

AD-A187 199

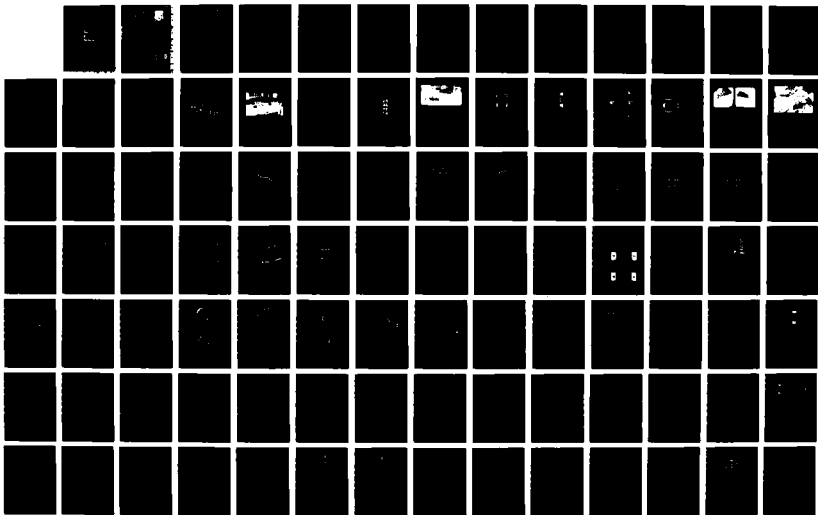
DISK PUMPING TEST(U) PRATT AND WHITNEY WEST PALM BEACH  
FL GOVERNMENT PRODUCTS DIV D J GRABER ET AL SEP 87  
PW/GPD-FR-19184 AFMAL-TR-87-2050 F33615-83-C-2331

1/2

UNCLASSIFIED

F/G 21/5

NL





2

AFWAL-TR-87-2050

DTIC FILE COPY

# DISK PUMPING TEST



D. J. Graber  
W. A. Daniels  
B. V. Johnson

United Technologies Corporation  
Pratt & Whitney  
Government Products Division  
P.O. Box 109600  
West Palm Beach, FL 33410-9600

September 1987

Final Report for Period August 1983 to February 1987

Approved for Public Release; Distribution Unlimited.

Aero Propulsion Laboratory  
Air Force Wright Aeronautical Laboratories  
Air Force Systems Command  
Wright-Patterson Air Force Base, Ohio 45433-6563

DTIC  
ELECTE  
DEC 09 1987  
S E D

87 11 01 100

AD-A187 199

UNCLASSIFIED

SECURITY CLASSIFICATION OF THIS PAGE

A187199

## REPORT DOCUMENTATION PAGE

1a. REPORT SECURITY CLASSIFICATION Unclassified		1b. RESTRICTIVE MARKINGS N/A										
2a. SECURITY CLASSIFICATION AUTHORITY N/A		3. DISTRIBUTION/AVAILABILITY OF REPORT Approved for Public Release; Distribution Unlimited										
2b. DECLASSIFICATION/DOWNGRADING SCHEDULE N/A												
4. PERFORMING ORGANIZATION REPORT NUMBER(S) P&W/GPD/FR-19184		5. MONITORING ORGANIZATION REPORT NUMBER(S) AFWAL-TR-87-2050										
6a. NAME OF PERFORMING ORGANIZATION Pratt & Whitney	6b. OFFICE SYMBOL (If applicable)	7a. NAME OF MONITORING ORGANIZATION Aero Propulsion Laboratory (AFWAL/POTX) AF Wright Aeronautical Laboratories										
6c. ADDRESS (City, State and ZIP Code) P.O. Box 109600 West Palm Beach, FL 33410-9600		7b. ADDRESS (City, State and ZIP Code) Wright Patterson Air Force Base Ohio, 45433-6563										
8a. NAME OF FUNDING/SPONSORING ORGANIZATION Disk Pumping Test	8b. OFFICE SYMBOL (If applicable) AFWAL/POTX	9. PROCUREMENT INSTRUMENT IDENTIFICATION NUMBER Contract F33615-83-C-2331										
8c. ADDRESS (City, State and ZIP Code) Wright Patterson Air Force Base Ohio, 45433-6563		10. SOURCE OF FUNDING NOS. <table border="1"><thead><tr><th>PROGRAM ELEMENT NO.</th><th>PROJECT NO.</th><th>TASK NO.</th><th>WORK UNIT NO.</th></tr></thead><tbody><tr><td>62203F</td><td>3066</td><td>10</td><td>25</td></tr></tbody></table>		PROGRAM ELEMENT NO.	PROJECT NO.	TASK NO.	WORK UNIT NO.	62203F	3066	10	25	
PROGRAM ELEMENT NO.	PROJECT NO.	TASK NO.	WORK UNIT NO.									
62203F	3066	10	25									
11. TITLE (Include Security Classification) Disk Pumping Test												
12. PERSONAL AUTHOR(S) D. J. Graber, W. A. Daniels, B. V. Johnson												
13a. TYPE OF REPORT Final	13b. TIME COVERED FROM Aug 1983 TO Feb 1987	14. DATE OF REPORT (Yr., Mo., Day) September 1987	15. PAGE COUNT 102									
16. SUPPLEMENTARY NOTATION												
17. COSATI CODES <table border="1"><thead><tr><th>FIELD</th><th>GROUP</th><th>SUB. GR.</th></tr></thead><tbody><tr><td>21</td><td>01</td><td></td></tr><tr><td>21</td><td>05</td><td></td></tr></tbody></table>		FIELD	GROUP	SUB. GR.	21	01		21	05		18. SUBJECT TERMS (Continue on reverse if necessary and identify by block number)	
FIELD	GROUP	SUB. GR.										
21	01											
21	05											
19. ABSTRACT (Continue on reverse if necessary and identify by block number) <p>An experimental study of secondary flows in gas turbine engines was conducted with cold flow models to develop an understanding of the disk pumping flow characteristics within a variety of disk/cavity configurations. Turbine disk torque experiments were conducted with co-rotating, counter-rotating, and one rotating/one static coaxial disk combinations. The experiments were conducted with selected combinations of disk shape, diaphragm between the rotating disks, bolts, and partial bolt covers. Turbine rim seal ingestion experiments were conducted with four seal configurations using a CO<sub>2</sub><sup>17</sup> trace gas measurement technique. Results showed the effects of gap spacing and seal configuration on the rim seal ingestion rate. Compressor drum aerodynamic experiments were conducted with a six cavity model and with coolant flow injected from three radial locations. Results showed the effects of coolant flowrate and coolant injection location on the pressure distribution in each cavity. Compressor drum heat-transfer experiments were conducted for heating and cooling transient flow conditions. The results were compared on a dimensionless basis with results from previous steady-state rotating heat-transfer experiments and from a free convection correlation for stationary plates.</p>												
20. DISTRIBUTION/AVAILABILITY OF ABSTRACT UNCLASSIFIED/UNLIMITED <input checked="" type="checkbox"/> SAME AS RPT. <input type="checkbox"/> DTIC USERS <input type="checkbox"/>		21. ABSTRACT SECURITY CLASSIFICATION Unclassified										
22a. NAME OF RESPONSIBLE INDIVIDUAL R. J. Martin		22b. TELEPHONE NUMBER (Include Area Code) (513) 255-8210	22c. OFFICE SYMBOL AFWAL/POTX									

## SUMMARY

An experimental study of secondary flows in gas turbine engines was conducted with cold flow models to develop an understanding of the disk pumping flow characteristics within a variety of disk/cavity configurations.

Turbine disk torque experiments were conducted with co-rotating, counter-rotating, and one rotating/one static coaxial disk combinations. The experiments were conducted with selected combinations of disk shape, diaphragm between the rotating disks, bolts, and partial bolt covers. Measured torque coefficients were compared with previous correlations for the one rotating/one static disk flow conditions. Measured torque coefficients showed the effects of coolant flow direction (inward or outward) and flowrate and the beneficial effect of a diaphragm with counter-rotating disks. One major result from this experiment is that the torque coefficients for counter-rotating disks with a diaphragm installed between disks is approximately the same as for the one static disk condition. The torque coefficients for the counter-rotating smooth turbine disk with no bleed flow and a diaphragm are approximately half those obtained without a diaphragm.

Turbine rim seal ingestion experiments were conducted with four seal configurations using a CO<sub>2</sub> trace gas measurement technique. Results showed the effects of gap spacing and seal configuration on the rim seal ingestion rate. The results were compared with previous results from the University of Sussex. An important conclusion of this experiment is that a decrease in the radial gap between rotating and static seals produced the largest improvement in cooling effectiveness for a given purge flowrate.

Compressor drum aerodynamic experiments were conducted with a six cavity model and with coolant flow injected from three radial locations. Results showed the effects of coolant flowrate and coolant injection location on the pressure distribution in each cavity. Tangential velocity distributions were deduced from the measured radial pressure distributions. The pressure distributions were compared with results from an analysis of the core flow and the boundary layer flow on the disks. The results of the comparison showed that the dimensionless secondary flow parameter,  $\eta_c = m(\pi\mu R_c)/(\rho v_c R_c/\mu)^{0.8}$  was effective in correlating the aerodynamic characteristics of the flow in the compressor cavities.

Compressor drum heat-transfer experiments were conducted for heating and cooling transient flow conditions. The results were compared on a dimensionless basis with results from previous steady-state rotating heat-transfer experiments and from convection correlation for stationary plates. An important conclusion from the experiment is that the maximum dimensionless heat transfer rates obtained during the transient cooling cycle were approximately twice as great as those for the heat cycle.



<b>Accession For</b>	
NTIS GRA&I	<input checked="" type="checkbox"/>
DTIC TAB	<input type="checkbox"/>
Unannounced	<input type="checkbox"/>
Justification	
<b>By</b>	
<b>Distribution/</b>	
<b>Availability Codes</b>	
<b>Dist</b>	<b>Avail and/or Special</b>
<b>A-1</b>	

## **FOREWORD**

This final technical report presents the work performed by Pratt & Whitney/Engineering Division under U.S. Air Force Contract F33615-83-C-2331. This report covers work accomplished from August 1983 through February 1987.

The principal investigators were Mr. Daryl J. Graber and Dr. Edwin J. Kawecki. The experiments were conducted by Mr. W. A. Daniels under the direction of Dr. Bruce Johnson. The Government Project Engineer was Mr. Richard J. Martin of the Aero Propulsion Laboratory, Air Force Wright Aeronautical Laboratories, WPAFB, Ohio.

## TABLE OF CONTENTS

<i>Section</i>	<i>Page</i>
I INTRODUCTION .....	1
II DESCRIPTION OF FACILITY AND APPARATUS .....	2
1. Internal Air Systems Facility .....	2
a. Mechanical Components .....	2
b. Instrumentation .....	3
2. Turbine Disk Assembly .....	4
a. Mechanical .....	5
b. Instrumentation .....	7
3. Turbine Rim Seal Assembly .....	7
a. Mechanical .....	8
b. Instrumentation .....	8
4. Compressor Drum Assembly .....	10
a. Mechanical .....	10
b. Instrumentation .....	11
III TURBINE DISK TORQUE EXPERIMENTS .....	13
1. Introduction .....	13
a. Problem .....	13
b. Objective .....	13
c. Approach .....	13
2. Discussion of Experiments and Results .....	13
a. Definition of Test Matrix and Dimensionless Parameters ...	13
b. Measurement Procedures .....	16
c. Results of Torque Measurements .....	16
d. Results of Radial Pressure Measurements .....	25
3. Correlation of Results .....	32
IV TURBINE RIM SEAL INGESTION EXPERIMENTS .....	36
1. Introduction .....	36
a. Problem .....	36
b. Objective .....	36
c. Approach .....	36
2. Discussion of Experiment and Results .....	37
a. Apparatus .....	37
b. Measurement Technique .....	38
c. Expected Results .....	38
d. Results for Concept Geometry .....	38
e. Results for Three Rim Seal Geometries .....	38
f. Comparison of Rim Seal Performance .....	43
3. Correlation of Results .....	45
a. Comparison with Turbulent Transport Model .....	45
b. Comparison With the University of Sussex Correlations ...	46

## TABLE OF CONTENTS (Continued)

Section		Page
V	COMPRESSOR DRUM AERODYNAMIC EXPERIMENTS .....	50
	1. Introduction .....	50
	a. Problem .....	50
	b. Objective .....	50
	c. Approach .....	51
	2. Discussion of Experiments and Results .....	51
	a. Test Procedure .....	51
	b. Results for Bleed Configuration A .....	55
	c. Results for Bleed Configuration B .....	56
	d. Results for Bleed Configuration C .....	57
	e. Comparison of Results for Bleeds A, B, and C .....	57
	3. Analysis of the Flow in the Bleed Cavity .....	60
	a. Parametric Results .....	60
	b. Analytical Formulation .....	62
	c. Comparison of Analysis with Experiment .....	64
	d. B Bleed Tangential Velocity Profiles .....	64
VI	COMPRESSOR DRUM HEAT TRANSFER EXPERIMENTS .....	67
	1. Introduction .....	67
	a. Problem .....	67
	b. Objective .....	67
	c. Approach .....	67
	2. Discussion of Experiments and Results .....	67
	a. Test Apparatus and Procedure .....	67
	b. Aerodynamic Results .....	68
	c. Heat-Transfer Results .....	69
	3. Comparison of Results with Previous Correlations .....	74
VII	CONCLUSIONS .....	76
	1. Turbine Disk Experiments .....	76
	2. Turbine Rim Seal Ingestion Experiments .....	76
	3. Compressor Drum Aerodynamic Experiments .....	77
	4. Compressor Drum Heat-Transfer Experiments .....	77
	APPENDIX — A Turbulent Diffusion Model For Turbine Rim Cavity. Seals .....	78
	1. Introduction .....	78
	2. Heat Ingestion Model .....	78
	3. Analytical Results .....	80
	4. Turbulent Transport Characteristics .....	83
	5. Concluding Remarks .....	85
	REFERENCES .....	86



## LIST OF ILLUSTRATIONS

<i>Figure</i>		<i>Page</i>
1	Internal Air Systems Facility .....	2
2	Internal Air Systems Facility With Pressure Chamber Cover Removed and Partially Assembled Compressor Model Installed .....	3
3	Turbine Disk Assembly Schematic .....	5
4	Turbine Disk Assembly Installed in Facility .....	6
5	Turbine Disk Models .....	6
6	Turbine Disk Model and Windage Diaphragm Mounted in Assembly ...	7
7	Turbine Rim Seal Assembly .....	8
8	Turbine Rim Seal Configurations .....	9
9	Instrumentation Sketch for Turbine Rim Seal Effectiveness Measurements .....	9
10	Compressor Drum Model Cross Section .....	10
11	Uninstrumented Compressor Drum Model Assembly .....	11
12	Compressor Drum Model Showing the Injection Manifold Plumbing, Outer Diameter Injectors Installed, and Portions of the Instrumentation Lead Paths .....	12
13	Exploded View of Heat Flow Sensor and RdF Corporation Microfoil ...	12
14	Test Matrix Identification for the Turbine Disk Torque Experiments ..	15
15	Torque Meter Calibration Curve .....	17
16	Torque Meter Zero-Torque Offset Curve .....	18
17	Comparison of Torque Coefficients for Flat Disks with Outflow ( $+\eta_t$ ) and Inflow ( $-\eta_t$ ); $Re_t = 1.6 \times 10^7$ , $S/R_o = 0.328$ .....	19
18	Comparison of Torque Coefficients for Flat Disks and Turbine Disks; $Re_t = 1.6 \times 10^7$ , $S/R_o = 0.328$ .....	20
19	Comparison of Torque Coefficients on Rotating and Static Turbine Disks; $Re_t = 1.6 \times 10^7$ , $S/R_o = 0.328$ .....	21
20	Effects of Windage Diaphragm on Torque Coefficients for Turbine Disks; $Re_t = 1.6 \times 10^7$ , $S/R_o = 0.328$ .....	22

# LIST OF ILLUSTRATIONS (Continued)

Figure		Page
21	Comparison of Torque Coefficient for Turbine Disks and Turbine Disks With Bolts; $Re_t = 1.6 \times 10^7$ , $S/R_o = 0.328$ .....	23
22	Comparison of Torque Coefficients for Turbine Disks With Bolts and Turbine Disks With Bolts and Covers; $Re_t = 1.6 \times 10^7$ , $S/R_o = 0.328$ .	24
23	Comparison of Torque Coefficient for Turbine Disks With Bolts and Bolt Covers at Two Disk Spacings; $Re_t = 1.6 \times 10^7$ .....	25
24	Tangential Velocity Profiles and Radial Pressure Drop for Various Values of the Core Rotation Factor $k$ .....	27
25	Radial Pressure Drop for Flat Disks With Flow Inward and Flow Outward; $Re_t = 1.6 \times 10^7$ , $S/R_o = 0.328$ , $ \eta_t  = 0.0026$ .....	28
26	Comparison of Radial Pressure Distribution Between Flat Disks and Turbine Disks With One Disk Static; Flow Inward, $Re_t = 1.6 \times 10^7$ , $S/R_o = 0.328$ .....	29
27	Tangential Velocity Profiles and Radial Pressure Drop for Co-rotating Turbine Disks; Flow Is Inward, $Re_t = 1.6 \times 10^7$ .....	30
28	Tangential Velocity Profiles and Radial Pressure Drop for Turbine Disks With One Disk Static; Flow Is Inward, $Re_t = 1.6 \times 10^7$ .....	31
29	Tangential Velocity Profiles and Radial Pressure Drop for Counter-Rotating Turbine Disks; Flow Is Inward, $Re_t = 1.6 \times 10^7$ .....	32
30	Comparison of Present Data With Classical Disk Theory, Schultz-Grunow Data (Reference 2) and Zimmermann, et al. Data (Reference 3); Flat Disks, $\eta_t = 0$ .....	33
31	Effects of Scaling Parameter for Counter-Rotating Flat Disks; Flow Inward .....	35
32	Rim Seal Geometries and Dimensions .....	37
33	Definitions of Seal Cooling Effectiveness Parameter, Dimensionless Flow Parameter, and Cavity Flow and Geometric Parameters .....	39
34	Typical Seal Cooling Effectiveness Parameter as a Function of Purge Flowrate .....	40
35	Rim Seal Cooling Effectiveness Parameter for Seal Configuration 1 ....	40
36	Rim Seal Cooling Effectiveness Parameter for Seal Configuration 2 ....	42
37	Rim Seal Cooling Effectiveness Parameter for Seal Configuration 3 ....	42

# LIST OF ILLUSTRATIONS (Continued)

<i>Figure</i>		<i>Page</i>
38	Rim Seal Cooling Effectiveness Parameter for Seal Configuration 4 ....	43
39	Dimensionless Tangential Velocity Profiles Obtained from the Measured Radial Pressure Distribution for Seal Configuration 3 .....	44
40	Effect of Radial Gap Width on the Cooling Effectiveness Parameter ...	44
41	Effects of Axial Spacing on the Cooling Effectiveness Parameter .....	45
42	Comparison of Present Data With Results of Turbulent Diffusion Model for Seal Configuration 3 .....	46
43	Definition of the Dimensionless Seal Gap Parameter, $S/R_s$ , Used in References 7 and 8 .....	47
44	Definition of the Dimensionless Seal Gap Parameter, $S/R_s$ , Used in References 7 and 8 .....	47
45	Comparison of Purge Velocity Ratio Results With Reference 8 .....	49
46	Typical Effect of Bleed Configuration on Tangential Velocity Distribution in Compressor Drum .....	51
47	Compressor Drum Model With Cavity Nomenclature .....	52
48	Operating Range for Compressor Drum Model .....	53
49	Pressure and Tangential Velocity Distributions in Selected Cavities of Compressor Drum With Baseline Flow Conditions and Coolant Injection Location A, Test Point A10 .....	55
50	Effects of Coolant Flowrate on Pressure and Tangential Velocity Distributions in Bleed Cavity for Coolant Injection Location A .....	56
51	Pressure and Tangential Velocity Distributions in Selected Cavities of Compressor Drum With Baseline Flow Conditions and Coolant Injection Location B, Test Point B5 .....	57
52	Effects of Coolant Flowrate on Pressure and Tangential Velocity Distributions in Bleed Cavity for Coolant Injection Location B .....	58
53	Pressure and Tangential Velocity Distributions in Selected Cavities of Compressor Drum With Baseline Flow Conditions and Coolant Injection Location C, Test Point C4 .....	59
54	Comparison of Pressure and Tangential Velocity Distributions in Compressor Cavity 2 for Baseline Flow Condition and Three Coolant Injection Locations .....	59

# LIST OF ILLUSTRATIONS (Continued)

Figure		Page
55	Comparison of Pressure and Tangential Velocity Distributions in Compressor Cavity A for Baseline Flow Condition and Three Coolant Injection Locations .....	60
56	Comparison of Pressure and Tangential Velocity Distributions in Compressor Cavity 2 for Baseline Secondary Flow Parameter and Two Tangential Reynolds Numbers .....	61
57	Prediction of Primary and Secondary Flow Characteristics for Cold Flow Experiments With Injection Location A .....	65
58	Comparison of Predicted and Measured Radial Pressure Distributions and Pressure Drop from Bleed to Bore Radii for Cold Flow Compressor Drum Experiments With Coolant Injection Location A .....	65
59	Effect of Flow Condition on Tangential Velocity Profile Shape Near Disk Bore in Bleed Cavity for Coolant Injection Location B .....	66
60	Effects of Heating and Cooling on the Bleed Cavity Aerodynamics .....	69
61	Variation of Air Temperature With Time at Compressor Drum Inlet, Disk 2 Bore, Disk 3 Bore, and Drum Outlet; $\eta_c = 0.04$ , Coolant Injection Location B .....	70
62	Variation of Air Temperature With Time at Three Radial Locations in Cavity 1 .....	71
63	Variation of Cavity Wall Temperature With Time at Selected Radial Locations in Cavity 1 .....	72
64	Variation of Surface Heat Flux With Time at Selected Radial Locations in Cavity 1 .....	73
65	Comparison of Dimensionless Heat-Transfer Result With Correlations from UTRC Freon Experiments and Flat Plate Theory .....	74
A-1	Turbine Rim Seal Components .....	79
A-2	Details of Turbulent Diffusion Model for Turbine Rim Cavity Seals ...	79
A-3	Axial Variation of Temperature in Annular Channel .....	81
A-4	Variation of Ingested Heat Flux Ratio With Coolant Flow Ratio .....	82
A-5	Variation of Cavity Effectiveness With Coolant Flow Ratio .....	83

## LIST OF TABLES

<i>Table</i>		<i>Page</i>
1	Turbine Disk Model Test Configurations .....	14
2	Turbine Rim Seal Test Matrix .....	41
3	Dimensional and Dimensionless Parameters for Turbine Rim Seal Ingestion Experiments .....	48
4	Test Conditions and Dimensionless Parameters for Compressor Drum Cold Flow Experiments With Coolant Injection Location A .....	53
5	Test Conditions and Dimensionless Parameters for Compressor Drum Flow Experiments With Coolant Injection Location B .....	54
6	Test Conditions and Dimensionless Parameters for Compressor Drum Flow Experiments With Coolant Injection Location C .....	54
7	Comparison of Core Rotation Factors, $k$ , for Selected Secondary Flow Parameters and Three Coolant Injection Locations .....	62
8	Test Conditions and Dimensionless Parameters for Compressor Drum Heat-Transfer Experiments .....	68

## LIST OF SYMBOLS

$C_1, C_2$	Constants
$C$	Rim Cavity $CO_2$ Concentration
$C_m$	Torque Coefficient
$C_o$	Gaspath $CO_2$ Concentration
$C_p$	Purge Flow $CO_2$ Concentration
$h$	Heat-Transfer Coefficient
$k$	Core Rotation Factor, $V/\Omega r$
$\dot{m}$	Coolant Mass Flowrate
$\dot{m}'_i$	Zero Purge Flow Ingestion Mass Flowrate
$\dot{m}_e$	Ejected Mass Flowrate
$\dot{m}_i$	Ingested Mass Flowrate
$\dot{m}_o$	Gas Path Mass Flowrate
$\dot{m}_p$	Purge Flow Mass Flowrate
$\dot{m}_s$	Secondary Mass Flowrate
$\dot{m}_t$	Coolant Mass Flowrate
$P$	Pressure
$q_o$	Dynamic Pressure
$Nu$	Nusselt Number
$Re_r$	Mass Flow Reynolds Number for Turbine and Turbine Rim Seal Experiment
$Re_t$	Tangential Reynolds Number
$Re_z$	Mass Flow Reynolds Number for Compressor Drum Experiments
$R_i$	Cavity Inlet Radius
$R_{in}$	Cavity Inside Radius
$R_o$	Disk Rim Radius
$R_s$	Rim Cavity Seal Radius

# LIST OF SYMBOLS (Continued)

$r$	Local Radius
$r/R_o$	Radius Ratio
$S$	Cavity Width
$S_{ca}$	Seal Axial Clearance
$S_{cr}$	Seal Radial Clearance
$S/R_o$	Seal Gap Parameter
$S/R$	Seal Gap Parameter
$S/R_s$	Seal Gap Parameter
$T_c$	Coolant Temperature
$T_w$	Wall Temperature
$U_r$	Boundary Layer Radial Velocity
$U_\theta$	Boundary Layer Tangential Velocity
$U_z$	Boundary Layer Normal Velocity
$V$	Core Tangential Velocity
$V_c$	Core Tangential Velocity
$V_j$	Jet Velocity
$V_p$	Seal Purge Flow Velocity
$V'_r$	Zero Purge Flow Ingestion Velocity
$V_{\phi j}$	Injected Flow Tangential Velocity
$V/V_o$	Core Flow Velocity Ratio
$V_p/V_o$	Purge Flow Velocity Ratio
$V'_r/V_o$	Zero Purge Flow Ingestion Velocity Ratio
$Z_o$	Cavity Axial Overlap
$\alpha$	Exponent

### LIST OF SYMBOLS (Continued)

$\beta$	Zero Purge Flow Ingested Mass Ratio
$\delta$	Boundary Layer Thickness
$\eta_c$	Mass Flow Parameter for Compressor Drum Experiments
$\eta_t$	Mass Flow Parameter for Turbine Disk and Turbine Rim Seal Experiments
$\eta'$	Zero Purge Flow Mass Flow Parameter
$\mu$	Molecular Viscosity
$\bar{\mu}$	Turbulent Viscosity
$\nu$	Kinematic Viscosity
$\rho$	Density
$\phi$	Cooling Effectiveness Parameter
$\Omega$	Disk Rotation Rate
$\omega$	Core Rotation Rate



## SECTION I

### INTRODUCTION

This Disk Pumping Test study addresses the objective of gaining a fundamental understanding of high speed rotating cavity flow fields through detailed experimental measurements. The trend of gas turbine engine performance and operating economics has driven advanced engine cycles to high rotor speeds, temperatures, and pressures, while at the same time demanding greater performance and life. In addition, competitive pressures are forcing a reduction in the development time of new and improved engines, putting a premium on an accurate first build understanding of system responses.

The internal air flow system of a gas turbine engine has the complex, interrelated responsibility of extracting and distributing cooling air from the main gaspath to provide a thermal environment that will maintain engine structural integrity and running clearance goals under steady-state and transient conditions, while it also pressurizes, cools, and thrust balances the rotor. With increasing rotor speeds and temperatures, the internal air flow system has evolved beyond a primary flow distribution and pressurization system to a complex thermal management system. As a result, internal air flow distribution management has become an essential part of engine design to meet the requirements of increasing component life at more severe operating conditions, and reducing cycle penalties inherent with the practice of bleeding secondary air from compressor stages for internal engine air flow management purposes.

The disks, drums, seals, and other internal components managed by the internal flow system are now required to operate adjacent to gaspath environments that are substantially beyond their design limits and to do so for long periods. To achieve high performance at these conditions and meet the increased life requirements, the structural members must be treated as complex heat exchangers. This requires a fundamental understanding of internal air flow dynamics, both to reduce uncertainties in the thermal management of structural members in new and conventional designs, and to accurately predict the system response of those improved components without resorting to expensive trial and error testing.

This study effort was directed at a fundamental understanding of representative flow fields in simple geometries at operating engine level conditions (i.e.,  $Re \approx 10^7$ ) to more complex geometries and flow fields reflecting actual engine components at these operation levels.

The study consisted of three major rig test series: (1) turbine disk cavity with co-rotating, counter-rotating, and one stationary wall, (2) turbine rim cavity, and (3) compressor drum cavity. These major tests have been accomplished and the nondimensional data is documented in this final report.

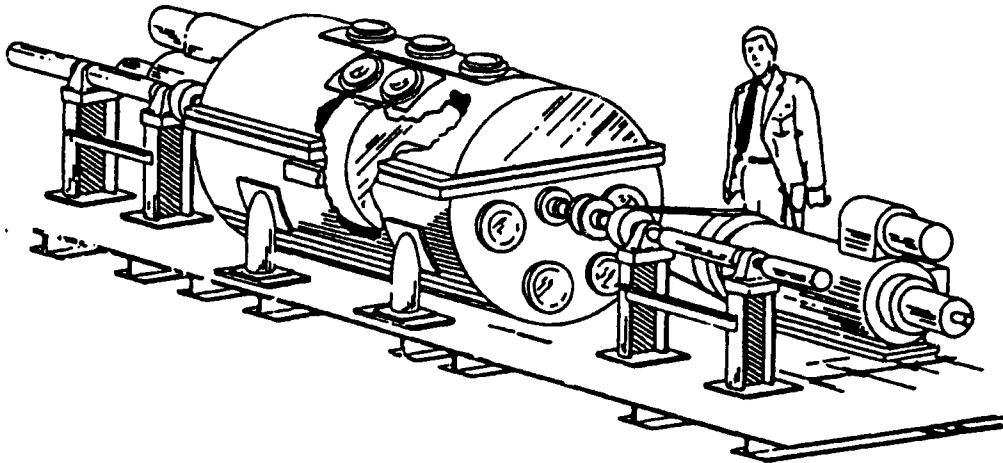
Technical effort was accomplished with the combined knowledge and capabilities of Pratt & Whitney (P&W)/Government Products Division, P&W/Commercial Engineering, and United Technologies Research Center (UTRC). Pratt & Whitney ensures that the test configurations represented engine internal air flow systems and that the test conditions were similar to actual engine environments. Rig tests were conducted at UTRC, East Hartford, Connecticut, using their unique test and instrumentation capability for simulating and documenting the internal flow fields of advanced technology engine features of high rotor speeds, counter-rotating, and engine hardware geometries specified by P&W.

## SECTION II

### DESCRIPTION OF FACILITY AND APPARATUS

#### 1. INTERNAL AIR SYSTEMS FACILITY

The United Technologies Research Center (UTRC) facility was designed for experimental investigation of aerodynamic and heat transfer characteristics of internal air flow system components, including compressor drums, turbine disks, turbine disk cavities, turbine rim cavity/seal systems, and rotating orifices. The facility has two independently operated drive systems which provide capability for co-rotating and counter-rotating disk experiments. Using air as the working fluid, the facility is capable of providing test conditions with dimensionless fluid parameters (e.g., Reynolds number) typical of current and advanced gas turbines. A sketch of the facility is shown in Figure 1, and instrumentation and mechanical capabilities are described in the following paragraphs.



FD 334551

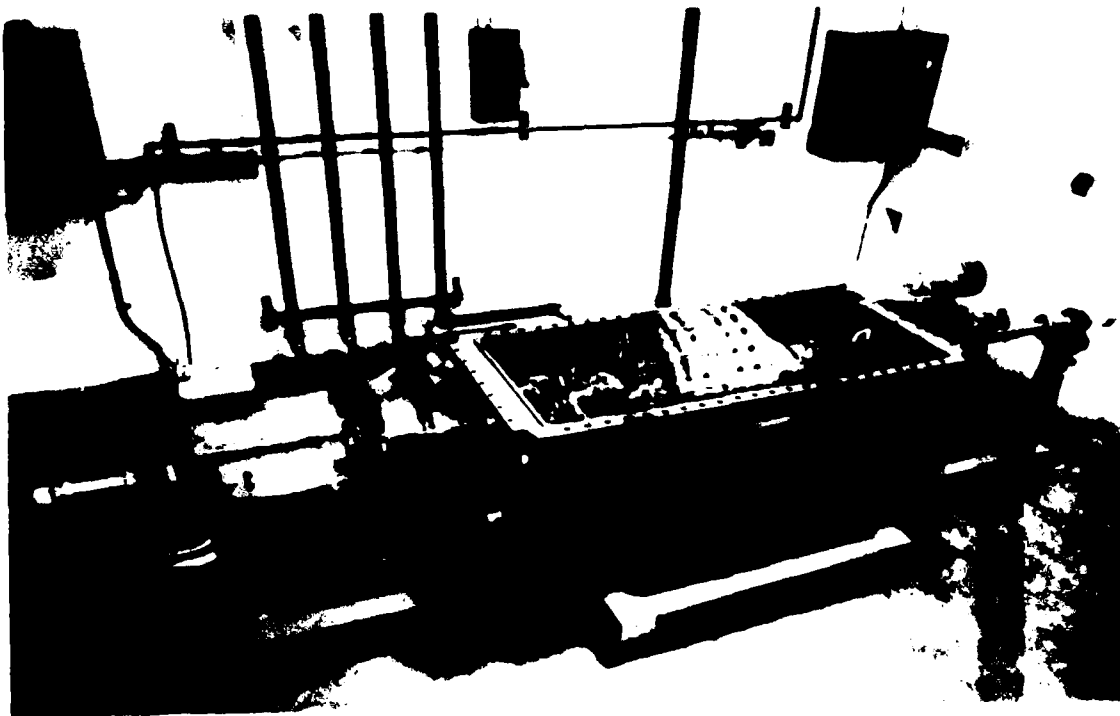
Figure 1. — Internal Air Systems Facility

##### a. Mechanical Components

The principal mechanical components of the facility include a pressure chamber, two drive systems, plumbing, flow control valves and meters, and two drive system control stations. The pressure chamber is designed to the American Society of Mechanical Engineers (ASME) boiler code specifications for pressure vessels and operates at pressures up to 150 psig. The vessel, approximately 3 feet in diameter and 6 feet in length, is designed so that the upper one-third of the vessel can be removed to facilitate model installation, modification, and checkout.

The pressure vessel and model air supply system receives compressed air at ambient temperature from the UTRC 400 psi compressor facility. The air is then regulated, and the flow to the vessel and model is measured by two of four turbine flowmeters. All of the flow going to the vessel and model is returned from the facility and is measured by the remaining two flowmeters before being exhausted into the atmosphere. The air supply system provides a flowrate of 1 pound/second to the test model. The test model air can be diverted through a heat exchanger which uses high-pressure steam to heat the air. This provides air temperatures at the model inlet of 180°F.

Each of the independently operated drive systems consists of a 30-horsepower, direct current motor, a belt-driven drive shaft with air-cooled, high speed bearing assemblies, drive pulleys, and a motor control station. The motors are driven in either direction and can rotate the drive shaft assembly and test model at speeds up to 3500 rpm. The drive systems, pressure chamber, and a partially assembled compressor drum model installed in the facility is presented in Figure 2.



UTRC No.

*Figure 2. — Internal Air Systems Facility With Pressure Chamber Cover Removed and Partially Assembled Compressor Model Installed*

#### **b. Instrumentation**

Facility instrumentation includes a data acquisition and control unit, flow and pressure measuring equipment, gas sampling equipment, vibration sensors, safety circuits, slipring assemblies, and computers.

##### **(1) Data Acquisition and Control Unit**

A Hewlett-Packard HP3497A and HP3498A data acquisition and control unit provides up to 300 analog channels for sampling output voltages from thermocouples, heat flux sensors, torque meters, strain gages, flowmeters, and pressure transducers. The unit is controlled manually (thereby simplifying checkout procedures) or by computer through an IEEE 488 interface. Sampling rates and channel selection can be varied and event timing can be recorded with the built-in clock.

## **(2) Flow and Pressure Measuring Equipment**

Four EFM turbine flowmeters are used to measure flowrates to the facility and test models. The flowmeter output signal is sensed by a Hewlett-Packard HP5384A frequency meter which is computer controlled through an IEEE 488 interface. Pressure measurements in flow lines, test models, and test chamber are obtained with three Scanivalve Model 48J4-1 scanning valve assemblies. Two of the 48-port scanning valve assemblies are used for making pressure measurements in test models in the rotating reference frame. All three scanning valve assemblies are controlled manually or by computer through the HP3497A data acquisition and control unit. Pressure transducers are available in ranges of  $\pm 1$  psid to  $\pm 250$  psid.

## **(3) Gas Sampling Equipment**

A Beckman Non-Dispersive Infrared Model 865 Analyzer is used for measuring carbon dioxide concentrations for ingestion and mass transfer investigations. Measurements are obtained from a multiple number of ports by using a single Scanivalve Model W56-12-SPL fluid switch to direct the gas sample from a specific location on the model to the gas analyzer. The system is operated manually or by computer.

## **(4) Vibration Sensors and Safety Circuits**

Rig and test model vibration levels are sensed by numerous Vibramite Model 302-9 vibration sensors. The sensors are mounted in horizontal and vertical pairs on drive shaft spindles, test model supports, bearing blocks, and other load bearing structures. Vibration sensor outputs are monitored by several Pratt & Whitney (P&W) Model 1517-1 vibration monitors. The monitors are connected to the facility drive system control station and automatically shuts off all systems when vibration levels exceed 2 mils at any sensor location.

## **(5) Slipping Assembly**

A Wendon Model W200-4-100 200 channel slipping assembly transmits transducer output and transducer excitation signals between the stationary and the rotating frames of reference.

## **(6) Computers**

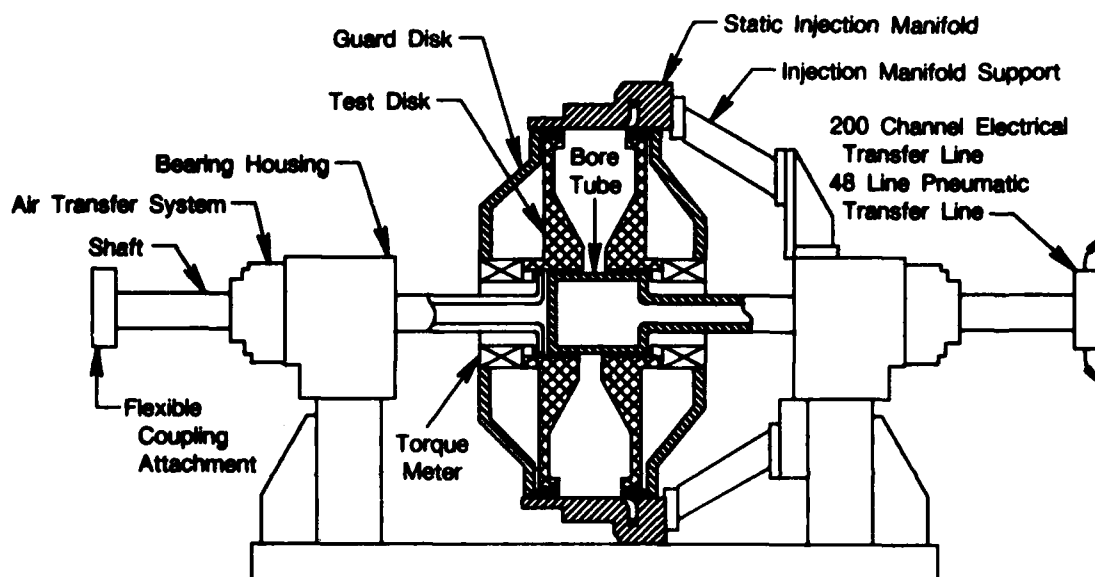
The facility uses two onsite computers. A DEC PDP 11/23 minicomputer with LSI 11 operating system and IEEE 488 interface is used to acquire data, control data acquisition sequences and to store data in raw form on floppy disk. The computer controls the facility's peripheral equipment including plotters, spectrum analyzer, frequency meter, data acquisition, and control unit and printer. Data reduction and analysis is performed on a Perkin-Elmer 3205 computer with a 50-million-byte fixed/removable disk drive assembly. Data is transferred from the DEC PDP 11/23 computer by RS232 line directly into the Perkin-Elmer 3205 computer. The Perkin-Elmer computer also supports peripheral equipment such as plotters, graphic terminals, printers, and magnetic tape drives.

## **2. TURBINE DISK ASSEMBLY**

A turbine disk assembly was designed and built to conduct the turbine disk and turbine disk cavity aerodynamic and torque measurement experiments. The assembly was designed to accommodate several disk models. The assembly consists of two opposing disk models which are rotated independently in either direction at speeds up to 3500 rpm. The assembly also has the capability to measure the torque on each disk. The prominent mechanical and instrumentation features of the turbine disk assembly are described in the following paragraphs.

### a. Mechanical

The principal mechanical components of the turbine disk assembly include drive shaft and bearing assemblies, air transfer and injection systems, model disks, guard disks, and model support. The turbine disk assembly and major components are depicted in Figure 3. Each side of the assembly has an independent drive unit consisting of a bearing housing which supports a drive shaft, guard disk, torque meter, and disk model. A stationary-to-rotating frame air transfer system is incorporated in each of the bearing housings to bleed air into the model or to withdraw air from the model. The model support permits separation of one unit from the other to facilitate changing test disk configurations, disk spacing, and the addition of hardware such as a windage diaphragm.

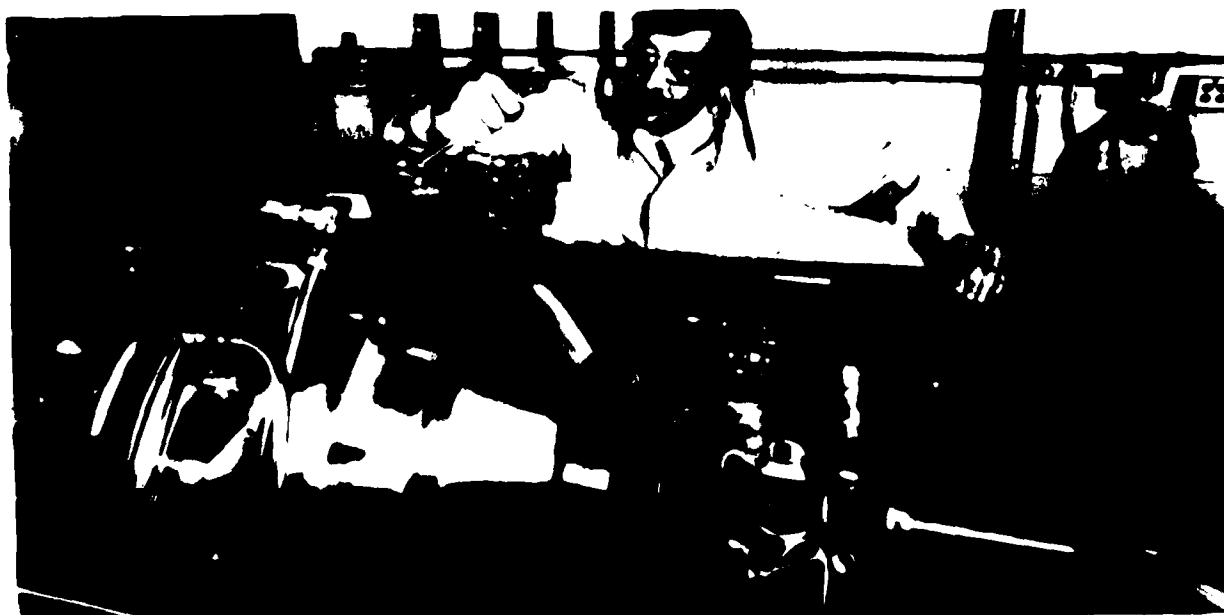


FDA 334552

Figure 3. — Turbine Disk Assembly Schematic

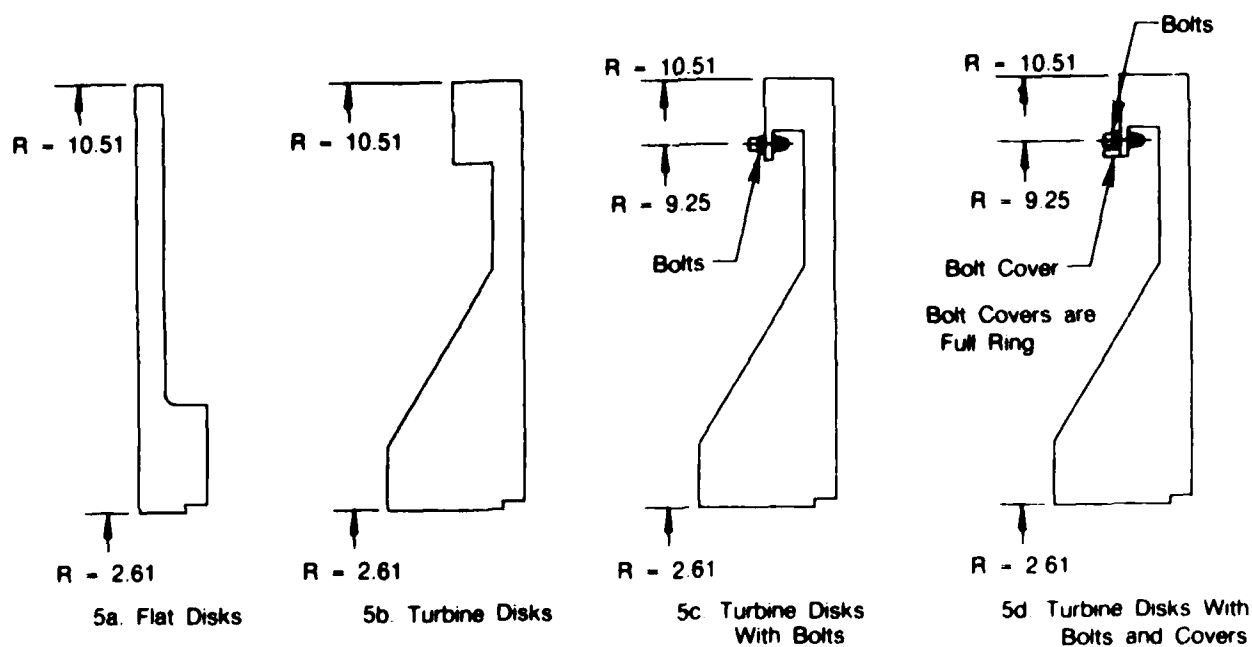
Coolant is introduced into the cavity between the disk models at one of two locations: the rotating bore tube or a static injection manifold. From the bore tube, the coolant is bled through 24 radial holes located circumferentially at three axial locations. The static injection manifold is located at the disk cavity outer diameter (OD). The static injection manifold contains 18 injection nozzles arranged in three sets of six equally spaced nozzles. The nozzles are tangentially oriented with the cavity OD and each set of nozzles is sized to produce a given coolant swirl level at a given coolant flowrate. Each set of injection nozzles is supplied by an individual supply manifold which is controlled and located outside the pressure chamber test section. Figure 4 shows the turbine disk assembly installed in the facility including a portion of the static OD injection manifold and manifold plumbing.

Several test disk models were used in the experiment, including flat disks, smooth disks having a typical turbine disk geometry, turbine disks with bolts, and turbine disks with bolts and bolt covers. Cross sections of these test disk configurations are shown in Figure 5. The disk rim radius for each configuration was 10.51 inches and the disk bore radius was 2.61 inches. The disk configurations with bolts employed 40 equally spaced 10-24 socket head cap screws at a radius of 9.25 inches.



UTRC No

Figure 4. — Turbine Disk Assembly Installed in Facility



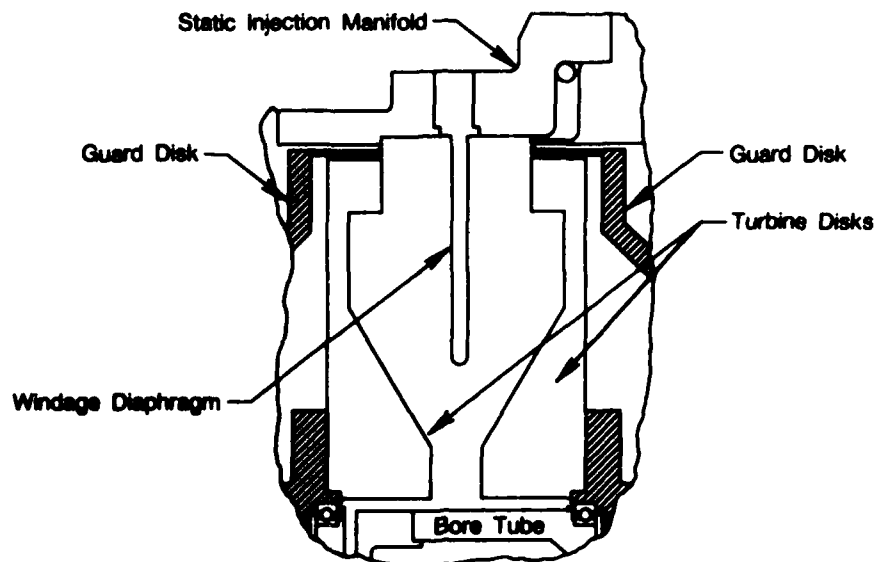
Dimensions in Inches

FDA 334553

Figure 5. — Turbine Disk Models

The axial spacing between disk models was altered by the addition of a spacer to the drive shaft of one of the disk drive units. With the spacer, the reference axial disk spacing of 3.45 inches was decreased to 2.45 inches.

The static OD wall of the disk cavity was designed to accept a windage diaphragm. When installed, the diaphragm was located at midcavity and extended from a radius of 5.65 inches to the cavity OD. Figure 6 presents the turbine disk configuration with windage diaphragm installed.



FDA 334564

Figure 6. — Turbine Disk Model and Windage Diaphragm Mounted in Assembly

#### b. Instrumentation

Test disk radial pressure measurements were made in the rotating reference frame using a Model 48J4-1 scanivalve assembly and a  $\pm 25$ -psid scanivalve pressure transducer. Each of the models contained 24 static pressure taps at different radial and azimuthal locations on the disk. All of the static pressure taps were installed flush with the disk surface.

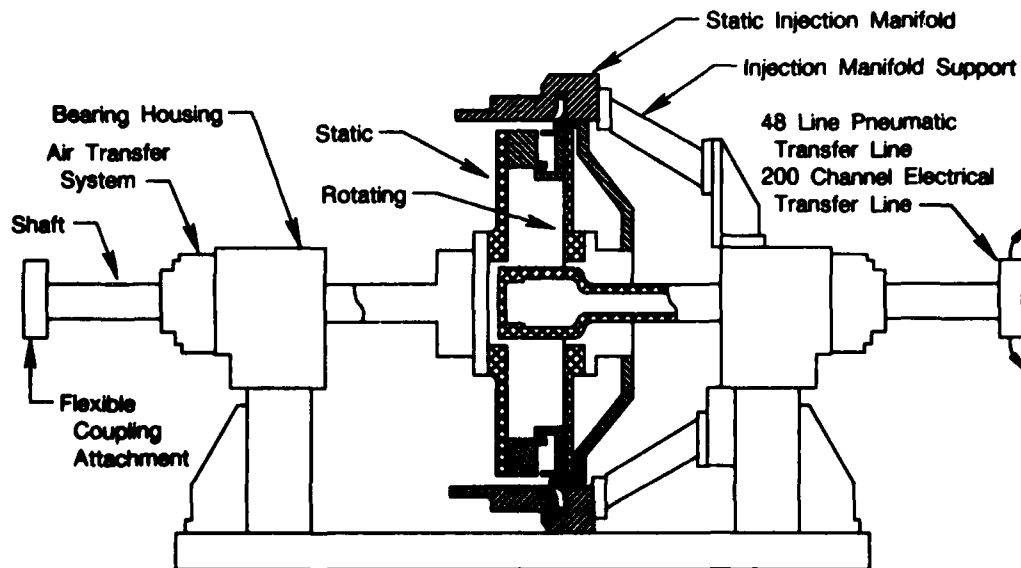
Air temperature measurements at the disk cavity OD were made using six ungrounded chromel-alumel thermocouples. The thermocouples were located at various azimuthal locations on the static OD wall of the cavity. The thermocouples were enclosed in a 0.065 inch stainless steel sheath and protruded radially into the cavity 0.5 inch.

The torque on each disk was measured in the rotating reference frame by two LeBow Model 2404-128 torque meters. The assembly was designed to measure only the torque on one side of the model disk. The torque meters were mounted between the guard disks and the test disks. This created a "buffer" cavity in back of the test disk with seals and a guard disk so that the air in this cavity rotates as a solid body with the same rotational speed as the test disk. Therefore, the air in this buffer cavity does not exert an aerodynamic torque on the back of the test disk.

#### 3. TURBINE RIM SEAL ASSEMBLY

A turbine rim seal assembly was designed and built to conduct the turbine rim seal ingestion experiments. The model cross section is shown in Figure 7. The principal components of the assembly include a rotating disk model, stationary disk model, injection manifold for injecting swirling air across the OD of the rim seal model to simulate the primary gaspath flow,

and bore bleed injection system for injecting purge flow into the rim seal cavity model. The assembly was designed to simulate a rim cavity and the aerodynamic seal on the downstream side of a rotor.



FDA 334555

Figure 7. — Turbine Rim Seal Assembly

#### a. Mechanical

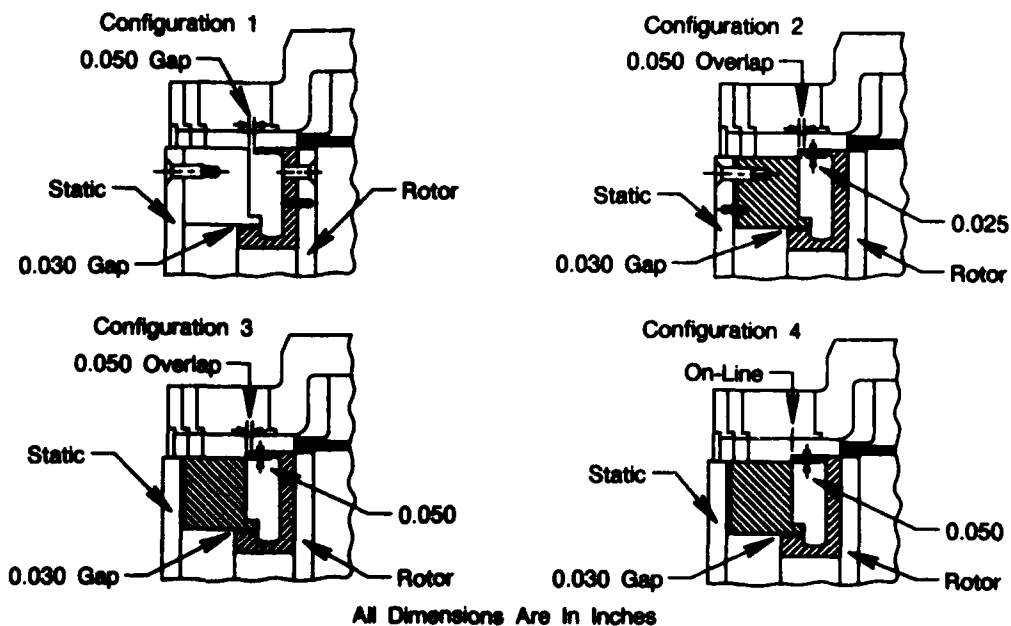
The assembly uses the drive units, model support, and air injection systems that were used in the turbine disk assembly. The rim cavity and rim seal model configurations were formed by attaching shaped rings to the flat disk models used in the turbine disk torque experiments. Four rim cavity and seal configurations were investigated, as shown in Figure 8. The rotor has a rim radius of 10.51 inches and was unaltered during the investigation. The rim seal geometries and cavity aspect ratios shown in Figure 8 were obtained by altering the stator section.

#### b. Instrumentation

A trace gas technique was used to determine the amount of gaspath flow ingested into the rim cavity model. The trace gas used in the investigation was carbon dioxide ( $\text{CO}_2$ ). The procedure was to mix  $\text{CO}_2$  with the cavity purge flow to a predetermined  $\text{CO}_2$  concentration level, and then to measure the  $\text{CO}_2$  concentration levels at various locations within the rim cavity model. The  $\text{CO}_2$  concentration levels measured are used to determine a cavity cooling effectiveness for each coolant flowrate.

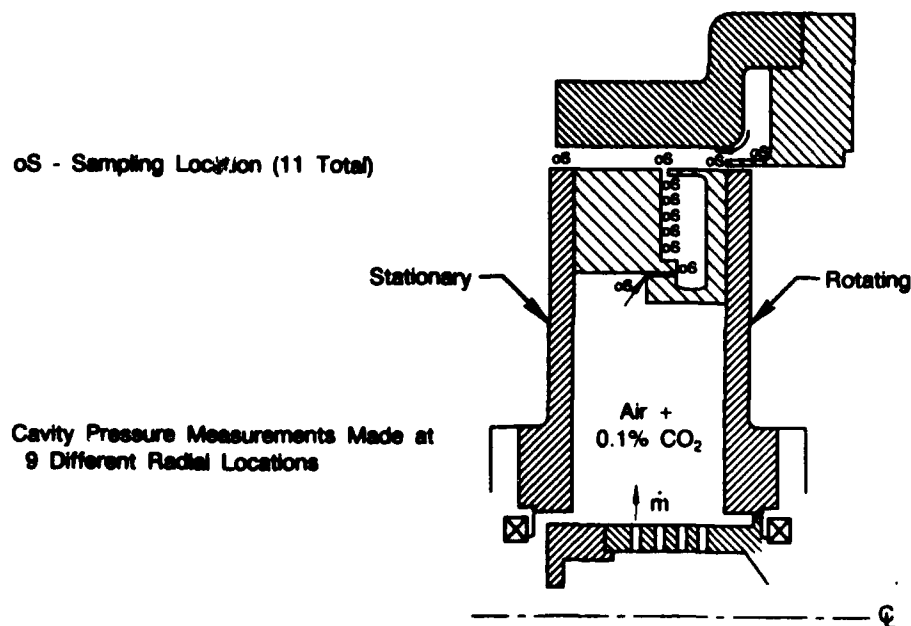
A Beckman Non-Dispersive Infrared Model 865 Analyzer measured  $\text{CO}_2$  concentration levels at 11 locations within the model. A schematic of the model showing the gas sampling locations and the cavity purge flow system is presented in Figure 9. All measurements were made in the stationary reference frame, and all  $\text{CO}_2$  sampling taps were installed flush with the cavity wall surface.





FDA 334556

Figure 8. — Turbine Rim Seal Configurations



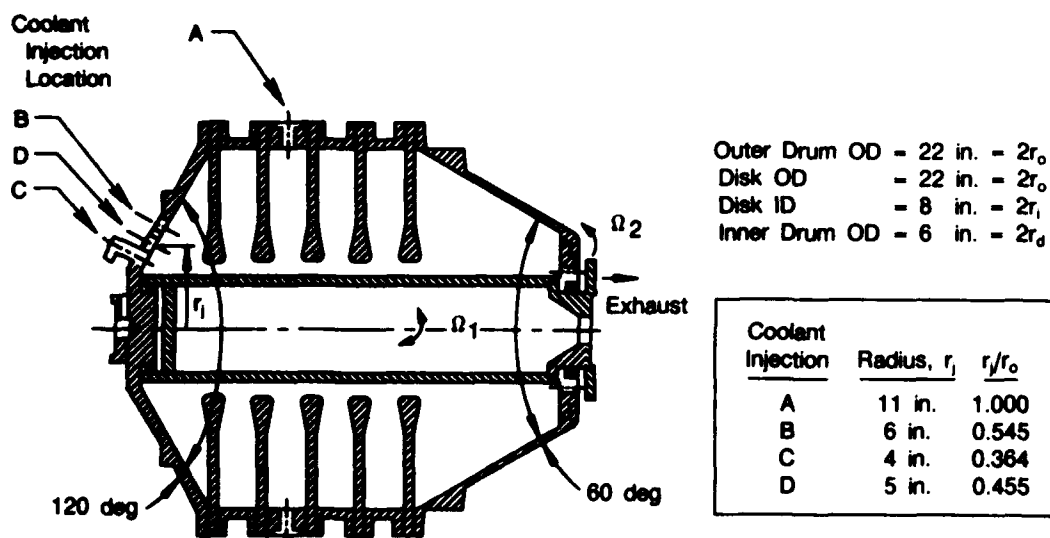
FDA 334557

Figure 9. — Instrumentation Sketch for Turbine Rim Seal Effectiveness Measurements

In addition to CO<sub>2</sub> concentration measurements, static pressure measurements were made at nine radial locations within the model. The measurements were made with a Model 48J4-1 scanivalve assembly using a  $\pm 15$ -psid scanivalve pressure transducer. All pressure taps were installed flush with the wall surface.

#### 4. COMPRESSOR DRUM ASSEMBLY

A compressor drum model was designed and built by UTRC to conduct the compressor drum aerodynamic and heat transfer experiments. The model contains six cavities with tapered endwalls and compressor disk geometries. An independently driven bore tube simulated co-rotating and counter-rotating bore tube designs. The maximum design speed of the model is 2000 rpm. The model has a maximum operating temperature of 300°F. The model cross section is shown in Figure 10.



FDA 334558

Figure 10. — Compressor Drum Model Cross Section

##### a. Mechanical

The compressor drum model has an overall length of 27.5 inches and a drum cavity and disk rim diameter of 22 inches. The disk bore diameter is 8 inches and the bore tube has a diameter of 6 inches. The upstream conical endwall is tapered to a 120 degree included angle while the downstream endwall taper is 60 degrees, as shown in Figure 10.

Coolant flow is injected into the model at several locations. Three injection locations are available on the 120 degree conical endwall for simulating coolant flow from a low-pressure compressor (LPC) into the high-pressure compressor (HPC) disk cavity. These are shown in Figure 10 as coolant injection locations B, C, and D. Each of the locations contain 8 equally spaced bleed ports at 6, 5, and 4 inch radii, respectively. Injection of coolant from the HPC gaspath is modeled by injecting air through passages located at the OD of the cavity between disks 2 and 3 and is shown as coolant injection location A in Figure 10. At location A, up to 24 injectors can be used. In this investigation, coolant injection locations A, B, and C were used. The uninstrumented compressor drum model is shown in Figure 11. The injectors at each coolant injection location are supplied air from a manifold attached to the 120-degree conical endwall. The manifold rotates with the model and is supplied by a stationary-to-rotating frame air transfer system that is incorporated in the bearing housing of the model. All coolant is exhausted from the model through 18 equally spaced holes located on the 60-degree conical endwall at a radius of 3.5 inches. The compressor drum model showing the coolant injection manifold and plumbing, OD injectors installed, and portions of the instrumentation lead paths is shown in Figure 12.



UTRC No

*Figure 11. — Uninstrumented Compressor Drum Model Assembly*

#### **b. Instrumentation**

The compressor drum model was instrumented with 43 thermocouples for measuring air temperature, 63 wall thermocouples for measuring metal temperatures, 63 heat flux sensors for measuring surface heat flux, and 68 pressure taps (including 16 on the bore tube) for measuring static pressure. The instrumentation was located at various radial and azimuthal locations throughout the model and provides the capability of measuring air temperatures at an average of 5 radii per cavity, wall temperatures at an average of 6 radii per cavity, wall heat flux at an average of 6 radii per cavity, and static pressure at an average of 7 radii per cavity.

The air thermocouples were chromel-alumel ungrounded thermocouples in a 0.040-inch sheath and mounted with the thermocouple junction protruding 0.5 inch from the model test surface. The heat flux and wall temperature sensors were made by the RdF Corporation as one unit consisting of a chromel-alumel thermocouple and a copper-constantan thermal difference amplifier. The sensor is shown in Figure 13. The heat flux sensors were mounted on the disk and wall surfaces of the model with the electrical leads buried in a recessed channel adjacent to the sensor. The channels were then filled with a casting resin and finished flush with the surface. With an average thickness of the heat flux sensors at about 5 mils, and with no exposed electrical leads, the compressor drum test surfaces were considered to be aerodynamically clean.



UTRC No.

*Figure 12. — Compressor Drum Model Showing the Injection Manifold Plumbing, Outer Diameter Injectors Installed, and Portions of the Instrumentation Lead Paths*

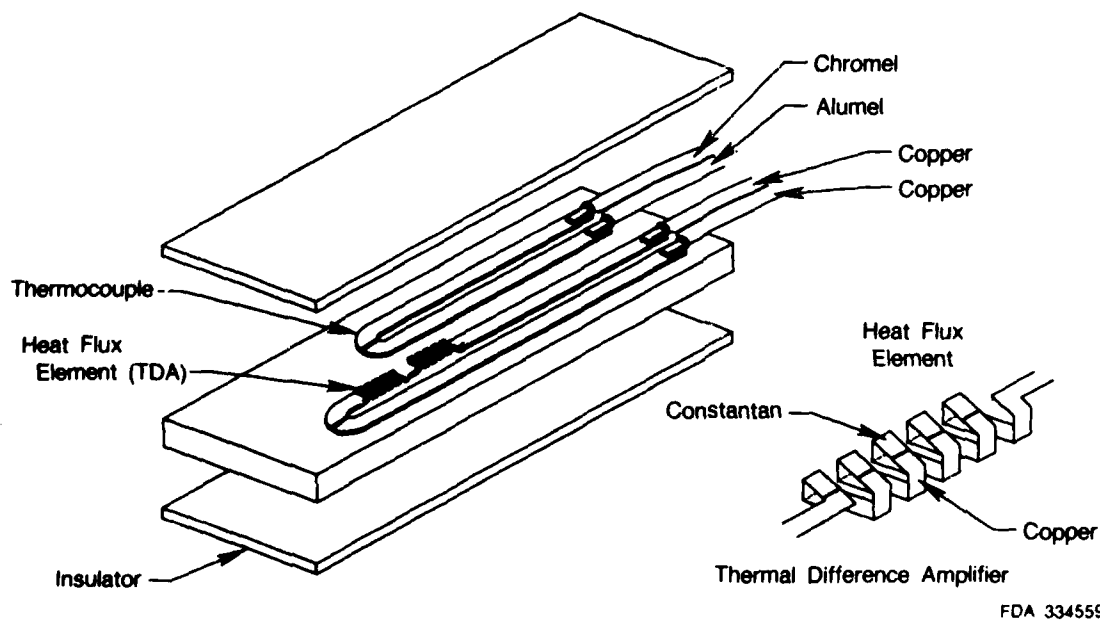


*Figure 13. — Exploded View of Heat Flow Sensor and RdF Corporation Microfoil*

## SECTION III

### TURBINE DISK TORQUE EXPERIMENTS

#### 1. INTRODUCTION

##### a. Problem

The flow fields in the turbine disk cavities are dominated by disk pumping generated by rotation of the disks. The amount of air that is supplied for cooling the turbine is generally less than the flowrate pumped in the boundary layers of the disks. As a result, recirculating flows are generated in the cavities adjacent to the disk. The work done on the fluid in the boundary layer (windage) can be significant and can result in a rise of the total temperature of the fluid. This increased temperature of the fluid being recirculated next to the disk reduces the capability of the fluid to remove heat from the disk. Wall friction and the flows in cavities adjacent to enclosed disks are influenced by several factors. The geometry of the disk cavity influences the recirculation patterns induced by the disk pumping secondary flows. The flow field in a cavity between a rotating disk and a stationary wall is significantly different than that in a cavity between co-rotating or counter-rotating disks. Protuberances on the disks in the form of bolts and other hardware contribute to friction losses and therefore heat generation. These influencing factors have led to the use of devices such as bolt covers and windage diaphragms that are designed to decrease wall friction and torque requirement losses. Other factors influencing windage loss and cavity recirculation regimes include coolant flowrate, disk geometry, coolant injection location, and disk speed.

##### b. Objective

The objectives for this phase of the investigation were to document and correlate disk friction and disk cavity aerodynamic characteristics for the classes of disk cavity flow fields and configurations found in the turbine region of gas turbine engines.

##### c. Approach

To achieve these objectives, an experimental investigation was conducted to obtain aerodynamic and disk friction data for several disk geometries, disk cavity configurations, and flow conditions. Disk radial pressure measurements and disk torque measurements were obtained for a rotating disk in a static shroud, co-rotating disks in a static shroud, and counter-rotating disks in a static shroud. The disk model geometries investigated ranged from simple flat disks to disks having typical turbine disk geometries. The effects of bolts, bolt covers, windage diaphragm, and disk spacing were determined. All measurements were obtained at Reynolds numbers typical of current and advanced gas turbine engines using air as the working fluid.

#### 2. DISCUSSION OF EXPERIMENTS AND RESULTS

##### a. Definition of Test Matrix and Dimensionless Parameters

The experiments were conducted using the turbine disk test facility described in Section II with six disk model configurations. Measurements were obtained for a total of 122 flow conditions. The disk model configurations were shown in Figure 5. The test plan for each model configuration consisted of a series of experiments for the test disk flow conditions of co-rotation, counter-rotation, and one disk static. Disk torque and radial pressure measurements were obtained for each disk geometry at the flow conditions identified in the Table 1 test matrix by tangential Reynolds number, coolant flowrate, and coolant injection location. Table 1 also lists the disk configurations and the coolant injection location.

TABLE 1.  
TURBINE DISK MODEL TEST CONFIGURATIONS

Configuration	Test Series	Data Points	Test Matrix	Conditions	Injection Location
1 — Flat Disks	1	10	B	Co-rotating	Flow Injected at OD
	2	12	A	Counter-rotating	
	3	10	B	One Static	
	4	4	C	Co-rotating	Flow Injected at ID
	5	4	C	Counter-rotating	
	6	4	C	One Static	
2 — Turbine Disks	7	4	C	Co-rotating	Flow Injected at OD
	8	4	C	Counter-rotating	
	9	4	C	One Static	
3 — Turbine Disks with Diaphragm	10	12	A	Counter-rotating	Flow Injected at OD
4 — Turbine Disks and Bolts	11	4	C	Co-rotating	Flow Injected at OD
	12	4	C	Counter-rotating	
	13	4	C	One Static	
5 — Turbine Disks, Bolts, and Covers	14	4	C	Co-rotating	Flow Injected at OD
	15	4	C	Counter-rotating	
	16	4	C	One Static	
	17	4	C	Co-rotating	Flow Injected at ID
	18	4	C	Counter-rotating	
	19	4	C	One Static	
6 — Disks, Bolts, Covers, and Spacing	20	4	C	Co-rotating	Flow Injected at OD
	21	10	B	Counter-rotating	
	22	4	C	One Static	

3918C

The number of flow conditions (data points) for each test matrix are shown in Figure 14. Each flow condition in Figure 14 is identified by a dimensionless mass flow Reynolds number  $Re_r$  and a tangential Reynolds number  $Re_t$ . The mass flow Reynolds number is defined:

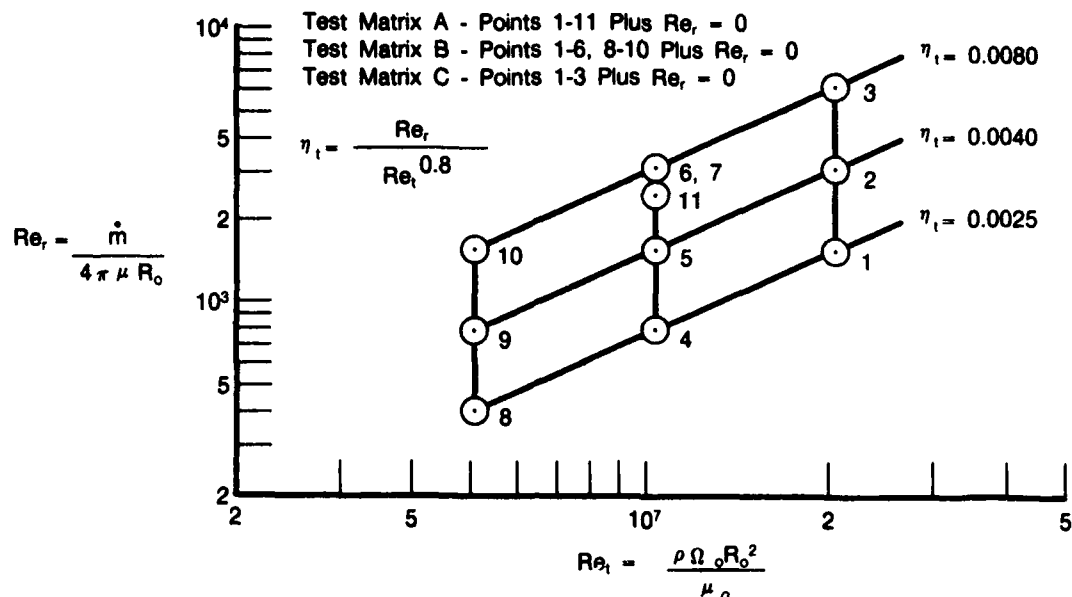
$$Re_r = \dot{m} / (4\pi R_o \mu) \quad (1)$$

where:

$\dot{m}$  = coolant mass flowrate

$R_o$  = disk rim radius

$\mu$  = dynamic viscosity of the fluid at the temperature of the fluid at the disk cavity outer diameter (OD).



FDA 334560

Figure 14. — Test Matrix Identification for the Turbine Disk Torque Experiments

The tangential Reynolds number is defined:

$$Re_t = \rho \Omega R_o^2 / \mu \quad (2)$$

where:

$\Omega$  = rotation rate of the disk

$\rho$  = fluid density at the disk cavity OD pressure and temperature.

These Reynolds numbers are combined to form a dimensionless flow parameter ( $\eta_t$ ) which has been shown (Reference 1) to correlate disk cavity pressure drop with flow conditions. This parameter is defined:

$$\eta_t = Re_t / Re_t^{0.8} \quad (3)$$

Where:

$\eta_t$  = secondary flowrate parameter that resulted from a turbulent disk friction analysis performed in Reference 1.

This scaling parameter will be used in the presentation of results. The range of tangential Reynolds numbers covered in the investigation (Figure 14) are typical of the operating range of a large gas turbine engine.

## **b. Measurement Procedures**

The principal measurements made for each disk model configuration were disk radial pressure measurements and disk torque measurements. Radial pressure measurements were made at 17 different radial and azimuthal locations on one disk. The measurements were made in the rotating reference frame with a 48-port Model 48J4-1 scanivalve assembly using a  $\pm 25$ -psid scanivalve pressure transducer. The pressure transducer was calibrated with a dead weight tester at repeated intervals throughout the investigation and was accurate and repeatable to within  $\pm 0.04$  psi.

The torque on each of the disk models was measured in the rotating frame of reference using two LeBow Model 2404-128 torque meters. Calibration of the torque meters consisted of a static and a dynamic calibration procedure. The static calibration procedure was performed to determine the torque versus transducer output (voltage) curve of the instrument. The torque meter was statically calibrated by hanging weights on a calibration arm supplied with the instrument and recording the transducer output voltage for the torques (in both directions) produced by the weights.

The dynamic calibration procedure was performed to determine the thermal offset experienced by the transducer as a result of temperature variations. A rise in temperature of the transducer causes a thermal offset in the zero-torque reading of the transducer compared with the static calibration zero-torque reading obtained at room temperature. The dynamic calibration procedure for each meter consisted of making flat disk torque measurements at different disk rotation rates in both directions with a high rate of air flow from the model bore toward the disk cavity OD. The amount of air bled into the model was based on the disk pumping requirements of a "free" disk given in Reference 2. Results from a typical dynamic calibration run are shown in Figure 15. The measured disk torque, based on the static calibration results, is plotted versus the disk rotation rate. Note the zero-torque offset of the raw data in Figure 15 and that the data corrected for this offset compares favorably with the predicted torque (Reference 2) of a free disk. Repeated dynamic calibration of each torque meter at different rig temperatures showed that the thermal zero-torque offset experienced by each transducer was approximately a linear function of transducer temperature. A torque meter zero-torque offset curve is shown in Figure 16.

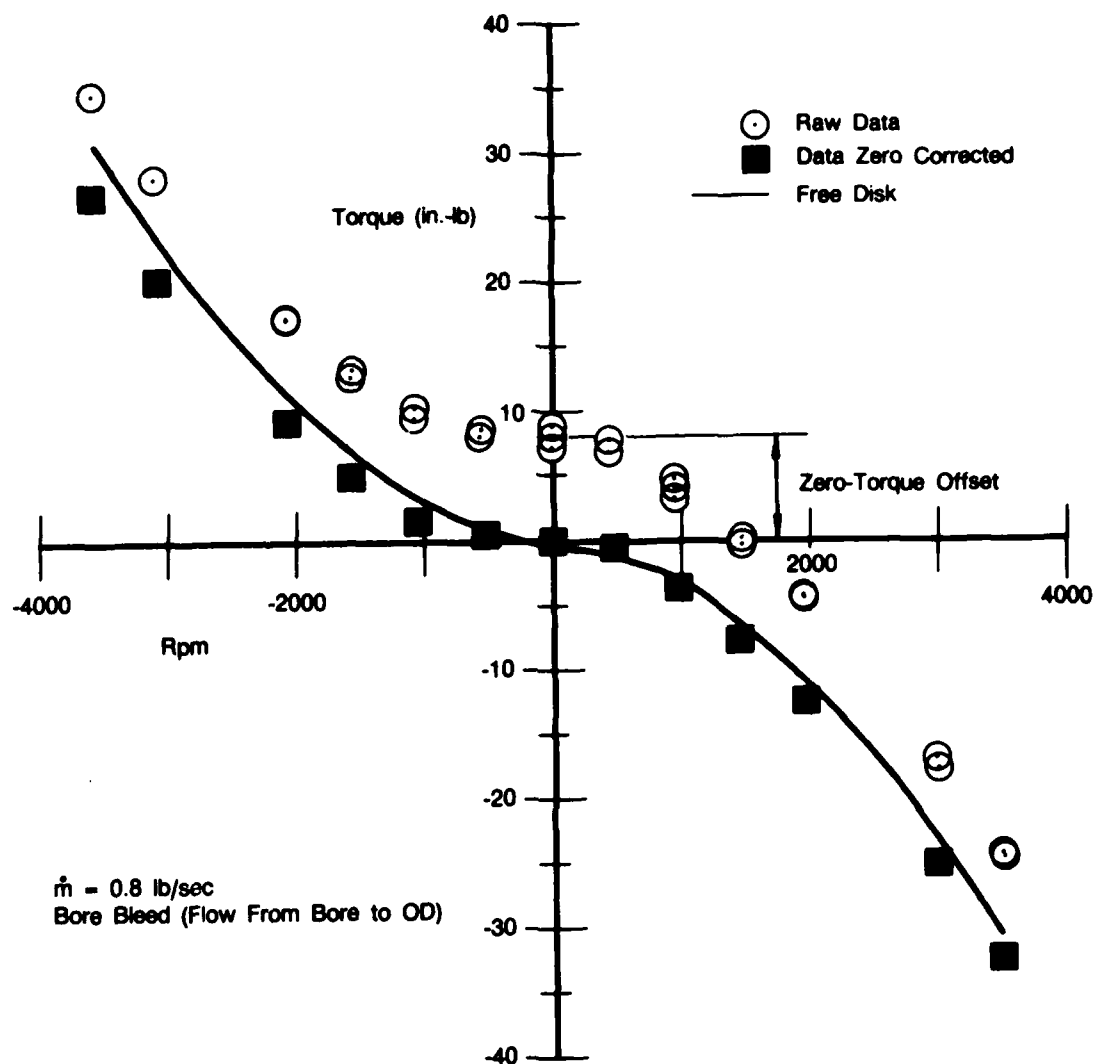
## **c. Results of Torque Measurements**

### **(1) Flat Disk Model Experiments**

Flat disk torque measurements were obtained for the disk model conditions of co-rotation, counter-rotation, and one static disk with various flowrates from two injection locations. The disk model cavity was bled with outward flow (positive  $\eta_t$ ) from the model bore tube and with inward flow (negative  $\eta_t$ ) from a static injection manifold located at the cavity OD (Figure 3). The fluid injected at the cavity OD was injected with swirl levels of approximately one-half the disk rotation rate and was withdrawn at the bore.

The measurements were obtained at tangential Reynolds numbers of  $4.0 \times 10^6$ ,  $8.0 \times 10^6$ , and  $1.6 \times 10^7$ . The disk speed was constant at 3500 rpm and the test chamber operating pressures were varied to obtain these tangential Reynolds. The disk spacing for the flat disk experiments was constant with a cavity width to disk radius ratio of  $S/R_0 = 0.328$ .





FDA 334561

Figure 15. — Torque Meter Calibration Curve

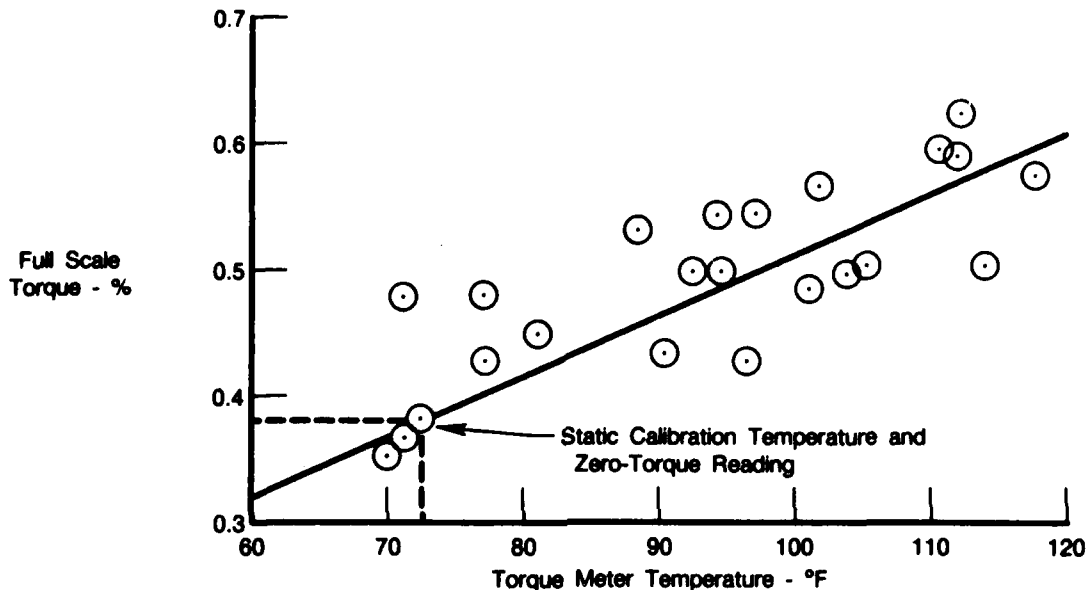
Flat disk torque coefficients for  $Re_t = 1.6 \times 10^7$  are shown in Figure 17. The torque coefficient ( $C_m$ ) is defined:

$$C_m = \text{Torque} / (0.5 \rho \Omega^2 R_o^4) \quad (4)$$

and is plotted versus the flow parameter  $\eta_t$  for both inward and outward flow. Following are observations from the data:

- $C_m$  is lowest for co-rotating disks and highest for counter-rotating disks for both inward flow and outward flow
- $C_m$  for counter-rotating disks is independent of flowrate and flow direction

- $C_m$  for co-rotating and one static disk flow conditions are dependent upon flowrate and flow direction
- $C_m$  for co-rotating and one static disk flow conditions are higher for outward flow than for inward flow
- $C_m$  for co-rotating and one static disk flow conditions increase with increasing flowrate for flow outward and decreases with increasing flowrate for flow inward.



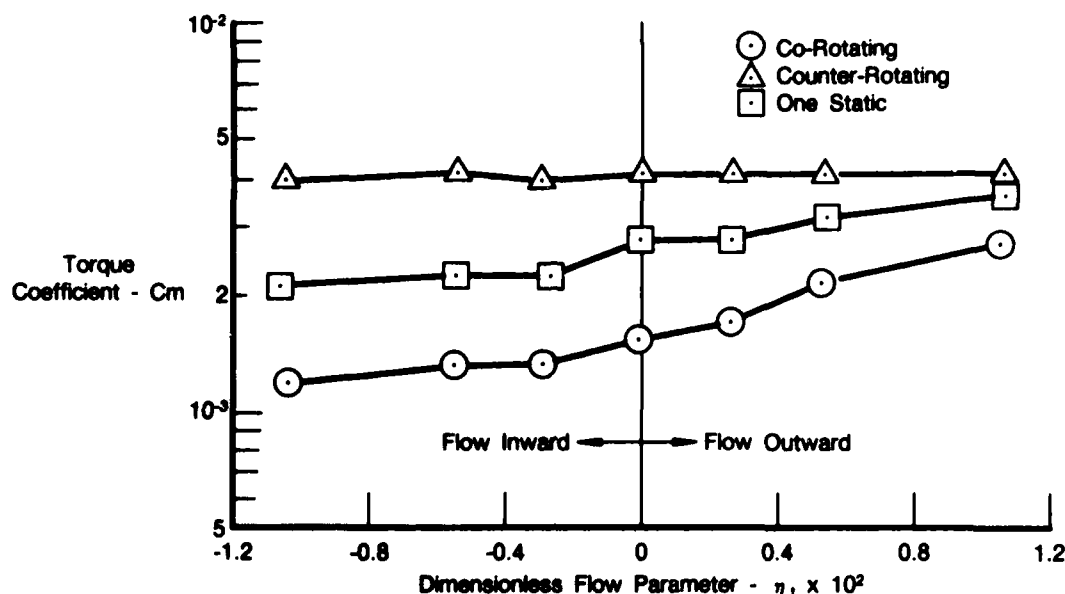
FDA 334562

Figure 16. — Torque Meter Zero-Torque Offset Curve

The observed variations in the torque coefficients ( $C_m$ ) can be attributed, in part, to the differences in the disk cavity flow fields that are induced for the different rotor conditions. In general, the core flow in the cavity between the disks rotates with an angular velocity that is near the average of the sum of the disk speeds. As the fluid is entrained into the disk boundary layer, the tangential component of the core velocity is accelerated from its value outside the disk boundary layer to a value of  $r\Omega$  on the disk surface. Thus, the shear stresses required to accelerate the fluid entering the boundary layer to disk speed are dependent on the magnitude of the tangential velocity component of the core flow relative to the disk. Increasing the core rotation rate decreases the disk friction on the rotating disk(s).

Co-rotating disks induce a core flow with a rotation rate that is generally larger than those caused by the one static and the counter-rotating disk cases. The variations in the torque coefficients with flowrate and injection location found for co-rotating and one static disk cases are attributed to the conservation of the angular momentum of the fluid injected into the disk cavity. The quantity  $r^2\Omega$  tends to be conserved for fluid entering the disk cavity at radius  $r$  and angular rotation rate  $\Omega$ . Therefore, the rotation rate of the fluid decreases with increasing radius for outward flow injected with low angular momentum near the center of rotation. This decrease in rotation rate of the core flow results in an increase in disk friction and therefore higher torque coefficients. For inward flow injected near the disk OD with angular momentum near that of the

disk, the core flow rotation rate increases with decreasing radius. The resulting increase in core rotation rate decreases the disk friction. The relative insensitivity of the torque coefficient to flowrate or flow direction for the counter-rotating disks is not satisfactorily explained. The counter-rotating disks generate a core flow that is almost radial with an average core rotation rate near zero. Thus, the torque coefficients for the counter-rotating disks are independent of flowrate and flow direction.



FDA 334563

Figure 17. — Comparison of Torque Coefficients for Flat Disks with Outflow ( $\eta_t > 0$ ) and Inflow ( $\eta_t < 0$ );  $Re_t = 1.6 \times 10^7$ ,  $S/R_o = 0.328$

## (2) Turbine Disk Model Experiments

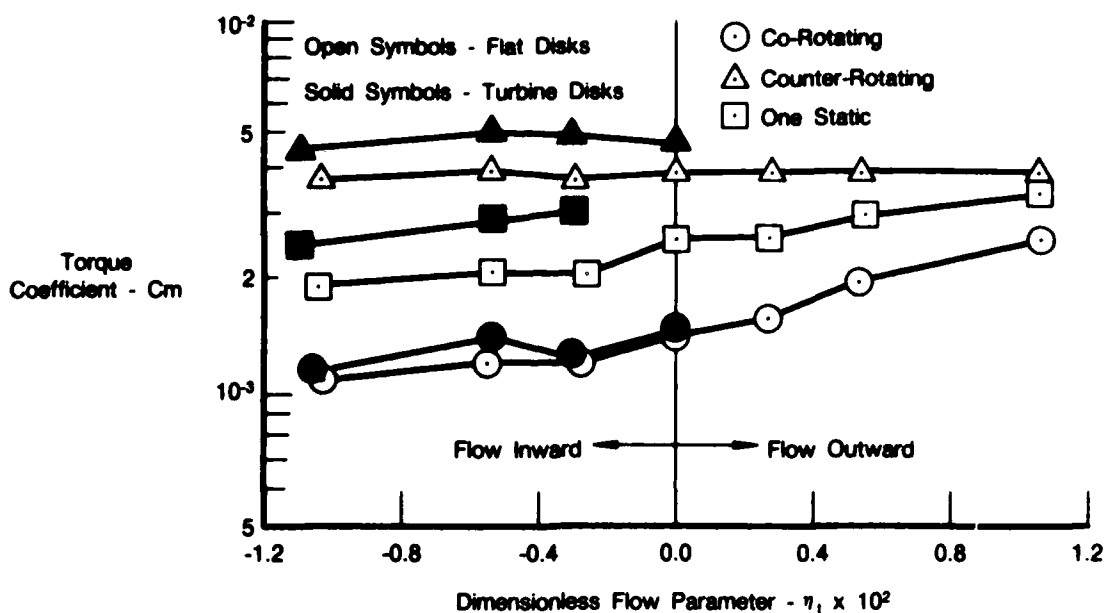
A number of turbine disk model configurations were investigated. These include plain turbine disks, turbine disks with windage diaphragm, turbine disks with bolts, and turbine disks with bolts and bolt covers. Torque measurements for the configuration with bolts and bolt covers were obtained for two different cavity widths. Data was obtained for the disk flow conditions of co-rotation, counter-rotation, and one disk static for all configurations, except for the configuration with a windage diaphragm.

### (a) Turbine Disk Results

Torque coefficients, obtained with the turbine disk model (Figure 5b), are shown in Figure 18. The torque coefficients are plotted versus the nondimensional flow parameter ( $\eta_t$ ). Results from the flat disk experiments are shown for comparison. Observations from the data follow:

- $C_m$  is lowest for co-rotating disks and highest for counter-rotating disks
- $C_m$  is essentially independent of flowrate for counter-rotating disks
- $C_m$  decreases with increasing inward flow rate for co-rotating and one static disk configurations

- $C_m$  is greater for turbine disks than for flat disks for all rotation combinations.



FDA 334564

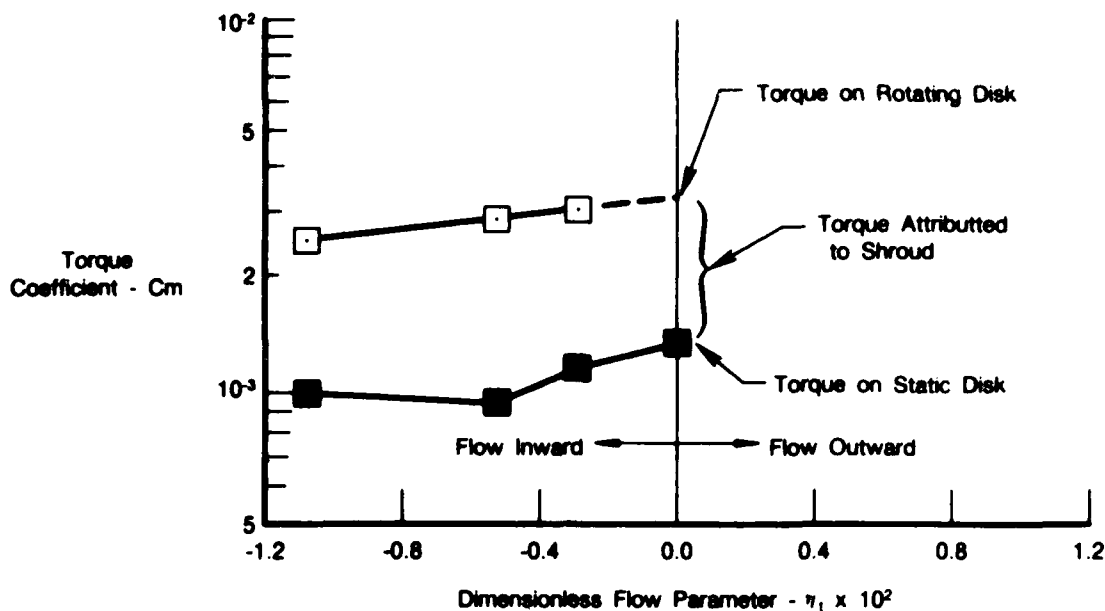
Figure 18. — Comparison of Torque Coefficients for Flat Disks and Turbine Disks;  $Re_1 = 1.6 \times 10^7$ ,  $S/R_0 = 0.328$

These results are consistent with the results from the flat disk experiments. The torque coefficients for the turbine disks are greater than those of the flat disks because of the difference in the total wetted area between the two disk models. The turbine disks have a test surface area which is approximately 15 percent greater than that of the flat disks (Figure 5).

A comparison of the torque coefficients obtained on both turbine disks for the one static disk flow condition is shown in Figure 19. Note that the torque coefficients for the rotating disk are approximately 2.7 times larger than those for the static disk at all flowrates. The conclusion from this comparison is that there is a substantial amount of friction due to the static shroud at the cavity OD.

#### (b) Effects of Windage Diaphragm

The turbine disk model configuration with the windage diaphragm is shown schematically in Figure 6. This device is proposed for use between the high and low rotors of gas turbines with a counter-rotating turbine design. The purpose of a windage diaphragm is to reduce the high torque experienced in counter-rotating cavities by transforming a counter-rotating cavity into two rotating static wall cavities.



FDA 334585

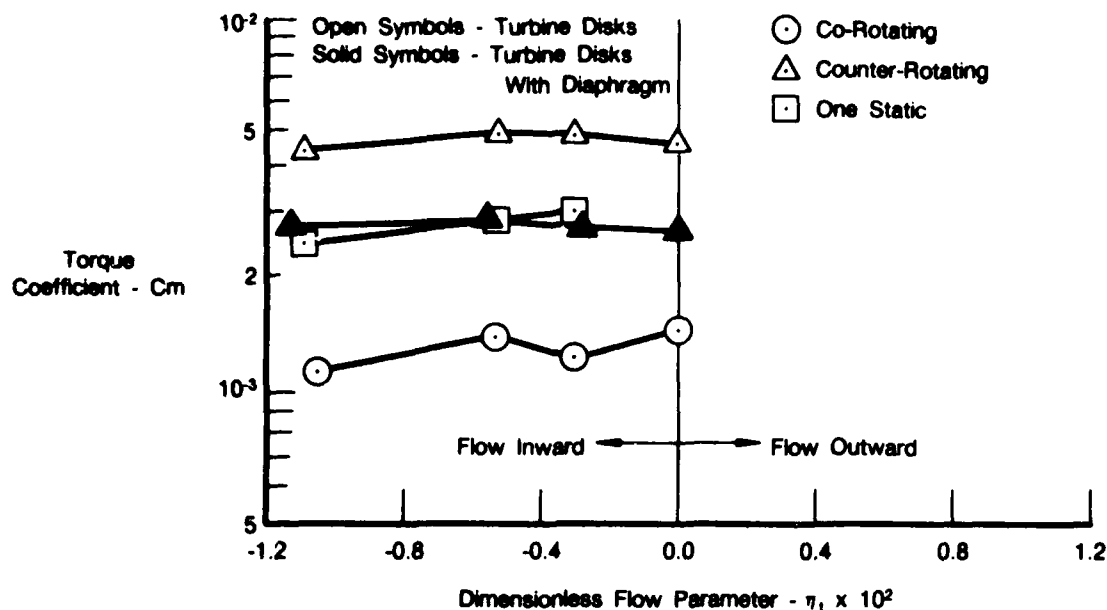
Figure 19. — Comparison of Torque Coefficients on Rotating and Static Turbine Disks;  
 $Re_t = 1.6 \times 10^7$ ,  $S/R_o = 0.328$

The effects of the windage diaphragm on the torque coefficients for the turbine disks are shown in Figure 20. The data shown were obtained at a tangential Reynolds number of  $1.6 \times 10^7$ . Torque coefficients obtained for plain turbine disks are included for comparison. The results shown in Figure 20 indicate that the addition of the windage diaphragm to the counter-rotating cavity reduces the disk torque to the level obtained for the one static disk flow condition. The conclusion from this comparison is that the addition of a windage diaphragm between counter-rotating disks substantially reduces disk torque and, hence, the temperature rise of the flow in the disk cavity.

### (c) Effects of Bolts and Bolts With Covers

The effects of bolts and bolt covers on disk friction was investigated by adding 40 bolts to the turbine disks on a bolt circle 9.25 inches in radius. Torque measurements were obtained with and without partial bolt covers for several flow conditions. The disk configurations and bolt cover geometry are shown in Figures 5c and 5d, respectively.

Torque coefficients for turbine disks with bolts are shown in Figure 21. Results obtained for the plain turbine disks are also shown for comparison. The addition of bolts to the disk significantly (100 percent for the counter-rotating disks and the one static disk) increases the torque compared with the plain disk. The additional torque requirements introduced by the addition of bolts can be attributed to increased boundary layer losses, form drag on the bolt heads and bolt pumping losses. Boundary layer losses are incurred when the bolt heads interrupt the development of the boundary layer near the surface of the disk and cause the boundary layer to be rebuilt on the other side of the bolt heads. The losses due to form drag are caused by the difference in the rotation rate of the protruding bolt heads compared with that of the core flow. This difference in relative speed between the bolts and the fluid also causes fluid to be pumped by the bolt heads, which results in a pumping loss. The total increase in windage due to the addition of bolts can be expected to depend upon the number of bolts and the bolt geometry.



FDA 334566

Figure 20. — Effects of Windage Diaphragm on Torque Coefficients for Turbine Disks;  
 $Re_1 = 1.6 \times 10^7$ ,  $S/R_o = 0.328$

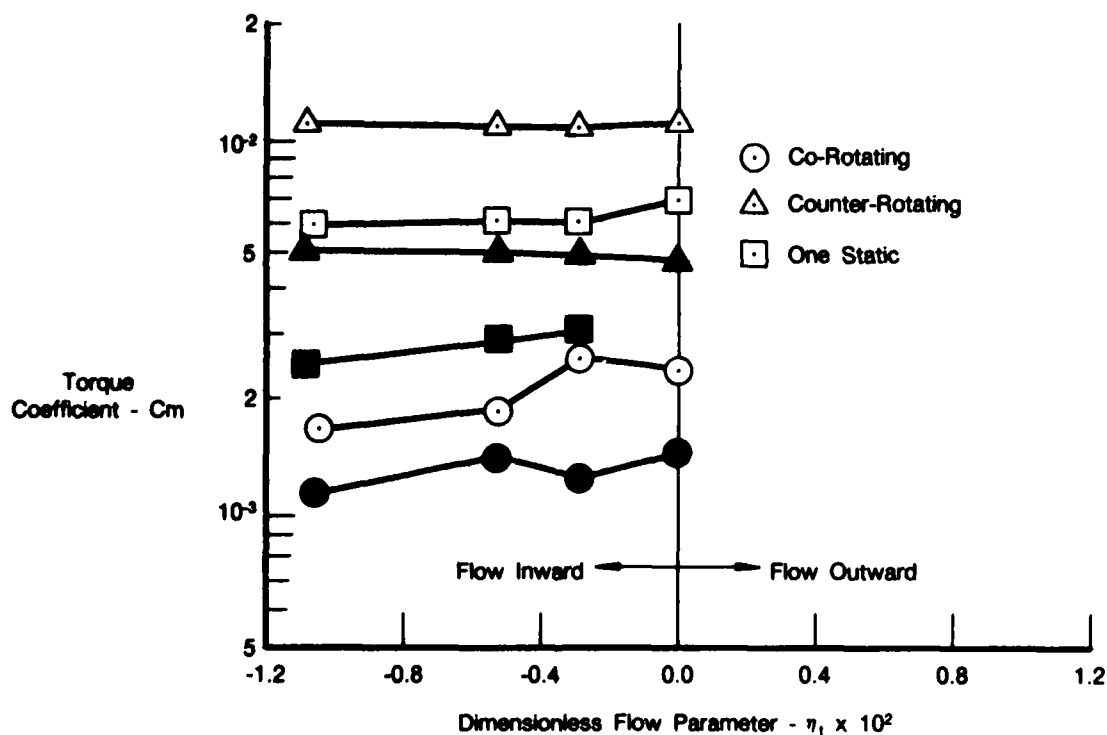
Bolt covers can be used to reduce the windage losses due to bolts. The cover prevents bolt pumping and reduces form drag and boundary layer interruption. However, to reduce weight and design complexity, partial bolt covers are preferred rather than full covers. The partial bolt cover shown in Figure 5d was evaluated in this parametric study. Figure 22 shows the comparison of the torque coefficients obtained for turbine disks with bolts (Figure 5c) and disks with bolts and partial bolt covers (Figure 5d). The results shown in Figure 22 indicate that there is no difference in torque coefficients between the partially covered and the uncovered cases. This result is in agreement with the recent (1986) results of Zimmermann (Reference 3), who measured disk friction with partially covered bolts and fully covered bolts. Zimmermann found that only fully covered bolts reduced disk friction below the level obtained for disks with bolts and disks with partially covered bolts. The conclusion from the present study and Reference 3 is that the partial bolt covers shown in Figure 5d are ineffective in reducing torque due to bolts.

#### (d) Effects of Disk Spacing

Torque measurements were obtained for turbine disks with bolts and bolt covers at two different disk spacings. The nondimensional cavity widths investigated were  $S/R_o = 0.328$  and  $S/R_o = 0.233$ . The disk spacing ( $S$ ) is measured across the cavity at the outer diameter of the disks. The torque coefficients obtained for these two gap widths are shown in Figure 23. The results indicate that there is no appreciable difference in torque coefficients for all flowrates and disk rotation conditions investigated. One reason for this result may be that both of the cavity widths investigated are much larger than the thicknesses of the boundary layers on the disks. At large gap widths, the boundary layers remain separate and do not interact directly with each other. According to Owen (Reference 4), disk spacing will affect disk torque coefficients when the gap is reduced to a point where the boundary layers begin to interact. Owen gives several expressions for estimating flat disk cavity widths for boundary layer interaction to occur and presents data showing the influence of a superimposed throughflow on these estimates. However,

these relationships do not account for the friction on the shroud walls which was shown in Figure 19 to be an appreciable part of the total torque in the rotating disk. The torque measurements alone do not provide enough information to create a complete disk cavity flow model. The conclusion from this comparison is that, in the region of interest, for large and medium aircraft gas turbines, the disk torque is essentially independent of disk spacing.

Symbol	$\Omega_2/\Omega_1$	Configuration
○	1	Turbine Disks With Bolts
●	1	Turbine Disks
△	-1	Turbine Disks With Bolts
▲	-1	Turbine Disks
◻	0	Turbine Disks With Bolts
■	0	Turbine Disks



FDA 334567

Figure 21. — Comparison of Torque Coefficient for Turbine Disks and Turbine Disks With Bolts;  $Re_t = 1.6 \times 10^7$ ,  $S/R_o = 0.328$

Symbol	$\Omega_2/\Omega_1$	Configuration
○	1	Turbine Disks With Bolts and Covers
●	1	Turbine Disks With Bolts
△	-1	Turbine Disks With Bolts and Covers
▲	-1	Turbine Disks With Bolts
□	0	Turbine Disks With Bolts and Covers
■	0	Turbine Disks With Bolts

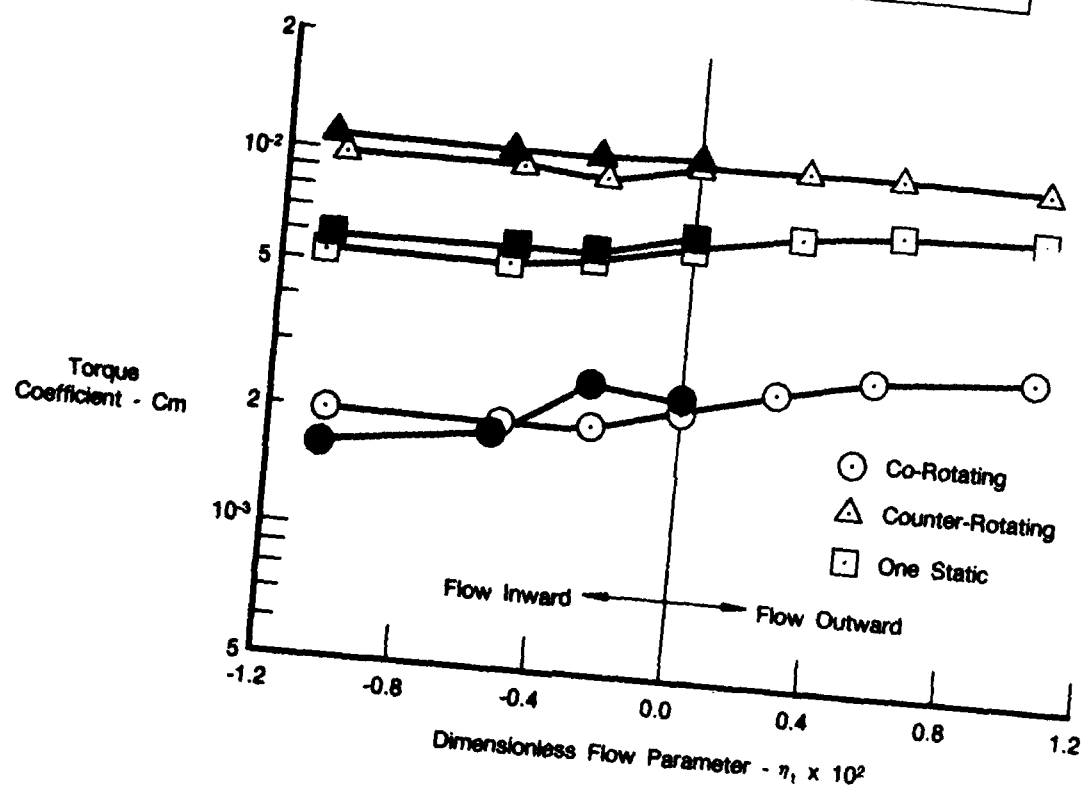
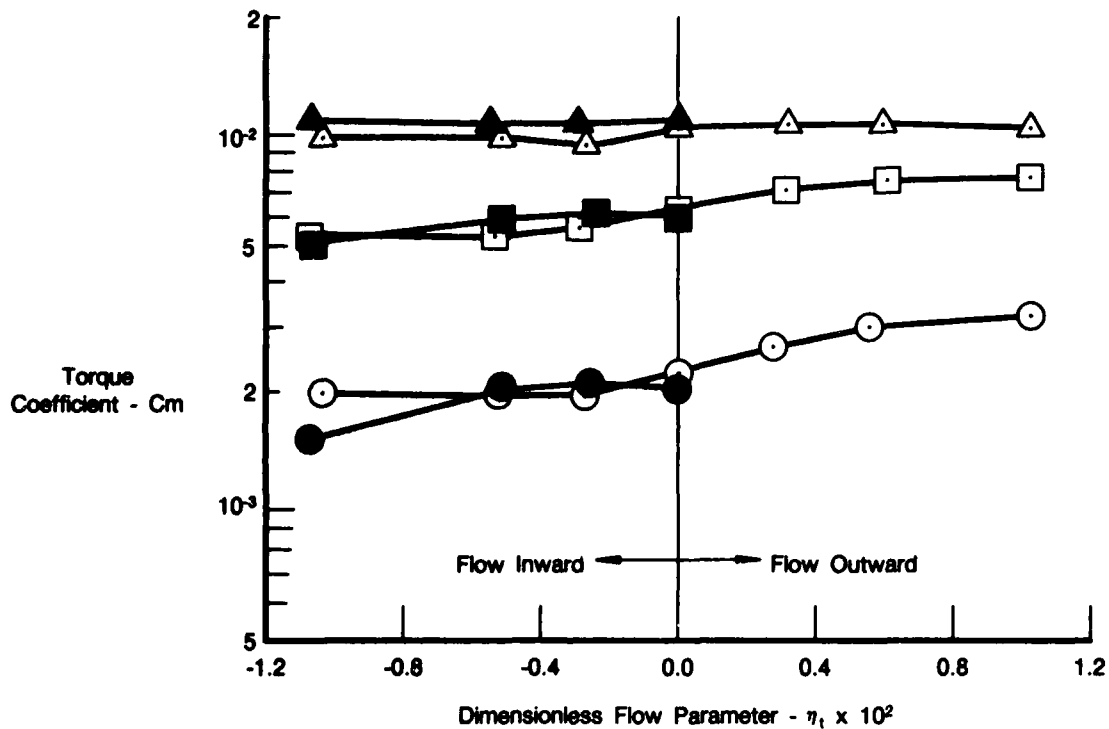


Figure 22. — Comparison of Torque Coefficients for Turbine Disks With Bolts and Turbine Disks With Bolts and Covers;  $Re_t = 1.6 \times 10^7$ ,  $S/R_o = 0.328$

FDA 334588



Symbol	$\Omega_2/\Omega_1$	S/R <sub>o</sub>
●	1	0.233
○	1	0.328
▲	-1	0.233
△	-1	0.328
■	0	0.233
□	0	0.328



FDA 334569

Figure 23. — Comparison of Torque Coefficient for Turbine Disks With Bolts and Bolt Covers at Two Disk Spacings;  $Re_t = 1.6 \times 10^7$

#### d. Results of Radial Pressure Measurements

Radial pressure measurements were obtained at 17 different radial locations for the flat disk and the turbine disk experiments. The measurements were used to determine cavity core rotation levels with disk rotation conditions, flowrate, and injection location. The core rotation rate was shown by the above results to influence disk torque.

In the core flow, a radial pressure gradient occurs due to the rotation of the fluid. This radial pressure gradient is impressed on the disk boundary layer and opposes the centrifugal forces of the fluid in the boundary layer. For a given disk speed, the direction and amount of fluid pumped through the boundary layer is dependent upon the magnitude of the radial pressure

gradient. If the pressure gradient is strong enough to overcome the centrifugal forces on the fluid in the boundary layer, the fluid will be pumped radially inward along the disk, whereas fluid is pumped outward for weaker pressure gradients. At some intermediate value, the pressure gradient and the centrifugal forces can be in equilibrium and no disk pumping occurs. This situation arises when the core rotates as a solid body with an angular rotation rate equal to that of the disk.

In general, the rotation rates of the induced core flows in the cavities between turbine disks are somewhat less than that of the disk and the disk pumping is radially outward. The magnitude of the core rotation rate which influences the disk windage is dependent upon the flowrate, injection location, and the disk boundary conditions. The core rotational velocity ( $V$ ) can be related to the local disk rotational velocity by:

$$V = kr \Omega \quad (5)$$

where:

- $r$  = local radius
- $\Omega$  = rotation rate of the disk
- $k$  = core rotation factor.

For  $k=1$ , the core rotates as a solid body with the disk. For the types of cavity flows found in the turbine area,  $k$  is usually less than one.

The radial pressure gradient imposed by a cavity core flow described by equation 5 is given by:

$$dp/dr = k^2 \Omega^2 r \rho \quad (6)$$

Equation 6 contains the principal terms from the radial momentum equation in cylindrical coordinates for rotating flow with negligible radial and axial velocities. If the radial distribution of the core rotation factor ( $k$ ) is known, equation 6 can be integrated to obtain the pressure drop across the disk.

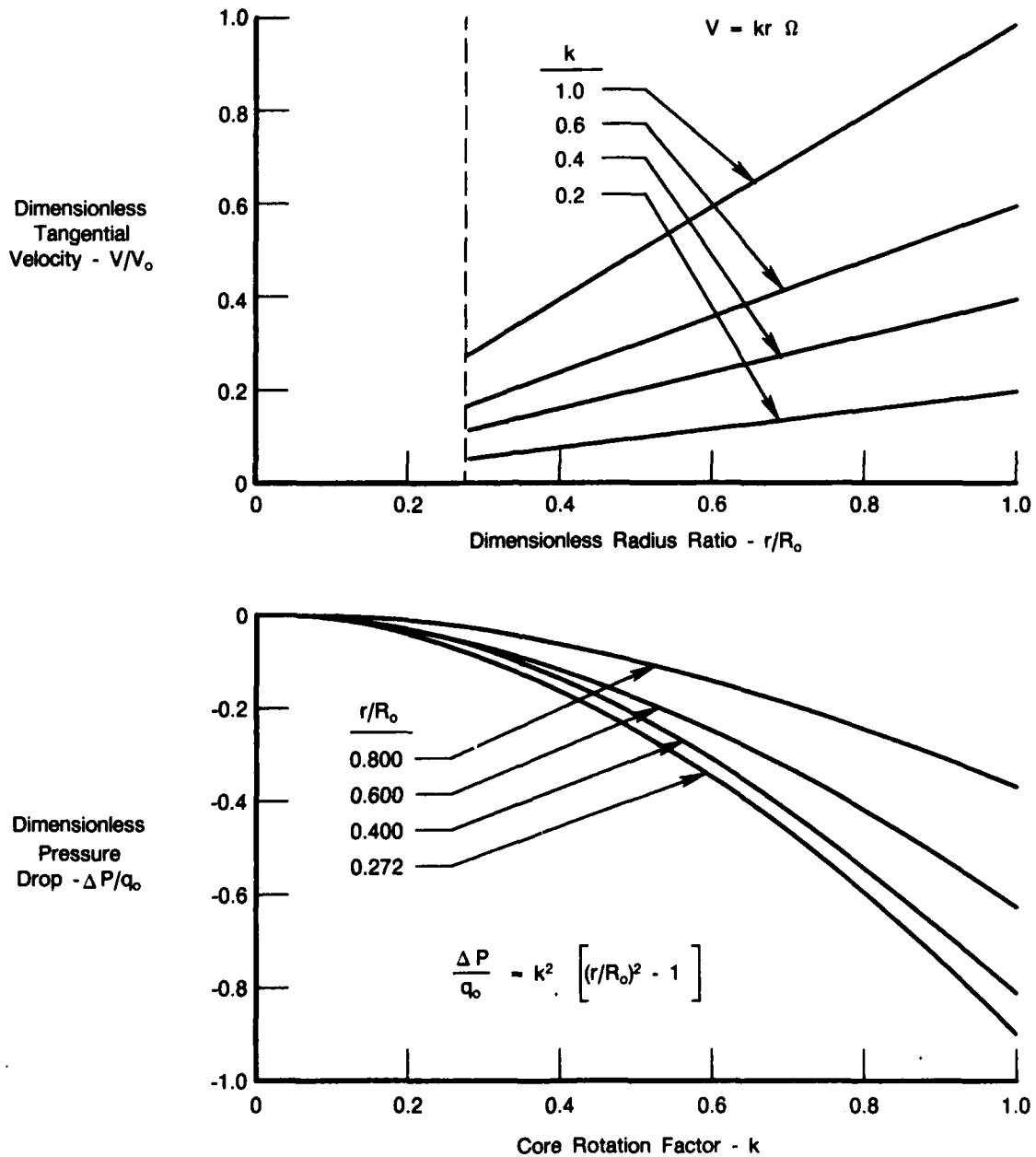
Several dimensionless core tangential velocity profiles for various values of  $k$  constant at all radii are shown in Figure 24. The core tangential velocity divided by the rim speed is plotted versus the radius ratio. Figure 24 also shows the dimensionless pressure drop from the disk OD at different radii for constant values of  $k$  from zero to one. These profiles were obtained by integrating equation 6 from radius  $r$  to the disk rim. In general,  $k$  will be a function of the radius, flowrate, injection location, and disk boundary conditions.

### **(1) Results for Flat Disks and Turbine Disks**

Dimensionless radial pressure distributions measured for flat disks are presented in Figure 25. Results are shown for both inward and outward flow with disk conditions of co-rotation, counter-rotation, and one disk static. The results shown in Figure 25 indicate that:

- The pressure difference from the disk OD to the hub is greatest for co-rotating disks and least for counter-rotating disks for both inward flow and outward flow

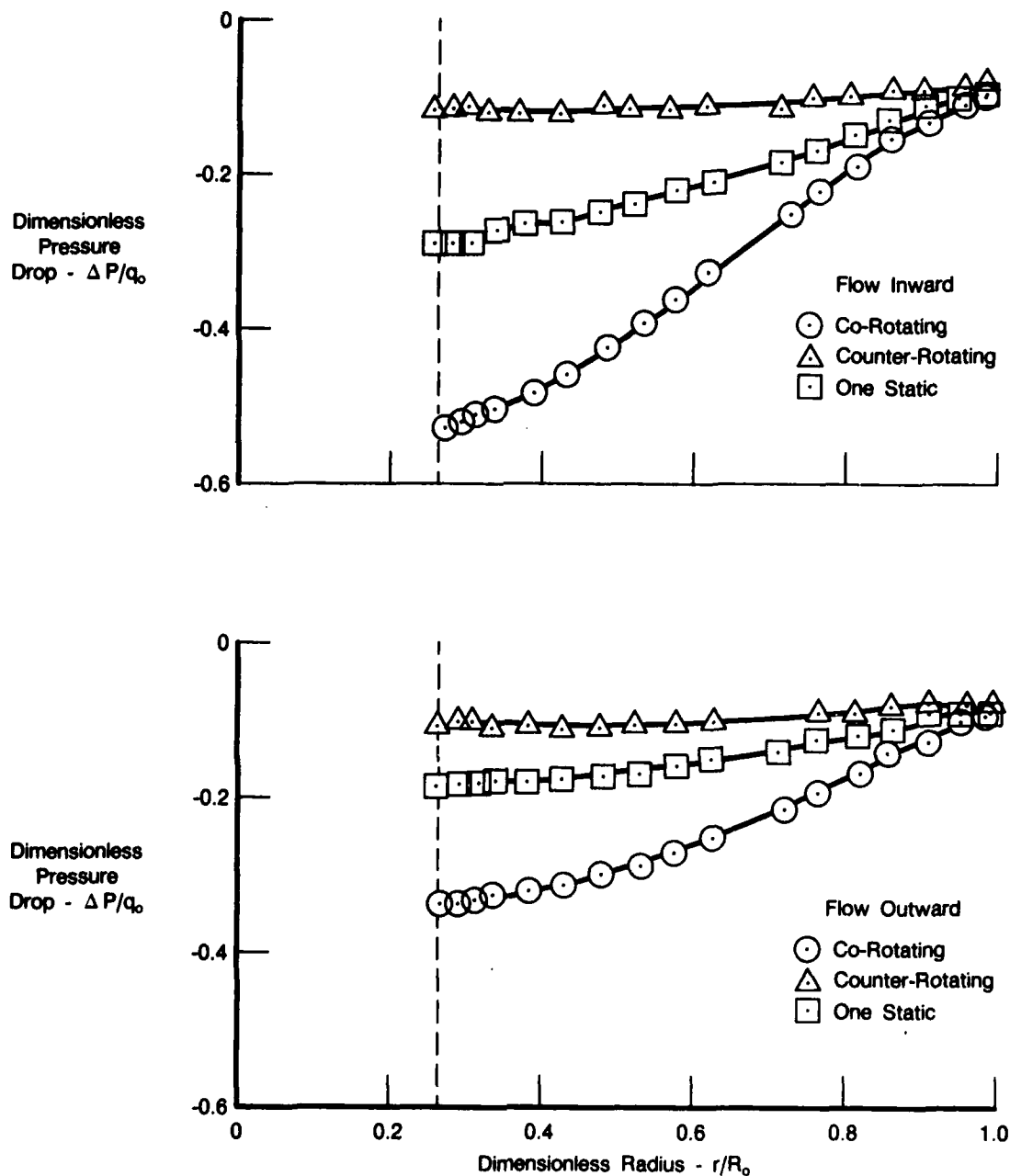
- The pressure difference from the disk OD to the hub is independent of flow direction for counter-rotating disks
- The pressure difference from the disk OD to the hub is greater for inward flow than for outward flow for co-rotating and one static disk conditions.



FDA 334570

Figure 24. — Tangential Velocity Profiles and Radial Pressure Drop for Various Values of the Core Rotation Factor  $k$

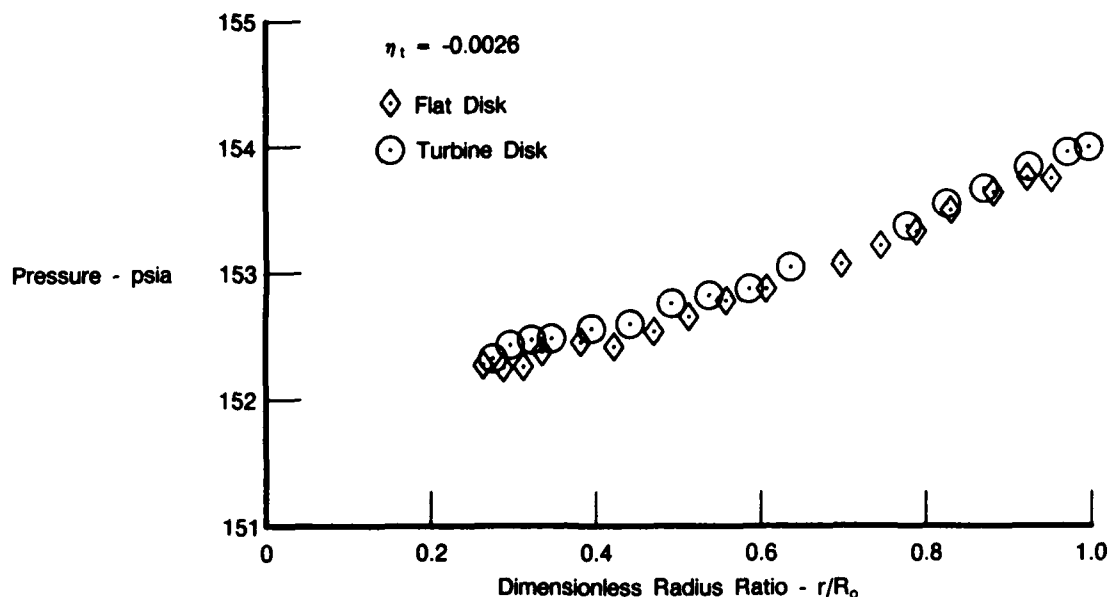
The differences in pressure drop for inward flow versus outward flow, shown in Figure 25 for the co-rotating and the one static disk cases, are due to the conservation of angular momentum of the fluid injected into the cavity. For flow inward, the core rotation rate increases with decreasing radius resulting in a larger pressure drop, when compared with the pressure drop obtained for the same amount of flow outward in the cavity. For inward flow, the pressure drop will increase with increasing flowrate.



FDA 334571

Figure 25. — Radial Pressure Drop for Flat Disks With Flow Inward and Flow Outward;  
 $Re_i = 1.6 \times 10^7$ ,  $S/R_0 = 0.328$ ,  $\eta_f = 0.0026$

The radial pressure distributions obtained for the turbine disks were approximately the same as those of the flat disks. Figure 26 compares the measured pressure for flat disks and turbine disks for the one static disk case with flow inward. The conclusion from this comparison and the torque measurements is that the increased torque coefficients measured for the turbine disks, compared with those of the flat disks, are due to the larger surface area of the turbine disks and not to a change in the disk cavity aerodynamics.



FDA 334572

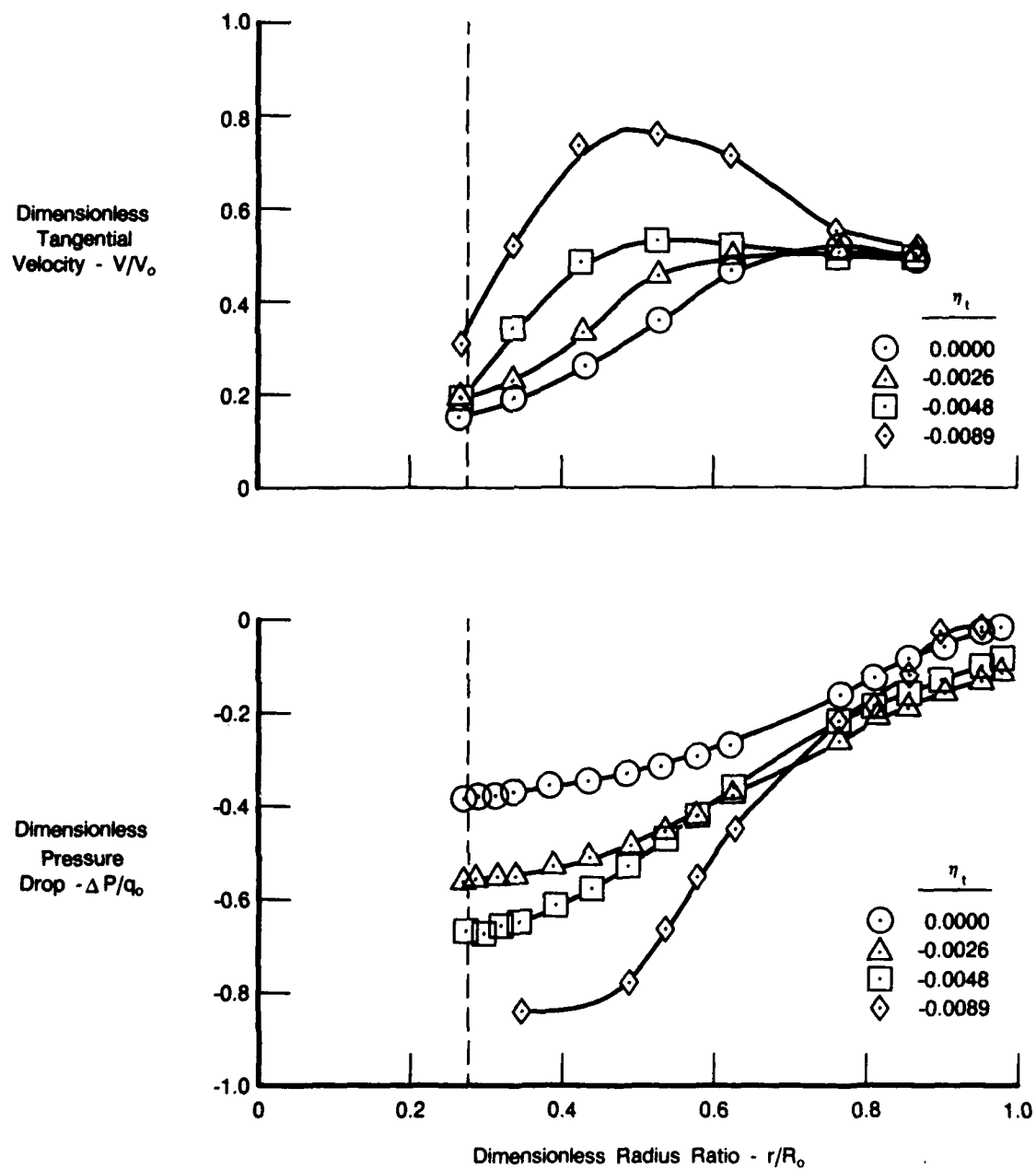
Figure 26. — Comparison of Radial Pressure Distribution Between Flat Disks and Turbine Disks With One Disk Static; Flow Inward,  $Re_t = 1.6 \times 10^7$ ,  $S/R_0 = 0.328$

## (2) Tangential Velocity Profiles for Turbine Disks

Tangential velocity profiles in the core region were deduced from the measured radial pressure distributions for the turbine disks. The profiles were obtained for four inward flowrates at a tangential Reynolds number of  $1.6 \times 10^7$ . Velocity profiles for co-rotating, one static, and counter-rotating disk flow conditions are presented in Figures 27, 28, and 29, respectively. The dimensionless radial pressure drops from which the velocity profiles were obtained are also shown. The tangential velocity profiles shown in Figures 27 through 29 were obtained by integrating equation 6 over incremental values of the radius, assuming a constant value of  $k$  within the interval. The end points of the interval coincided with every other pressure tap on the disk. The physical interval length was approximately 0.9 inch.

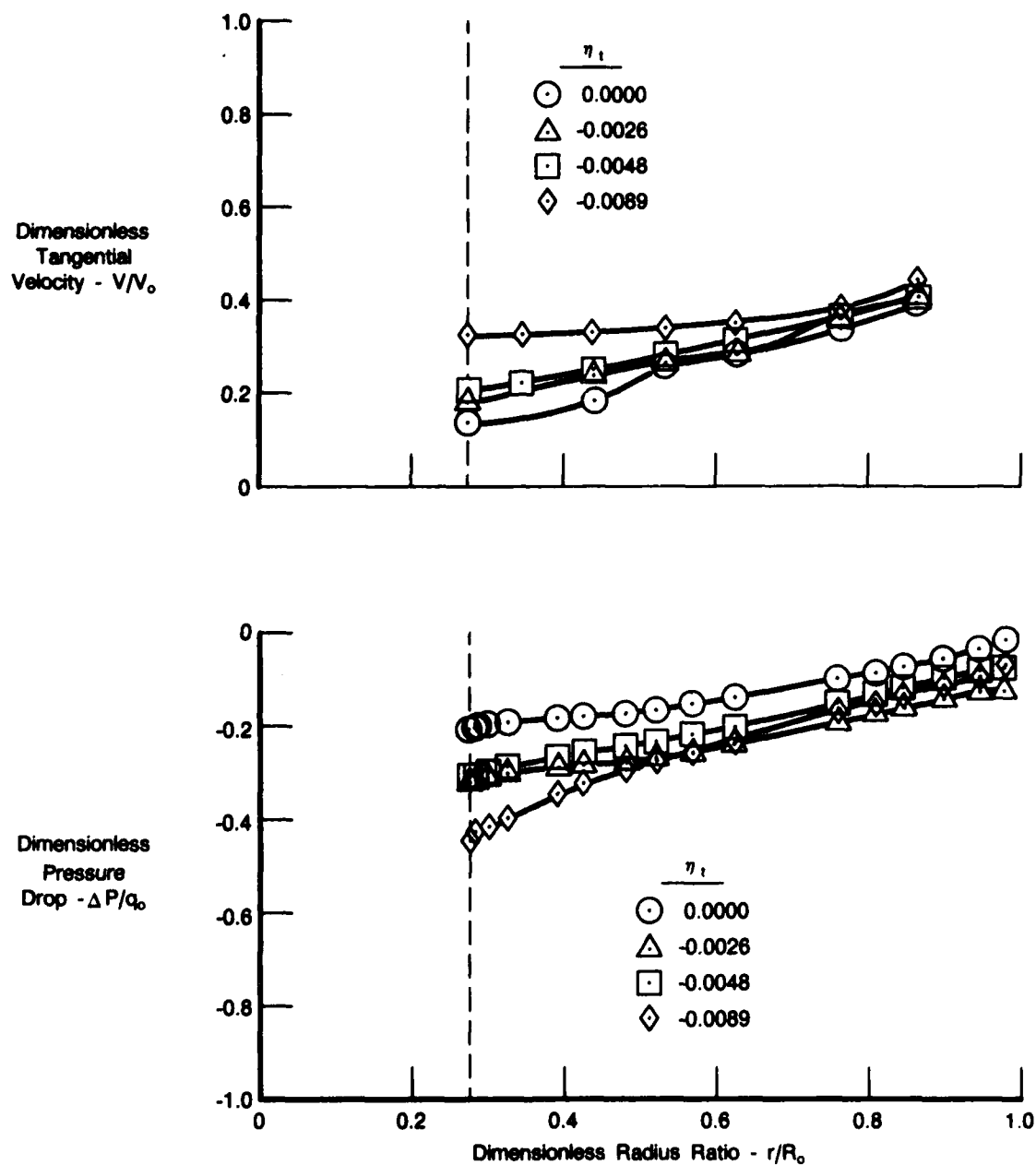
The results shown in Figures 27 and 28 for the co-rotating and the one static disk cases indicate that the core tangential velocity and rotation rate increase with increasing flowrate radially inward. This increase in core rotation rate results in a decrease in the relative speed between the disk and the fluid and hence a decrease in the disk torque coefficient as shown in Figure 18. The tangential velocity profile for the core flow with co-rotating disks at  $\eta_t = -0.0089$  has velocities greater than the local disk speed. For this condition, the local torque at radii, where core tangential velocity is greater than  $\Omega r$ , accelerates the disk. The results presented in Figure 29 for the counter-rotating disks show that the core flow has a very low rotation rate which is essentially independent of flowrate. This result indicates that the relative speed between the disk

and the core fluid is almost equal to the disk speed and causes the high torque coefficients shown in Figure 18.



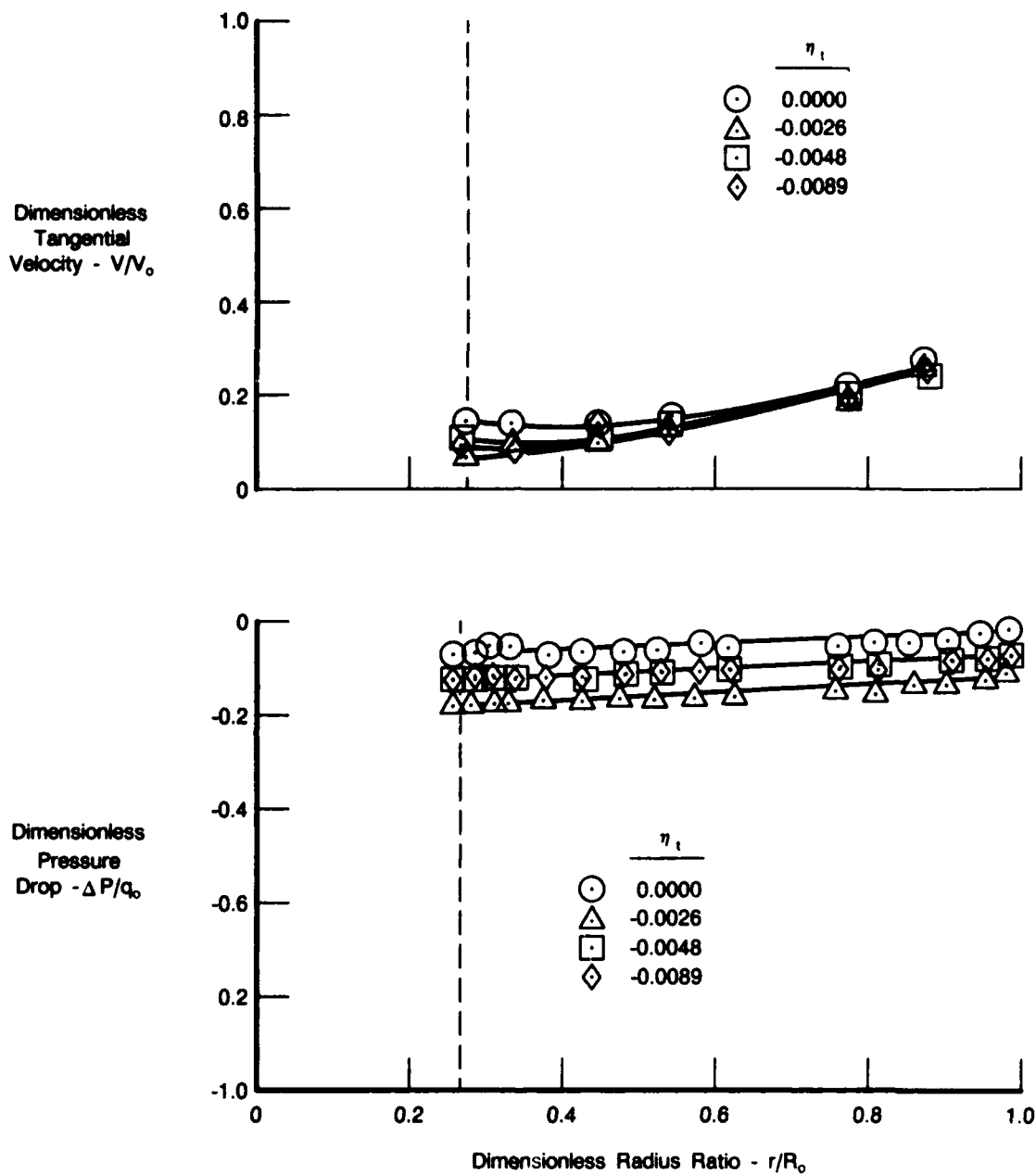
FDA 334573

Figure 27. — Tangential Velocity Profiles and Radial Pressure Drop for Co-rotating Turbine Disks; Flow Is Inward,  $Re_t = 1.6 \times 10^7$



FDA 334574

Figure 28. — Tangential Velocity Profiles and Radial Pressure Drop for Turbine Disks With One Disk Static; Flow Is Inward,  $Re_t = 1.6 \times 10^7$



FDA 334575

Figure 29. — Tangential Velocity Profiles and Radial Pressure Drop for Counter-Rotating Turbine Disks; Flow Is Inward,  $Re_t = 1.6 \times 10^7$

### 3. CORRELATION OF RESULTS

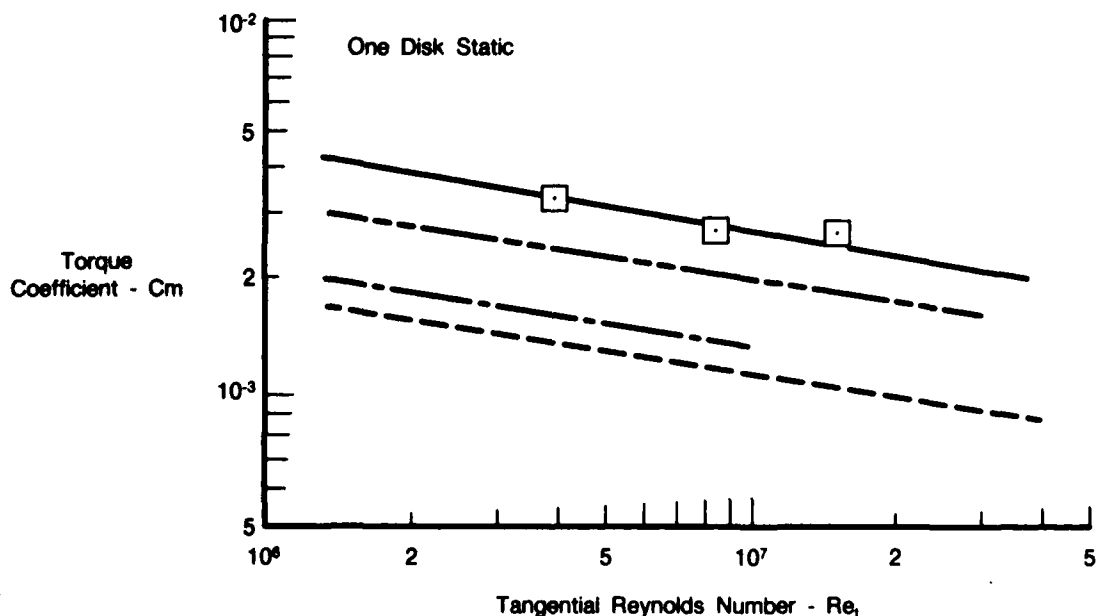
Disk flow problems are important in the field of fluid mechanics because of the numerous technical applications. Research published in the open literature has been concerned primarily with disk flows involving the classic "free" disk and those with the single smooth disk in a



stationary housing. Recently, studies have focused on more practical disk problems involving pairs of coaxial disks which are free to rotate independently of each other. The lack of information in the open literature for these types of disk problems, especially disk friction information, leaves little for comparison with the results obtained in this investigation for the co-rotating and the counter-rotating disk experiments. However, literature is available to compare the one static disk case study results.

A comparison of the torque coefficients obtained in this investigation with those obtained by Schultz-Grunow (Reference 2) and Zimmermann et al. (Reference 3) is presented in Figure 30. The torque coefficients for a free disk and a shrouded disk, predicted with a momentum integral analysis, are also presented. All results shown in Figure 30 were obtained for flat disks and zero flowrate.

Symbol	Source	S/R <sub>0</sub>
□	Present Data, Flat Disks	0.328
---	Zimmerman et al. (Ref. 3)	0.2375
---	Schultz-Grunow (Ref. 2)	0.020
---	Cm = 0.073 Re <sub>t</sub> <sup>-0.2</sup> (Ref. 2)	Free Disk
---	Cm = 0.0311 Re <sub>t</sub> <sup>-0.2</sup> (Ref. 2)	Disk in Housing



FDA 334576

Figure 30. — Comparison of Present Data With Classical Disk Theory, Schultz-Grunow Data (Reference 2) and Zimmermann, et al. Data (Reference 3); Flat Disks,  $\eta_t = 0$

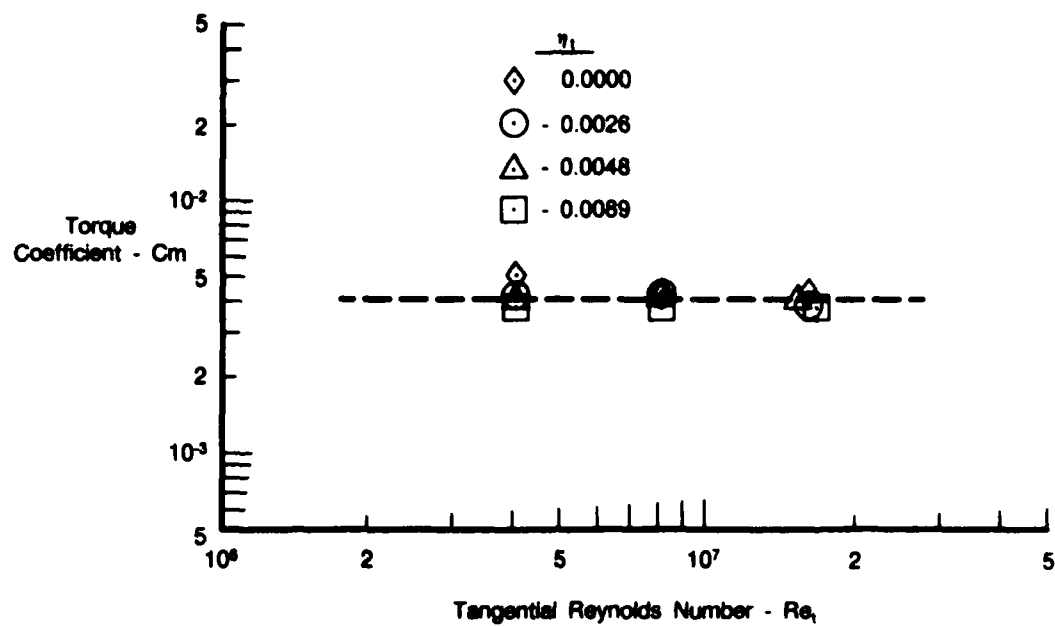
Several observations can be drawn from these results. The first observation is that disk spacing has a large effect on the torque coefficient. As disk spacing is increased from  $S/R = 0.02$

to 0.24 and 0.33, the torque coefficient increases. Also, all data lie between the torque coefficients predicted by the free disk and the disk in housing theory. This is interesting because the expressions for the torque coefficients resulting from these classical disk theories are independent of the disk spacing and therefore represent two limiting cases.

These effects of disk spacing on torque coefficient for the flat disks differ from those shown in Figure 23 for the turbine disks with bolts and bolt covers at two different disk spacings. For the geometries with bolts, there was no observed difference in the torque coefficients when the dimensionless disk spacing was reduced from  $S/R_o = 0.328$  to  $S/R_o = 0.233$ . For the flat disks there is almost 40 percent difference in torque coefficients shown in Figure 30 between the flat disk results obtained in this investigation at  $S/R_o = 0.328$  and those obtained by Zimmermann at  $S/R_o = 0.2375$ .

Limited literature is available to compare results with the co-rotating and counter-rotating co-planar disks. The work accomplished in this area has been primarily concerned with the determination and specification of the flow field generated between the disks, and torque measurements are not reported. Szeri et al. (Reference 5) have made Laser-Doppler velocity measurements for laminar flow between co-rotating, counter-rotating, and one static disk cases, and Dijkstra and van Heijst (Reference 6) have numerically and experimentally investigated the flow for these disk conditions with the disks rotating at nonequal rotation rates. The effects of throughflow was also reported in Reference 5 and the flow field results were correlated with a nondimensional flow parameter, similar to the  $\eta_t$  parameter, equation 3, used in this investigation.

The results of this investigation indicate that disk friction for counter-rotating disks is independent of tangential Reynolds number and flowrate. The torque coefficients obtained for counter-rotating flat disks at three tangential Reynolds numbers with various amounts of throughflow (inward) are presented in Figure 31. These results differ from those for the single rotating disk in that  $C_m$  does not decrease with increasing tangential Reynolds numbers. One possibility for this insensitivity to Reynolds number is that high levels of turbulence may be generated by the merging of the flow from the boundary layers on the two disks. Ingestion of this turbulent flow into the disk boundary layers will increase the local wall friction.



FDA 334577

Figure 31. — Effects of Scaling Parameter for Counter-rotating Flat Disks; Flow Inward

## SECTION IV

### TURBINE RIM SEAL INGESTION EXPERIMENTS

#### 1. INTRODUCTION

##### a. Problem

The internal air flow system of a gas turbine engine is used to extract and distribute cooling air from the main gaspath in the compressor region to provide an acceptable thermal environment in the turbine region. The turbine air seals are an important component in the internal air flow system because the seals limit the ingestion of hot flow from the main gaspath in the turbine into the turbine disk cavities. The amount of cooling air supplied to the seals to maintain acceptable metal temperatures also influences the thrust and specific fuel consumption of the gas turbine. The rim seal performance becomes more critical as the gaspath air temperatures through the turbine increase.

A limited amount of rim seal data is available in the open literature for the Reynolds number range of interest. This dearth of information makes it difficult to compare the performance of candidate seals and conduct parametric design studies. As a result, rim seal ingestion experiments were requested and proposed as part of the present Disk Pumping Test Program.

##### b. Objective

The objectives of this investigation were to document and correlate the rim seal ingestion characteristics for one class of rim seals used in aircraft gas turbines. The class of seals selected is that occurring on the downstream side of a turbine disk where the boundary layer along the disk flows directly into the seal gap.

##### c. Approach

To achieve these objectives, an experimental investigation was conducted to obtain heat transfer and aerodynamic data for a number of rim seal geometries and flow conditions. A mass transfer analogy, i.e. the use of a trace gas, was chosen to characterize the rim seal ingestion characteristics. A mass transfer process can be measured with greater accuracy in the boundary conditions than the corresponding thermal process. The application of the mass transfer analogy to determine equivalent temperature field distributions has been well documented (References 11, 12, and 13). The main assumption in this analogy is that the turbulent Prandtl number (governing heat transfer) and the turbulent Schmidt number (governing mass transfer) are approximately equal at all locations in the flow. This is a good assumption when the flow is turbulent and the molecular weight of the trace gas is close to that of the main gas (i.e., air). Although other gases, e.g. ethylene, with a molecular weight closer to air have been used to study aerodynamic mixing, CO<sub>2</sub> was chosen for reasons of safety and because of the overwhelming dominance of turbulent mixing over molecular diffusion in the rim seal ingestion experiments. The radial and axial gaps for the seals were varied from a baseline configuration and from a simplified concept configuration. A cooling effectiveness was determined for each configuration and flow condition from the CO<sub>2</sub> concentration and flowrate measurements. The results were compared on an absolute basis, with previous measurements, and with a turbulent diffusion analysis.

## 2. DISCUSSION OF EXPERIMENT AND RESULTS

### a. Apparatus

The rim seal ingestion experiments were conducted with the turbine rim seal assembly (Figure 7) installed in the internal air systems facility, illustrated in Figures 1 and 2. The turbine rim seal assembly employs many of the components previously used for the turbine disk assembly shown in Figure 3. The turbine rim seal configurations are attached to the flat turbine disks, as shown in Figure 8. The outside diameter of the Configuration 1 static disk was machined between experiments to obtain the desired radial gap between the rotating and static disks. A spacer was used between components on the static disk to obtain the desired axial gap (or overlap). Seal geometries are presented in Figure 32.

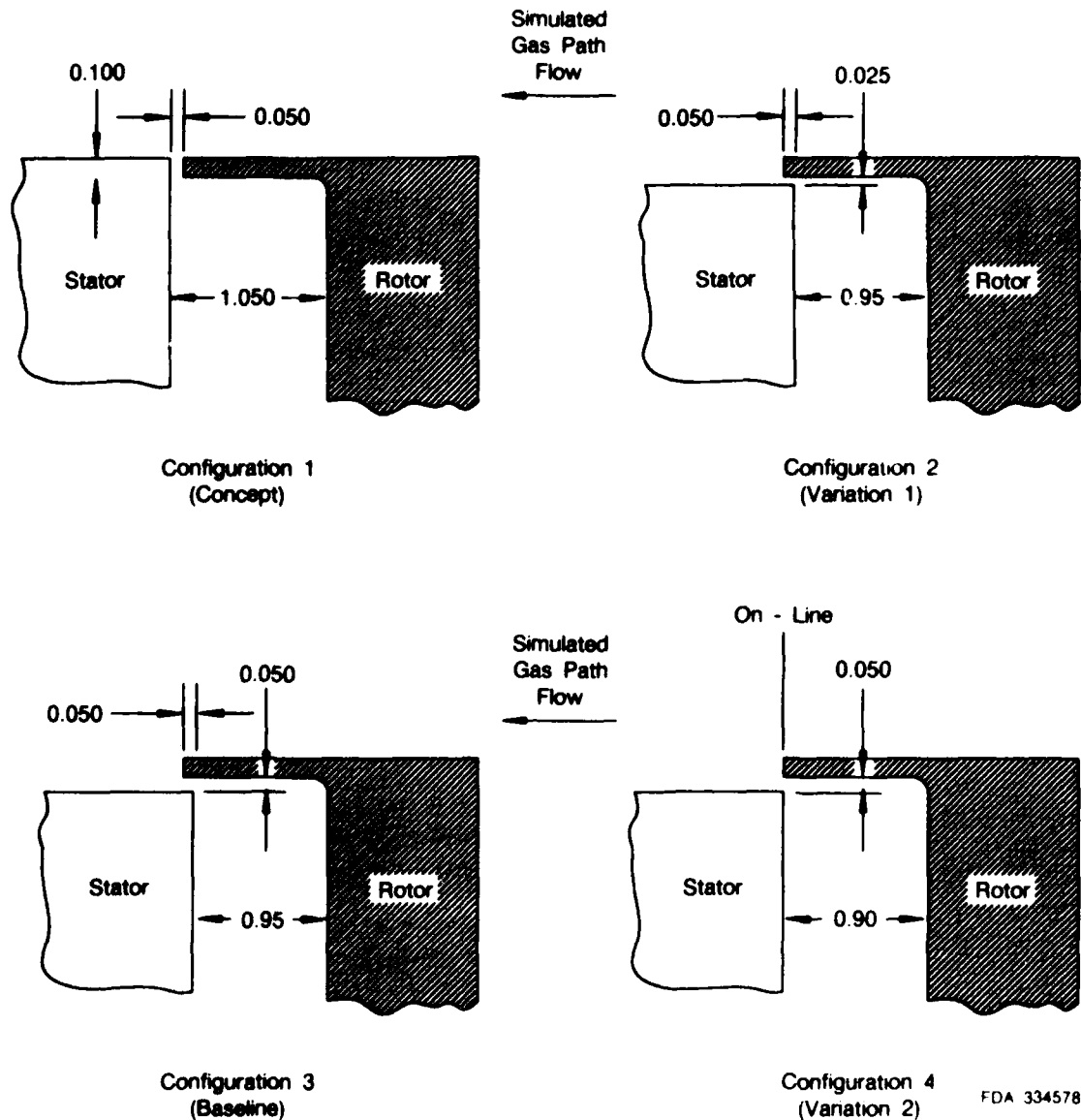


Figure 32. Rim Seal Geometries and Dimensions

## b. Measurement Technique

A CO<sub>2</sub> trace gas measurement technique was used to determine the cooling effectiveness of the turbine rim seal for each combination of seal configuration and flow condition. The trace gas measurement locations were shown in Figure 9, and the measurement apparatus was defined in Section II.

A sketch of a rim seal model with flow and geometric nomenclature is presented in Figure 33. For this model, all the flowrates in the rim cavity, i.e. purge ( $\dot{m}_p$ ), ingested ( $\dot{m}_i$ ), and ejected ( $\dot{m}_e$ ) are defined to be positive in the direction of the adjacent arrow. Definitions of the concentration nomenclature and radial dimensions of the rim seal are also shown in Figure 33. Equations for the conservation of mass and the conservation of the trace gas in the rim cavity, for the cooling effectiveness parameter ( $\phi$ ) and for a dimensionless flow parameter ( $\eta_f$ ) are also presented in Figure 33.

## c. Expected Results

The expected variation of rim seal cooling effectiveness parameter with purge (coolant) flowrate is shown in Figure 34. For no coolant flow, the main gaspath fluid would be ingested into the cavity and recirculated to the main gaspath. All the fluid in the rim seal cavity would be from the main gaspath and hence the cooling effectiveness parameter would be zero. When the purge (coolant) flowrates are increased sufficiently such that all the fluid pumped by the rim seal rotating disk is less than the coolant flowrate supplied, the cooling effectiveness parameter should approach or equal unity. At purge (coolant) flowrates between these two limits, the interaction of the flows in the cavity with the seal geometry and the coolant flowrate will determine rim seal cooling effectiveness. Each rim seal configuration will have a variation of cooling effectiveness with coolant flowrate for fixed disk speed and main gaspath conditions.

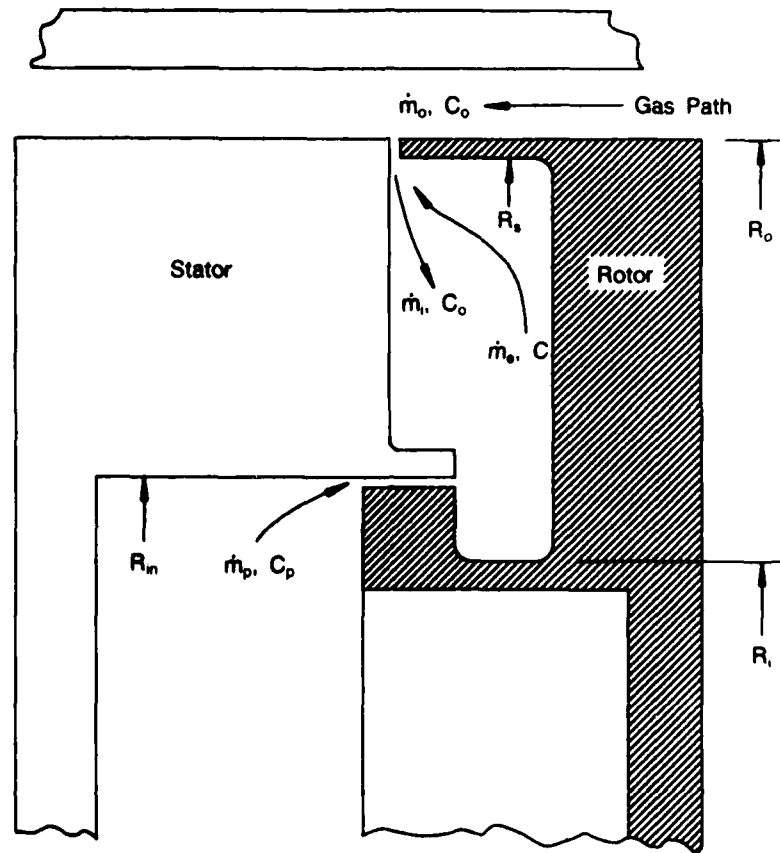
## d. Results for Concept Geometry

The variation of the cooling effectiveness parameter ( $\phi$ ) with the dimensionless coolant flowrate ( $\eta_f$ ) for the concept geometry (Configuration 1) is presented in Figure 35. Data were obtained for a tangential Reynolds number of  $5.1 \times 10^6$ . The main gaspath flow ( $\dot{m}_i$ ) was injected with two levels of swirl,  $V_{\phi i}/\Omega R_{\phi i}$ ,  $V_{\phi i} = 1.0$  and  $2.0 R_{\phi i}\Omega$ . The variation of the gaspath flow conditions were varied to determine the effects on the ingestion process. The cooling effectiveness parameter is essentially independent of the main gaspath swirl level for these flow conditions.

Exploratory experiments were conducted prior to these tests to determine the flow limits for the facility and the flow limits through each component. The maximum simulated main gaspath flowrate is limited to approximately 0.5 pounds/second. As a result, the tangential Reynolds number was limited to  $5 \times 10^6$  to avoid recirculation of test chamber gas into the main gaspath. The maximum purge flowrates were also maintained at a fraction of the simulated main gaspath flowrate.

## e. Results for Three Rim Seal Geometries

The combinations of configuration, main gaspath swirl velocity ratio, tangential Reynolds number, disk rpm and facility pressure for which data were obtained are shown in Table 2. The baseline flow condition has a tangential Reynolds number of  $5 \times 10^6$  and a gaspath swirl ratio equal 1.0. The tangential Reynolds number was decreased to  $2.5 \times 10^6$  and the gaspath swirl velocity ratio was increased and decreased to values of 2.0 and 0.6, respectively.



#### Conservation of Mass

$$\dot{m}_p - \dot{m}_e = \dot{m}_i$$

#### Conservation of CO<sub>2</sub>

$$C_p \dot{m}_p - C \dot{m}_e = C_o \dot{m}_i$$

#### Cooling Effectiveness Parameter, $\phi$

$$\phi = \frac{C - C_o}{C_p - C_o} = \left[ \frac{1}{1 - (\dot{m}_i / \dot{m}_p)} \right]$$

#### Dimensionless Flow Parameter, $n_1$

$$n_1 = \left( \frac{\dot{m}_p}{4 \pi \mu R_c} \right)^{0.8}$$

#### Parameters

$\dot{m}_p$  = Purge Flow

$\dot{m}_e$  = Ejected Flow

$\dot{m}_i$  = Ingested Flow

$\dot{m}_c$  = Gas Path Flow

$C_p$  = CO<sub>2</sub> Concentration of Purge

$C$  = Average Cavity CO<sub>2</sub> Concentration

$C_o$  = Gas Path CO<sub>2</sub> Concentration

$R_o$  = Rotor Rim Radius = 10.51 in.

$R_s$  = Seal Radius = 10.41 in.

$R_m$  = Cavity Inlet Radius = 8.22 in.

$R_i$  = Cavity Inside Radius = 7.65 in.

FDA 334579

Figure 33. — Definitions of Seal Cooling Effectiveness Parameter, Dimensionless Flow Parameter, and Cavity Flow and Geometric Parameters

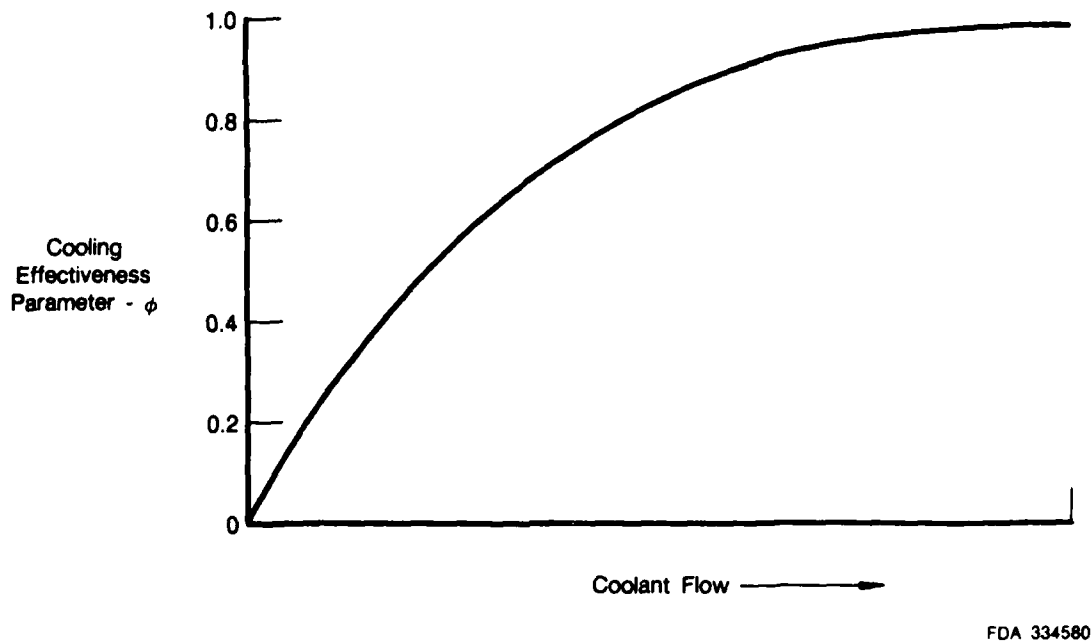


Figure 34. — Typical Seal Cooling Effectiveness Parameter as a Function of Purge Flowrate

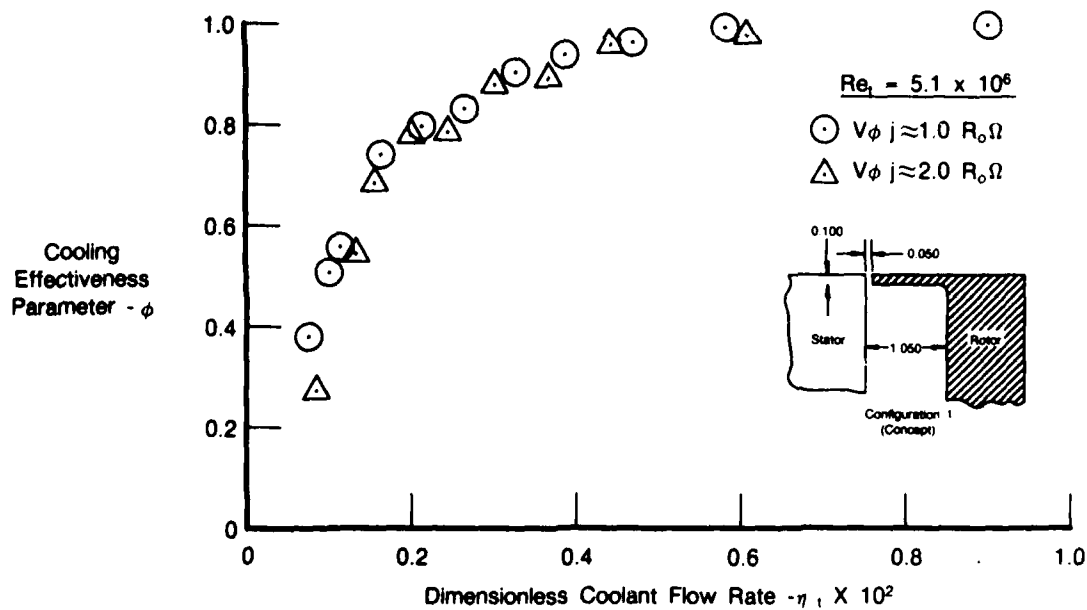
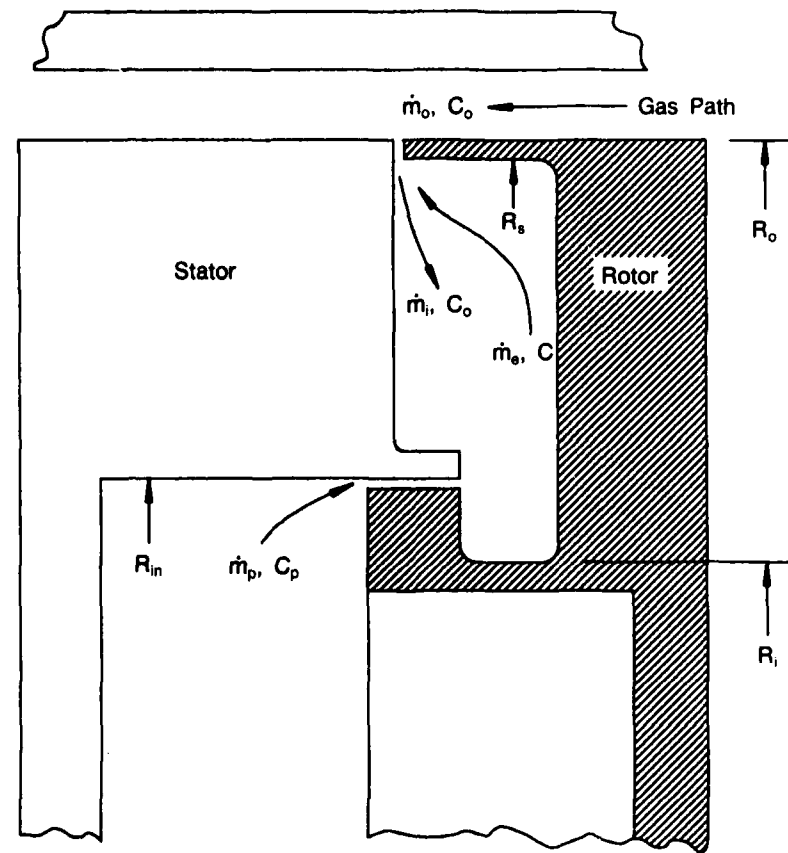


Figure 35. — Rim Seal Cooling Effectiveness Parameter for Seal Configuration 1





#### Conservation of Mass

$$\dot{m}_p - \dot{m}_e = \dot{m}_i$$

#### Conservation of CO<sub>2</sub>

$$C_p \dot{m}_p - C \dot{m}_e = C_o \dot{m}_i$$

#### Cooling Effectiveness Parameter, $\phi$

$$\phi = \frac{C - C_o}{C_p - C_o} = \left[ \frac{1}{1 - (\dot{m}_i / \dot{m}_p)} \right]$$

#### Dimensionless Flow Parameter, $n_t$

$$n_t = \left( \frac{\dot{m}_p}{4 \pi \mu R_c} \right) / Re_t^{0.8}$$

#### Parameters

$\dot{m}_p$  = Purge Flow

$\dot{m}_e$  = Ejected Flow

$\dot{m}_i$  = Ingested Flow

$\dot{m}_o$  = Gas Path Flow

$C_p$  = CO<sub>2</sub> Concentration of Purge

$C$  = Average Cavity CO<sub>2</sub> Concentration

$C_o$  = Gas Path CO<sub>2</sub> Concentration

$R_o$  = Rotor Rim Radius = 10.51 in.

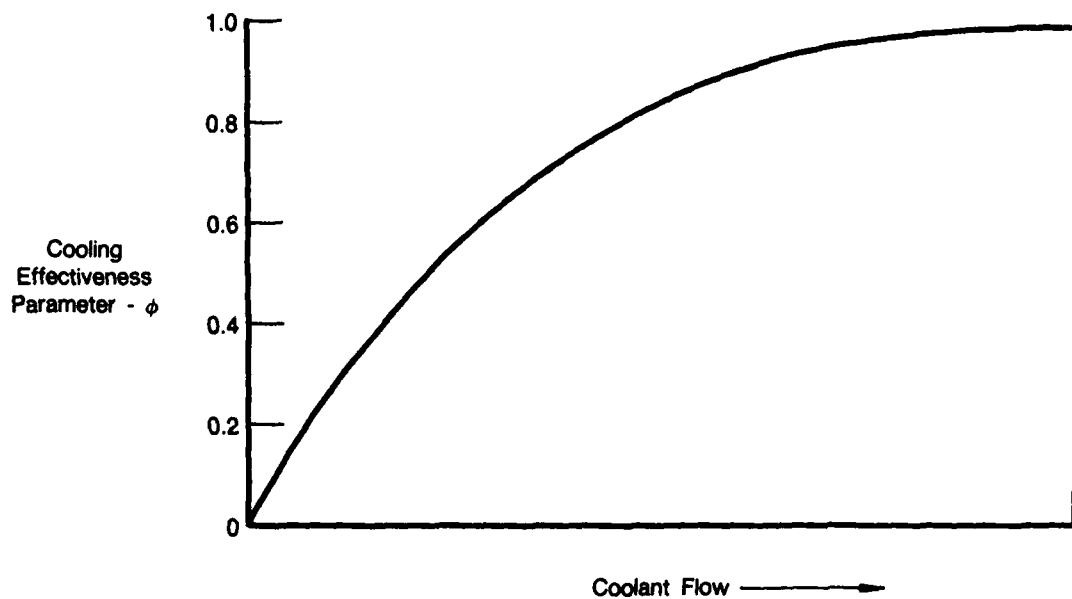
$R_s$  = Seal Radius = 10.41 in.

$R_{in}$  = Cavity Inlet Radius = 8.22 in.

$R_i$  = Cavity Inside Radius = 7.65 in.

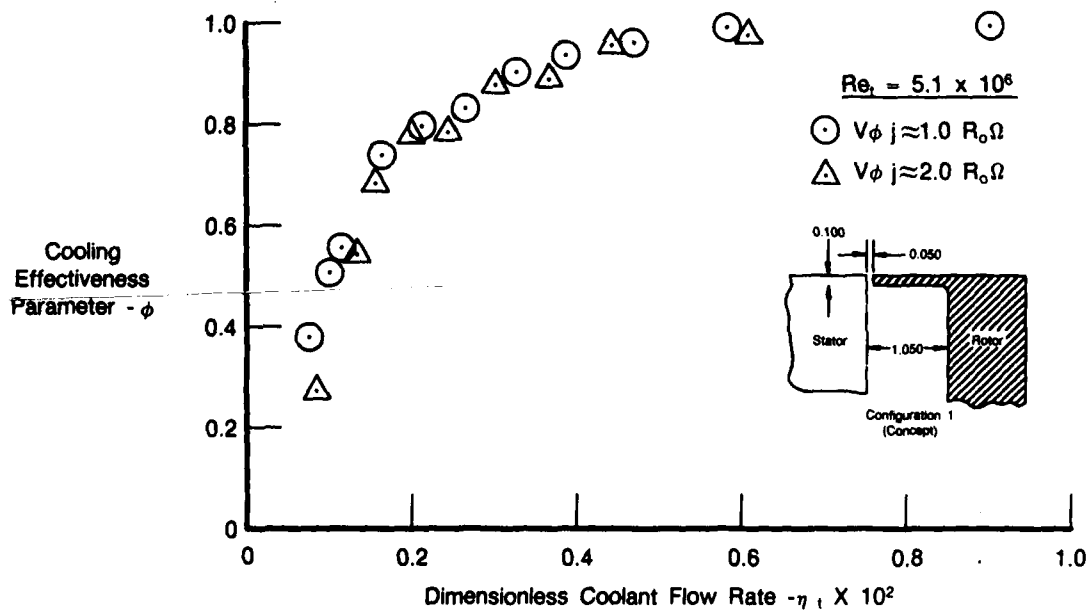
FDA 334579

Figure 33. — Definitions of Seal Cooling Effectiveness Parameter, Dimensionless Flow Parameter, and Cavity Flow and Geometric Parameters



FDA 334580

Figure 34. — Typical Seal Cooling Effectiveness Parameter as a Function of Purge Flowrate



FDA 334581

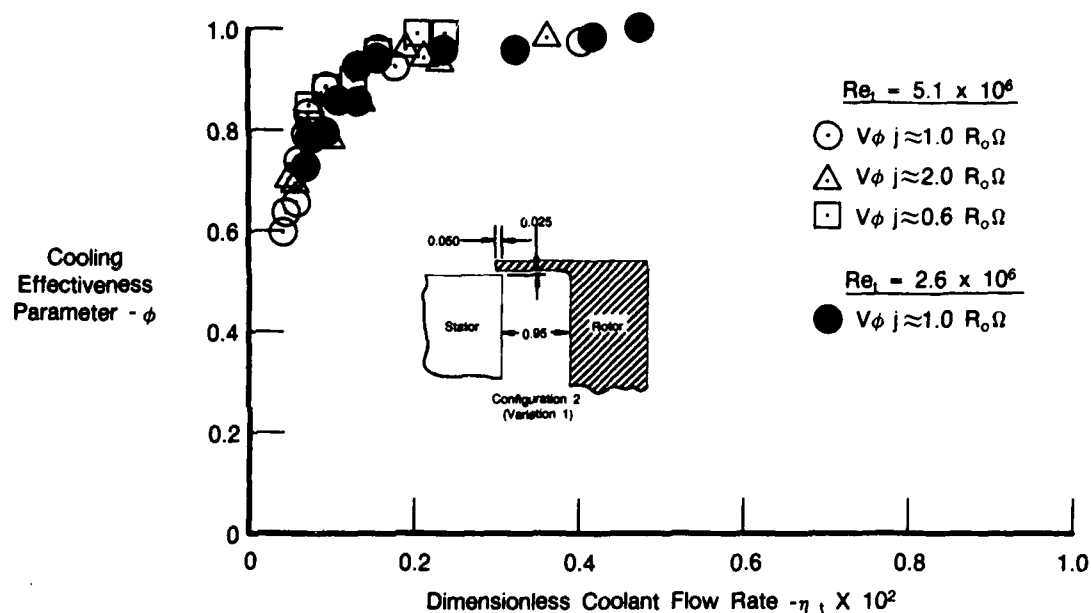
Figure 35. — Rim Seal Cooling Effectiveness Parameter for Seal Configuration 1

TABLE 2.  
TURBINE RIM SEAL TEST MATRIX

Configuration	Swirl Velocity Ratio, $V_{\phi_j}/R_o$	Tangential Reynolds No., $Re_t$	$\Omega$ rpm	$P_o$ psia
1 — Concept	1.0	$5.0 \times 10^6$	2450	62.5
	2.0	$5.0 \times 10^6$	2450	62.5
2 — Variation 1	1.0	$5.0 \times 10^6$	2450	62.5
	2.0	$5.0 \times 10^6$	2450	62.5
	0.6	$5.0 \times 10^6$	2450	62.5
	1.0	$2.5 \times 10^6$	1225	62.5
3 — Baseline	1.0	$5.0 \times 10^6$	2450	62.5
	2.0	$5.0 \times 10^6$	2450	62.5
	0.6	$5.0 \times 10^6$	2450	62.5
	1.0	$2.5 \times 10^6$	1225	62.5
4 — Variation 2	1.0	$5.0 \times 10^6$	2450	62.5
	2.0	$5.0 \times 10^6$	2450	62.5
	0.6	$5.0 \times 10^6$	2450	62.5
	1.0	$2.5 \times 10^6$	1225	62.5

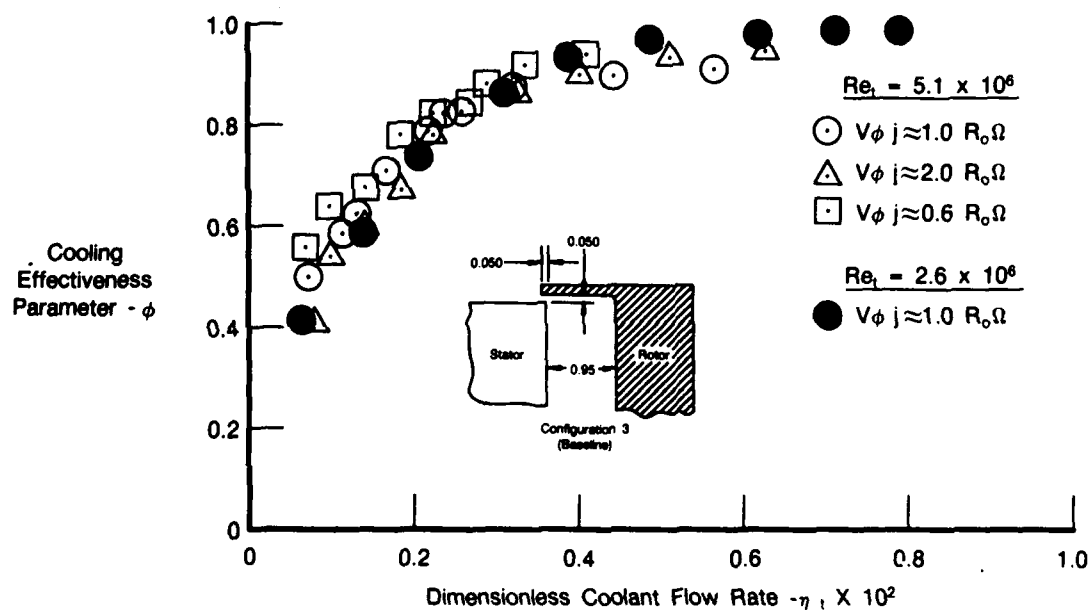
3021C

The variation of the cooling effectiveness parameter ( $\phi$ ) with dimensionless purge flowrate ( $\eta_r$ ) for rim seal Configurations 2, 3, and 4 are presented in Figures 36, 37, and 38, respectively. The lowest (i.e., the worst) cooling effectiveness parameters for a given purge flowrate were obtained with Configuration 4. Configuration 4 has a 0.050-inch radial gap and zero axial gap (no overlap). The effectiveness parameter characteristics for Configuration 4 were essentially independent of tangential Reynolds number (compare  $Re = 5.1 \times 10^6$  and  $2.6 \times 10^6$  for  $V_{\phi_j} = 1.0 \Omega R$ ) and of a decrease in  $V_{\phi_j}$  (compare  $V_{\phi_j} = 1.0$  and  $0.6\Omega R$  for  $Re_t = 5.1 \times 10^6$ ). The effectiveness parameter decreased slightly for an increase in the gaspath swirl velocity ratio.



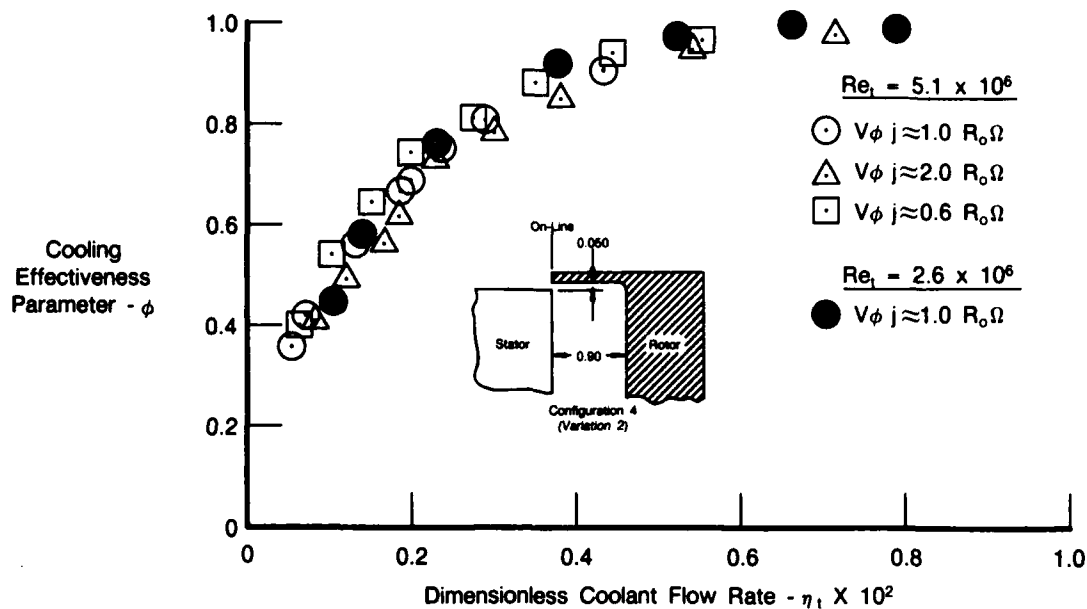
FDA 334582

Figure 36. — Rim Seal Cooling Effectiveness Parameter for Seal Configuration 2



FDA 334583

Figure 37. — Rim Seal Cooling Effectiveness Parameter for Seal Configuration 3



FDA 334584

Figure 38. — Rim Seal Cooling Effectiveness Parameter for Seal Configuration 4

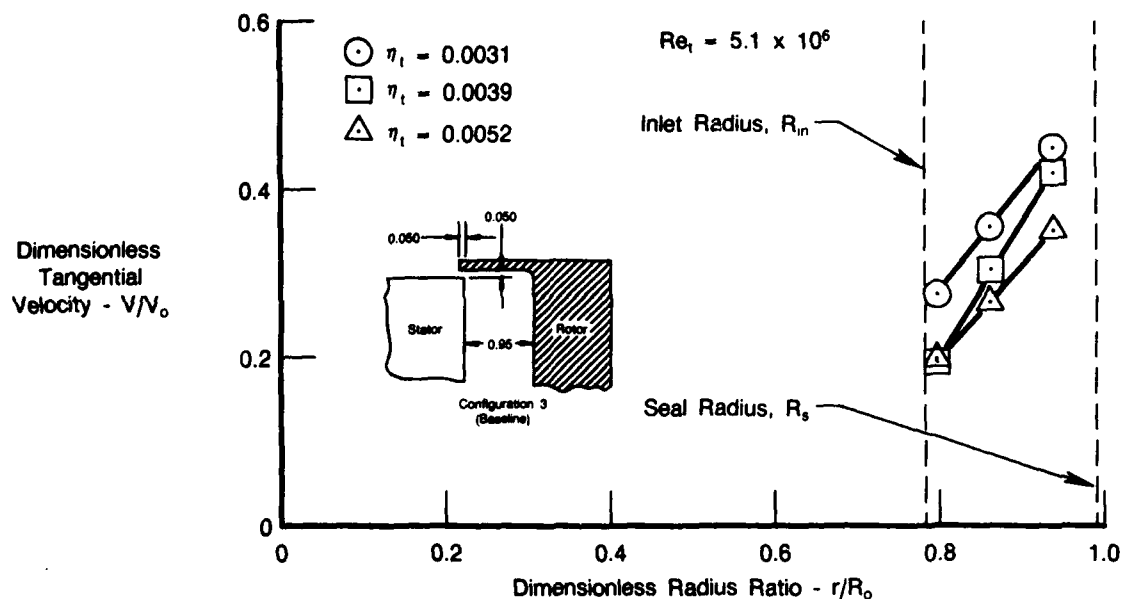
The cooling effectiveness characteristics for the baseline Configuration 3 were better (i.e., increased  $\phi$  for same value of  $\eta_1$ ) than those for Configuration 4. The effects of tangential Reynolds number and gaspath swirl ratio for Configuration 4 were mixed and were less significant than the effects of increasing the seal overlap 0.050 inch.

The cooling effectiveness characteristics for Configuration 2 were significantly better (Figure 36) than Configuration 3 or 4. Variations in the tangential Reynolds number and gaspath swirl velocity ratio did not significantly affect the characteristics of this seal.

The dimensionless tangential velocity distribution in the rim seal cavity was determined from the radial pressure distribution for Configuration 3 and for three purge flowrates, as shown in Figure 39. The tangential velocity ratios varied from 0.4 at the outer portion of the cavity to 0.2 near the inlet radius. The radial variation of tangential velocity was much greater in the rim cavity than the turbine disk cavity. This phenomena is not explained.

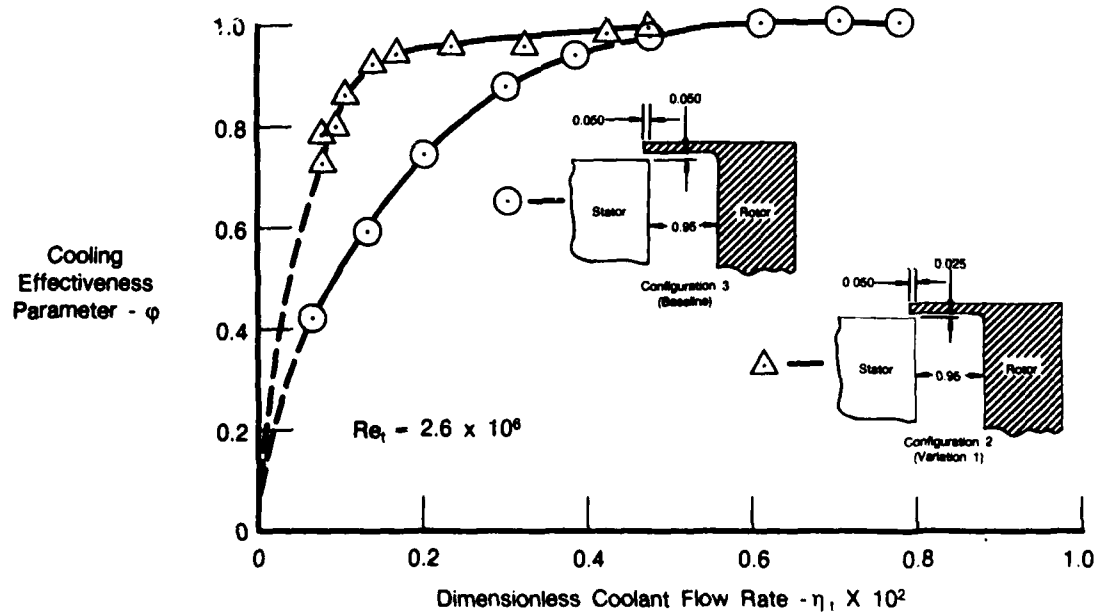
#### 1. Comparison of Rim Seal Performance

The effects of radial gap width on the cooling effectiveness parameter are shown in Figure 40 with a comparison of the results from Configuration 3 (baseline) and Configuration 2. Decreasing the radial gap to one-half (0.025 inch) of the baseline value (0.050 inch) decreased the purge flowrate required to obtain a cooling effectiveness parameter of 0.8 or 0.9 by approximately 60 percent of the baseline flowrate required to obtain the same cooling effectiveness. The cooling effectiveness for rim seals is usually most sensitive to variations in the minimum gap between the rotating and stationary components.



FDA 334585

Figure 39. — Dimensionless Tangential Velocity Profiles Obtained from the Measured Radial Pressure Distribution for Seal Configuration 3

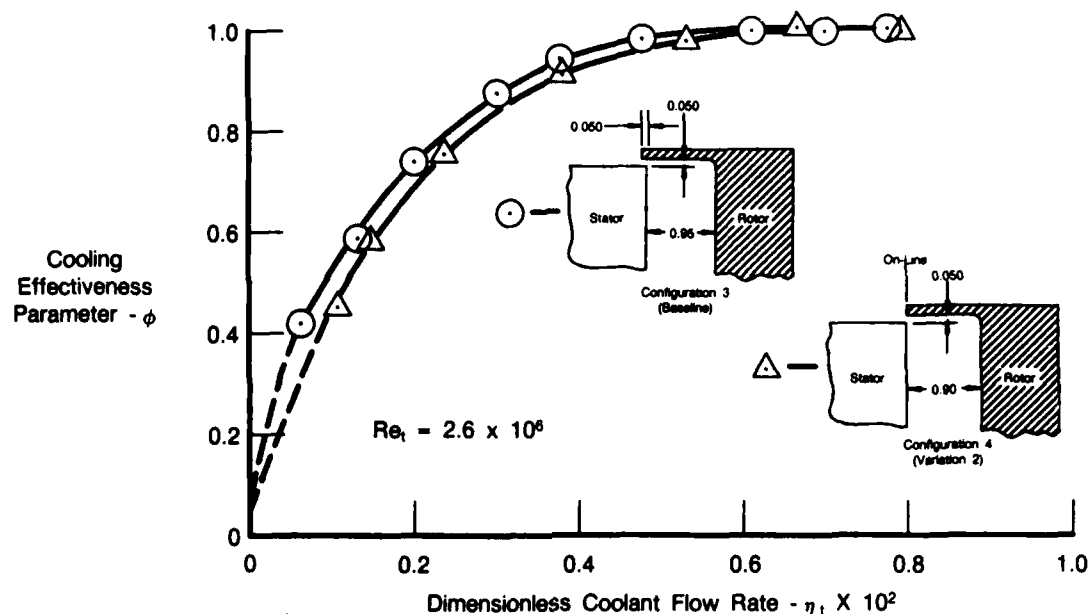


FDA 334586

Figure 40. — Effect of Radial Gap Width on the Cooling Effectiveness Parameter

The effects of increasing the axial overlap from zero to one radial gap width on the cooling effectiveness parameter is shown in Figure 41. Increasing the overlap caused the purge flow,

required to maintain a cooling effectiveness of 0.7 or 0.8, to decrease by approximately 20 percent from the baseline flowrate. Although increasing the overlap distance improved the cooling effectiveness characteristics, the effects were not as dramatic as decreasing the radial gap.



FDA 334587

Figure 41. — Effects of Axial Spacing on the Cooling Effectiveness Parameter

### 3. CORRELATION OF RESULTS

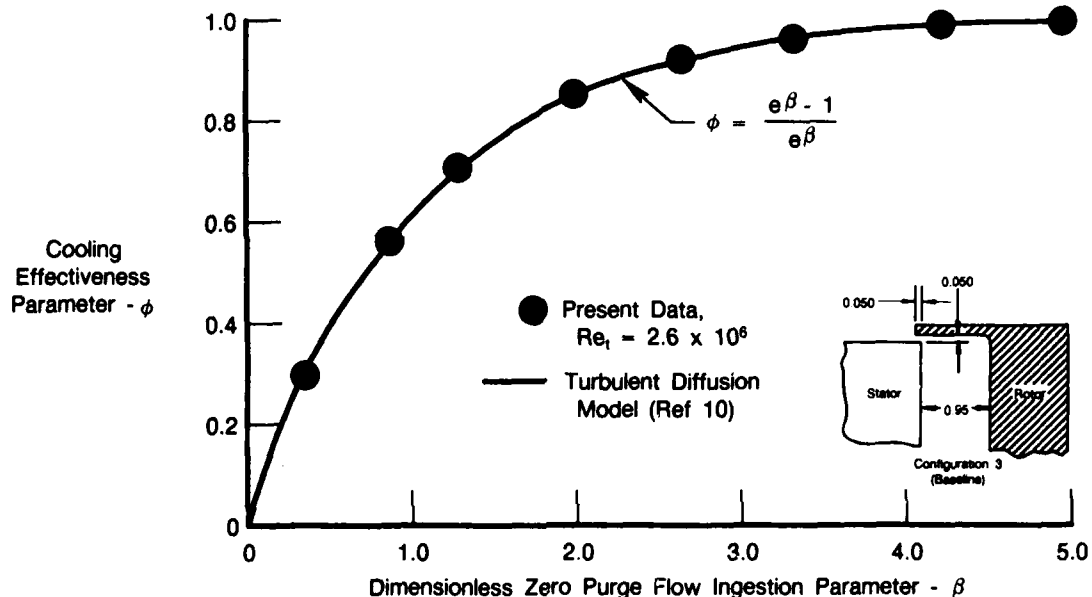
At present, the fluid mechanics of ingestion from the main gaspath into the turbine rim cavity is not well understood. For some configurations (i.e., wide clearances between the rotor and the downstream shroud) a boundary layer model has been formulated and is probably appropriate. However, as the radial clearances are reduced and the rotor rim and the vane shrouds are overlapped, a turbulent transport model for the diffusive transport of heat may be more appropriate. The results from the experiments conducted under this contract will be compared with previous correlations (References 7 and 8) and with a turbulent conductivity heat ingestion model previously developed at UTRC (Reference 10 and the Appendix A).

#### a. Comparison with Turbulent Transport Model

The rim cavity seals for most gas turbines are not designed to completely prevent ingestion into the cavity because the purge flowrate required to obtain acceptable rim seal temperatures can often be obtained at purge flowrates one-half to one-third the no ingestion amount. For example, the purge flowrate for seal Configuration 1 (Figure 35) required to obtain cooling effectiveness parameters of 0.8 and 0.9 were 27 percent and 37 percent of the flows required for no flow ingestion.

The turbulent transport model developed in Reference 10 develops a relationship which relates the purge flowrate to the cooling effectiveness parameter ( $\phi$ ). The model is empirical in that a coefficient is required for each configuration.

A set of data for seal 3 is compared with the turbulent diffusion model and presented in Figure 42. The value of the purge flow parameter equal to  $\beta = 1.0$  ( $\beta$  is defined in the Appendix) is determined by curve fitting the variation of  $\phi$  with  $\eta_t$  (Figure 36) near the value of  $\phi = 1.0 - e^{-1.0} = 0.632$ . The modeled relationship which passes the data at  $\phi = 0.632$  in Figure 42 is also an acceptable curve fit for the data at other values of  $\beta$ , i.e.  $= \eta_t/\eta'_t$  for  $\phi = 0.632$ ). The dimensional purge flowrate for  $\beta = 1.0$  is also the flowrate required to convect away the heat turbulently conducted or diffused through the seal at a zero purge flowrate (see the Appendix - Equation A-13a and related discussion). The dimensional and dimensionless purge flowrates for  $\beta = 1$  are denoted  $m'$  and  $\eta'_t$ , respectively.



FDA 334588

Figure 42. — Comparison of Present Data With Results of Turbulent Diffusion Model for Seal Configuration 3

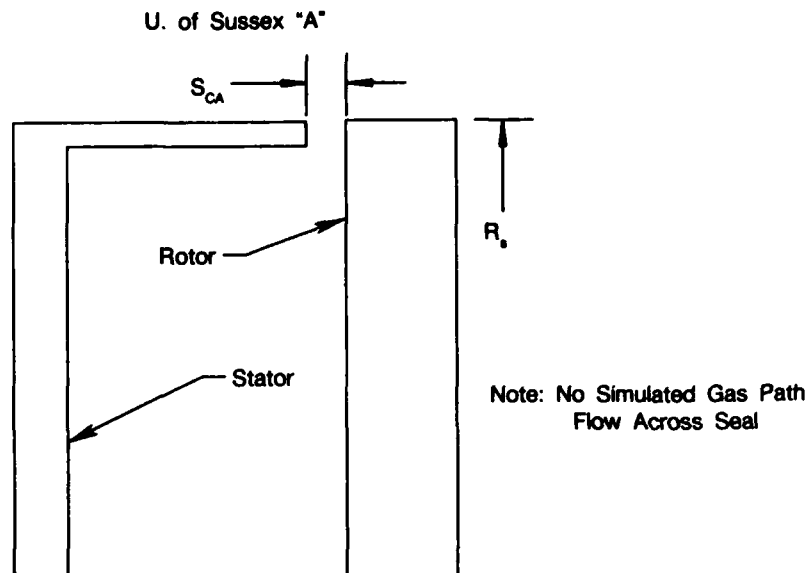
The analytical relationship for  $\phi$  ( $\beta$ ) will also be used to estimate flow condition for which essentially no ingestion occurs. A value of  $\phi = 0.99$  and a  $\beta = 4.6$  are assumed for this condition (i.e.,  $\phi = -\exp(-4.6) = 0.99$ ). These estimated values will be used to compare with previous work at the University of Sussex.

#### b. Comparison With the University of Sussex Correlations

Extensive experiments have been conducted at the University of Sussex with several rim seal configurations to determine the purge flow required to prevent ingestion. A combination of flow visualization and pressure measurements were used to estimate the amount of flow required to prevent ingestion for a given seal and disk rotation rate. Their experiments were conducted over a Reynolds number range from  $10^5$  to  $10^6$ .

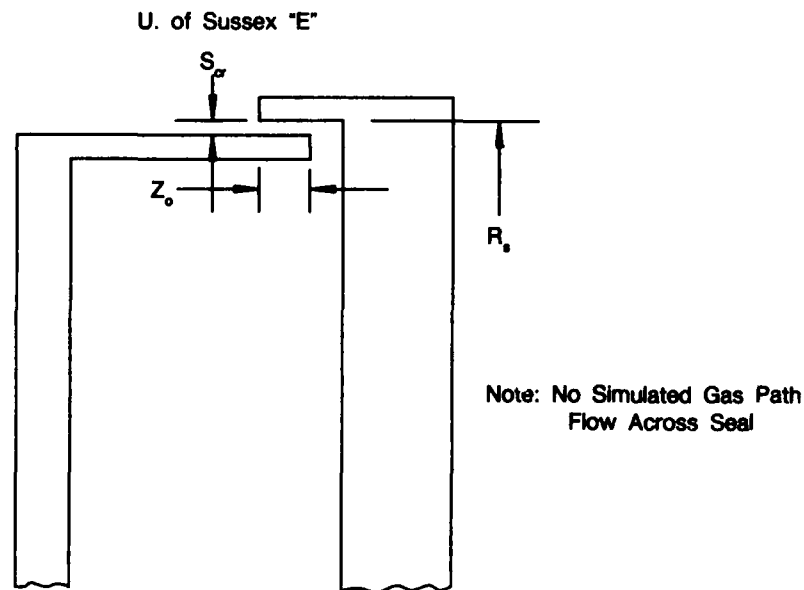
Several seal configurations were investigated at the University of Sussex and reported in References 7 and 8. Two configurations are shown in Figures 43 and 44 along with the definition for the seal gaps.





FDA 334589

Figure 43. — Definition of the Dimensionless Seal Gap Parameter,  $S_{CA}/R_s$ , Used in References 7 and 8



FDA 334590

Figure 44. — Definition of the Dimensionless Seal Gap Parameter,  $S_{cr}/R_s$ , Used in References 7 and 8

The results from this report and those from References 7 and 8 will be compared on the basis of a purge velocity ratio. The purge velocity ratio is defined as  $V_p/V_\phi$  where  $V_p$  is the radial axial average velocity through the minimum gap area,  $V_p = m/(2\pi R_s s)$ , and  $V_\phi$  is the tangential velocity of the rim seal. The purge flow required to prevent ingestion was obtained from

Reference 8 for seals A and E and for two ratios of  $s/R$ , 0.0025 and 0.0050. The purge velocity ratio was calculated from the Reference 8 tabulated results and the seal gap/radius ratio.

The no ingestion condition was estimated from the present report to occur when the cooling effectiveness ratio was 0.99. Because most of the data was obtained for cooling effectiveness ratio between 0.4 and 0.95, the  $\phi = 0.99$  value was estimated using the rim seal turbulent diffusion model as described in the previous subsection. The velocity ratio information from the present report is presented in Table 3.

TABLE 3.  
DIMENSIONAL AND DIMENSIONLESS PARAMETERS FOR TURBINE RIM SEAL  
INGESTION EXPERIMENTS

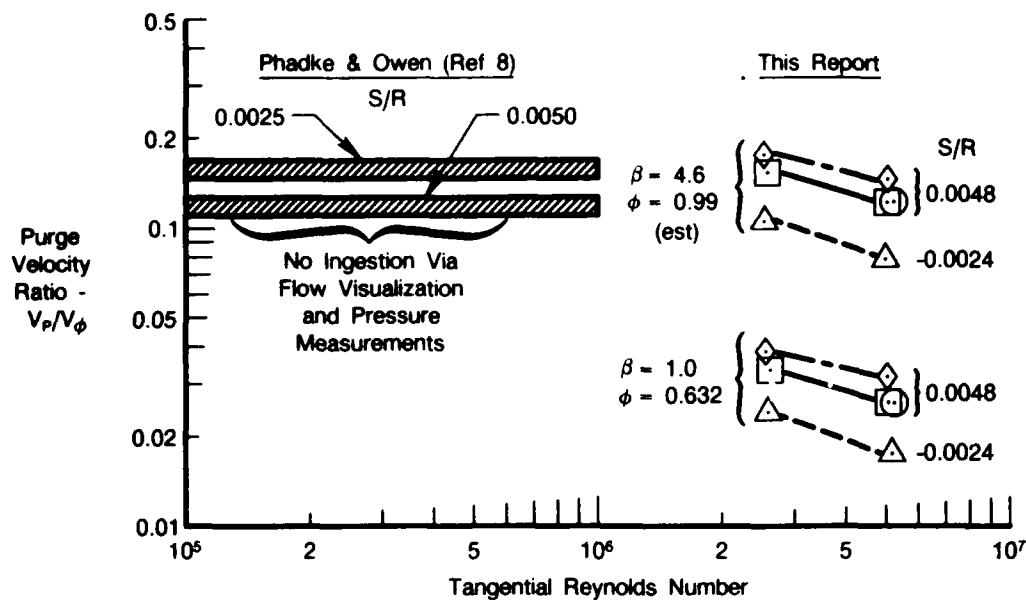
Configuration	$S/R$	Swirl Velocity Ratio, $V_{\phi}/R_o$	Tangential Reynolds No., $Re_t$	$\dot{m}$ lb/sec	$\eta'_t = \frac{Re_t'}{Re_t 0.8}$	$V_r'/V\phi$	$4.6 V_r'/V\phi$
1 — Concept	0.0048	1.0	$5.0 \times 10^6$	0.0438	0.00138	0.026	0.120
	0.0048	2.0	$5.0 \times 10^6$	0.0444	0.00140	0.027	0.124
2 — Variation 1	0.0024	1.0	$5.1 \times 10^6$	0.0143	0.00045	0.017	0.070
	0.0024	2.0	$5.1 \times 10^6$	—	—	—	—
	0.0024	0.6	$5.1 \times 10^6$	—	—	—	—
	0.0024	1.0	$2.6 \times 10^6$	0.0102	0.00055	0.024	0.110
3 — Baseline	0.0048	1.0	$5.1 \times 10^6$	0.0428	0.00135	0.026	0.120
	0.0048	2.0	$5.1 \times 10^6$	0.0491	0.00155	0.029	0.133
	0.0048	0.6	$5.1 \times 10^6$	0.0285	0.00090	0.017	0.078
	0.0048	1.0	$2.6 \times 10^6$	0.0277	0.00150	0.033	0.152
4 — Variation 4	0.0048	1.0	$5.1 \times 10^6$	0.0539	0.00170	0.032	0.147
	0.0048	2.0	$5.1 \times 10^6$	0.0618	0.00195	0.037	0.170
	0.0048	0.6	$5.1 \times 10^6$	0.0482	0.00152	0.029	0.133
	0.0048	1.0	$2.6 \times 10^6$	0.0324	0.00175	0.038	0.174

Notes:  $\eta'_t$  obtained from Figures 35 through 38

$\eta'_t = \eta_t$  at  $\phi = 0.632$  for each test series

3921C

A comparison of the purge velocity ratios required to prevent ingestion is presented in Figure 45. The results from Reference 8 are presented as a data band between correlations for Configurations A and E. Note that the average purge velocity ratio for the value of  $s/R = 0.0025$  is approximately 30 percent greater than for the value of  $s/R = 0.0050$ . The results from this report are shown for  $\beta = 1.0$  and  $\phi = 0.632$  as measured and for  $\beta = 4.6$  and  $\phi = 0.99$  as estimated. The data from this report indicate the purge velocity ratio for the value of  $s/R = 0.0048$  is approximately 50 percent greater than the value for  $s/R = 0.0024$ . This relationship is reversed from that obtained in the University of Sussex experiments. The other marked difference between the results from this report and those from References 7 and 8 is that the purge velocity ratios from this report decrease with increasing tangential Reynolds number. Flow visualization results from Reference 8 for some seals also showed a decrease in the purge velocity ratio as the Reynolds number was increased to  $10^6$ . However, the correlations deduced in Reference 8 from the combination of pressure measurements and flow visualization did not show this trend. Additional experiments will be required to resolve the aforementioned differences. Considering the differences in measurement techniques and the assumptions required for the comparison, the agreement between the results from this report and those from References 7 and 8 are good.



FDA 334591

Figure 45. — Comparison of Purge Velocity Ratio Results With Reference 8

## SECTION V

### COMPRESSOR DRUM AERODYNAMIC EXPERIMENTS

#### 1. INTRODUCTION

##### a. Problem

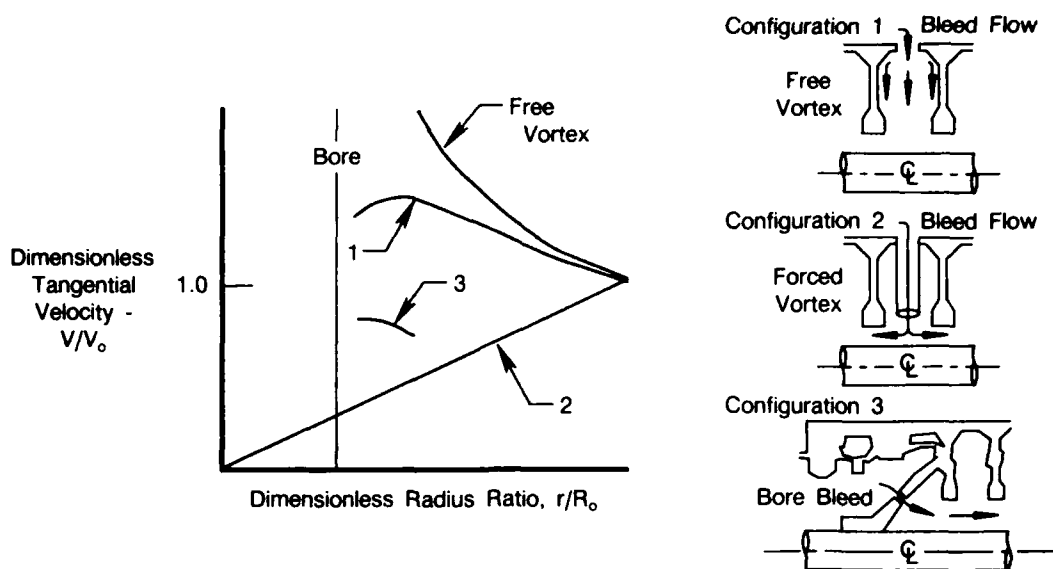
The flows inside compressor drum assemblies can be represented by a system of co-rotating disk cavities which rotate at the same angular velocity. Unlike rotor-stator disk systems where the relative velocity between disks provides a means by which work can be input into the system, the only momentum input into the compressor drum flow system is due to the initial swirl of the coolant injected into the drum. As a result, the flow fields in the compressor drum are dominated by the conservation of the initial angular momentum of the coolant bled into the system. These flows are characteristically weak and the decay of the heat transfer driving swirl can be significant and can be reduced until the cavity flows are primarily buoyancy driven. A comprehensive understanding of the enclosed rotating swirl flows in the compressor drum is required to predict disk heat transfer and thermal response characteristics. These flows will be largely dependent upon the coolant flowrate and coolant injection location.

Three typical compressor drum bleed configurations are shown in Figure 46. The disk cavity flow characteristics and disk heat transfer mechanisms in both the bleed and non-bleed cavities will differ significantly for each of these bleed configurations. For bleed Configuration 1, coolant enters the drum through the rim at a mid-compressor stage with the same angular rotation rate as the drum. Conservation of angular momentum for this situation requires that the angular rotation rate of the fluid increase with decreasing radius. This is shown in Figure 46 as Curve 1 in a plot of the tangential velocity of the fluid in the cavity (normalized by its initial value) versus the dimensionless radius ratio. For this bleed situation, Curve 1 indicates that the fluid in the bleed cavity rotates at a rate that is greater than that of the disks. Thus, a relative velocity exists between the fluid and the disks and a convective heat transfer process is possible for this bleed configuration. This heat transfer driving swirl, however, can be expected to decay in the enclosed cavities adjacent to the bleed cavity.

For bleed Configuration 2, coolant enters the drum from the same location as 1 but is constrained by a tube to move with the same angular velocity as the disk. The tangential velocity profile for this situation is shown in Figure 46 as Curve 2. For this case, there is no relative velocity between the fluid and the disk. A heat transfer process which is predominately buoyancy driven is possible here. For bleed Configuration 3, fluid enters the drum from the fan through the front endwall of the drum at a radius that is close in magnitude to the compressor drum disk bore. Conservation of angular momentum for this case requires that the angular velocity of the fluid decrease with increasing radius in the cavity. Curve 3 for this bleed configuration shows a tangential velocity profile which is somewhere in between that of bleed 1 and bleed 2. This indicates that a moderate amount of swirl is present and that a heat transfer process for this situation can be both convective and buoyancy driven in nature.

##### b. Objective

The objectives of this investigation were to document and correlate compressor drum disk cavity flow characteristics in both bleed and nonbleed cavities with changes in coolant injection location and coolant flowrate.



FDA 334592

Figure 46. — Typical Effect of Bleed Configuration on Tangential Velocity Distribution in Compressor Drum

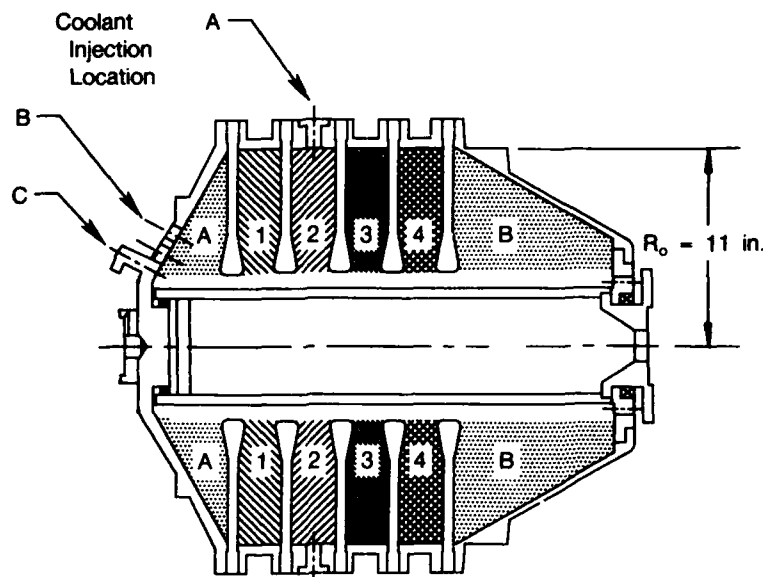
### c. Approach

To achieve these objectives, an experimental investigation was conducted to obtain compressor drum disk cavity aerodynamic data for a number of bleed configurations and coolant flow conditions. Pressure measurements at selected disk radii were obtained in a six-cavity compressor drum model in both bleed and non-bleed cavities. Three bleed configurations were investigated. One configuration simulated a high-pressure compressor midstage bleed configuration and the other two bleed configurations simulated two fan bled compressor drum designs with bore bleeds (Configuration 3, Figure 46). All measurements were obtained at Reynolds numbers typical of current and advanced gas turbine engines using air as the working fluid.

## 2. DISCUSSION OF EXPERIMENTS AND RESULTS

### a. Test Procedure

The experiments were conducted at UTRC using the compressor drum test assembly described in Section II. The three bleed configurations investigated are shown in Figure 47 and are identified by coolant injection locations A, B, and C. For bleed configuration A, coolant was injected at the drum rim of cavity 2 at a radius of 11.0 inches through 8 equally spaced radial holes. For B and C, coolant was injected through the 120 degree conical endwall of the drum at radii of 6 inches and 4 inches respectively. Each injection radius contained 8 equally spaced bleed holes. The radius of injection for Configuration C was the same as that of the disk bores, 4 inches.



FDA 334593

Figure 47. — Compressor Drum Model With Cavity Nomenclature

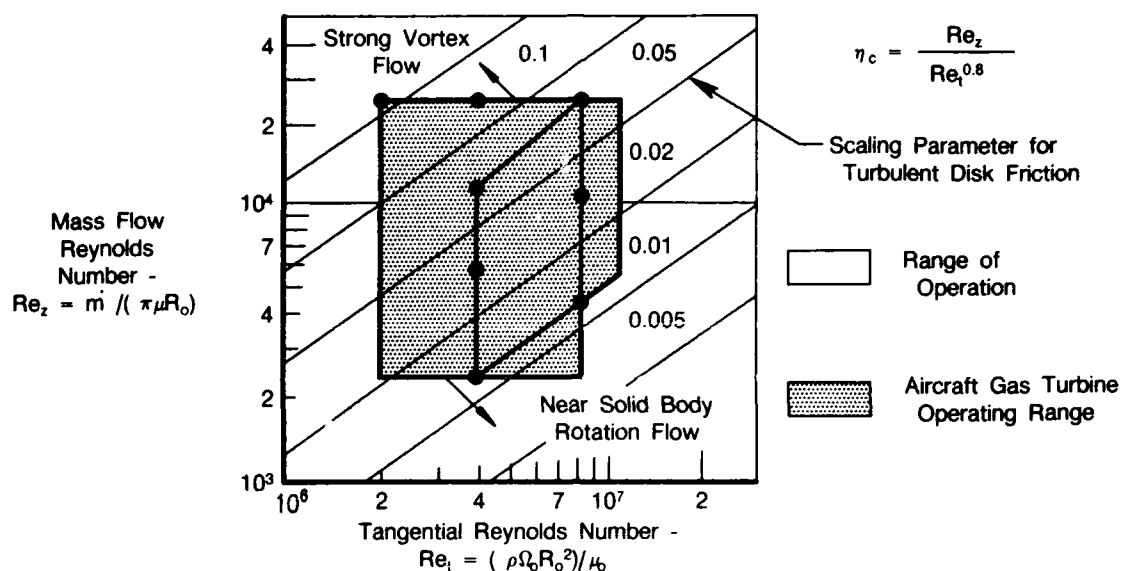
The compressor drum test matrix and operating range is shown in Figure 48. The coordinates chosen here are the tangential Reynolds number ( $Re_t$ ) and the dimensionless mass flow Reynolds number ( $Re_z$ ). The mass flow Reynolds number is defined as:

$$Re_z = \dot{m}/(\pi\mu R_o) \quad (7)$$

where:

- $\dot{m}$  = coolant flowrate
- $\mu$  = viscosity of the fluid
- $R_o$  = the disk rim radius.

These parameters were chosen because they can be used to form a quantity called the dimensionless flow parameter ( $\eta_c$ ) which will be shown to be able to correlate the disk cavity radial pressure drop with flow conditions. Lines of constant  $\eta_c$  are shown in Figure 48 superimposed upon the test matrix. Note in Figure 48, that the test matrix covers a large portion of the operating range of current and advanced gas turbine engines. Specific data point information for bleed configurations A, B, and C are given in Tables 4 through 6.



FDA 334594

Figure 48. — Operating Range for Compressor Drum Model

TABLE 4.

TEST CONDITIONS AND DIMENSIONLESS PARAMETERS FOR COMPRESSOR DRUM COLD FLOW EXPERIMENTS WITH COOLANT INJECTION LOCATION A

Test	Dimensionless Parameters						Dimensional Parameters								
	$Re_t$ ( $10^{-6}$ )	$Re_z$	$\frac{Re_z}{Re_{0.8}}$	$\frac{\Omega_o}{\Omega_i}$	$\frac{T_w - T_c}{T_w}$	$\frac{V_j}{\Omega r_j}$	$\Omega_o$ rpm	$\Omega_i$ rpm	P psia	$\dot{m}$ lb/sec	$T_w$ °F	$T_c$ °F	$\rho_c$ lb/ft <sup>3</sup>	$V_j$ ft/sec	$\Omega r_j$ ft/sec
A1	7.6	13,975	0.043	1.0	0	0.205	1500	1500	136	0.495	78	78	0.682	29.6	144.0
A2	7.3	5,007	0.016	1.0	0	0.075	1500	1500	138	0.180	88	88	0.680	10.8	144.0
A3	8.1	21,060	0.063	1.0	0	0.297	1500	1500	139	0.740	72	72	0.705	42.8	144.0
A4	4.3	6,621	0.033	1.0	0	0.176	2000	2000	56	0.234	76	76	0.282	33.8	192.0
A5	4.0	3,066	0.016	1.0	0	0.085	2000	2000	56	0.110	87	87	0.276	16.2	192.0
A6	4.7	13,331	0.061	1.0	0	0.338	2000	2000	57	0.465	67	67	0.292	64.9	192.0
A7	4.7	17,788	0.082	1.0	0	0.467	2000	2000	55	0.620	67	67	0.282	89.6	192.0
A8	4.7	21,863	0.099	1.0	0	0.581	2000	2000	55	0.766	70	70	0.280	111.5	192.0
A9	2.2	22,696	0.188	1.0	0	1.178	1000	1000	56	0.794	69	69	0.286	113.1	96.0
A10	4.4	8,246	0.040	1.0	0	0.217	2000	2000	56	0.290	73	73	0.284	41.68	192.0

Injection Through (8) 0.75 in.-dia holes (0.0245 ft<sup>2</sup>)

3921C

TABLE 5.

**TEST CONDITIONS AND DIMENSIONLESS PARAMETERS FOR COMPRESSOR  
DRUM FLOW EXPERIMENTS WITH COOLANT INJECTION LOCATION B**

Test	Dimensionless Parameters						Dimensional Parameters								
	$Re_t$ ( $10^{-6}$ )	$Re_z$	$\frac{Re_z}{Re_t 0.8}$	$\frac{\Omega_o}{\Omega_i}$	$\frac{T_w - T_c}{T_w}$	$\frac{V_j}{\Omega r_j}$	$\Omega_o$ rpm	$\Omega_i$ rpm	P psia	$\dot{m}$ lb/sec	$T_w$ °F	$T_c$ °F	$\rho_c$ lb/ft <sup>3</sup>	$V_j$ ft/sec	$\Omega r_j$ ft/sec
B1	7.5	13,252	0.042	1.0	0	0.350	1500	1500	137	0.467	74	74	0.693	27.5	78.5
B2	7.4	5,675	0.018	1.0	0	0.151	1500	1500	136	0.200	74	74	0.688	11.9	78.5
B3	7.3	21,283	0.069	1.0	0	0.579	1500	1500	137	0.759	82	82	0.682	45.4	78.5
B4	7.1	11,263	0.037	1.0	0	0.312	1500	1500	137	0.405	88	88	0.675	24.5	78.5
B5	4.0	6,136	0.032	1.0	0	0.299	2000	2000	58	0.220	86	86	0.287	31.3	104.7
B6	3.9	3,146	0.017	1.0	0	0.160	2000	2000	57	0.114	94	94	0.278	16.7	104.7
B7	4.1	13,952	0.072	1.0	0	0.683	2000	2000	56	0.494	77	77	0.282	71.5	104.7
B8	4.1	19,584	0.100	1.0	0	0.961	2000	2000	55	0.688	72	72	0.279	100.6	104.7
B9	2.0	10,315	0.094	1.0	0	1.020	1000	1000	55	0.364	75	75	0.278	53.4	52.4
B26	6.3	5,505	0.020	2.5	0	0.173	1500	600	132	0.206	117	117	0.618	13.6	78.5
B27	6.8	19,468	0.067	2.5	0	0.571	1500	600	134	0.711	99	99	0.647	44.9	78.5
B28	5.1	3,398	0.015	2.5	0	0.132	1500	600	107	0.127	116	116	0.501	10.3	78.5
B29	5.3	12,476	0.052	2.5	0	0.464	1500	600	106	0.456	100	100	0.511	36.4	78.5
B30	6.3	5,476	0.020	-2.5	0	0.172	1500	-600	132	0.205	117	117	0.618	13.5	78.5
B31	6.8	19,292	0.066	-2.5	0	0.567	1500	-600	134	0.705	100	100	0.646	44.5	78.5
B32	5.2	3,502	0.015	-2.5	0	0.134	1500	-600	107	0.130	111	111	0.506	10.5	78.5
B33	5.4	12,463	0.052	-2.5	0	0.462	1500	-600	106	0.455	99	99	0.512	36.3	78.5

Injection Through (8) 0.75 in.-dia holes (0.0245 ft<sup>2</sup>)

3921C

TABLE 6.

**TEST CONDITIONS AND DIMENSIONLESS PARAMETERS FOR COMPRESSOR  
DRUM FLOW EXPERIMENTS WITH COOLANT INJECTION LOCATION C**

Test	Dimensionless Parameters						Dimensional Parameters								
	$Re_t$ ( $10^{-6}$ )	$Re_z$	$\frac{Re_z}{Re_t 0.8}$	$\frac{\Omega_o}{\Omega_i}$	$\frac{T_w - T_c}{T_w}$	$\frac{V_j}{\Omega r_j}$	$\Omega_o$ rpm	$\Omega_i$ rpm	P psia	$\dot{m}$ lb/sec	$T_w$ °F	$T_c$ °F	$\rho_c$ lb/ft <sup>3</sup>	$V_j$ ft/sec	$\Omega r_j$ ft/sec
C1	7.4	10,481	0.033	1.0	0	0.432	1500	1500	135	0.369	89	89	0.664	22.6	52.4
C2	7.3	6,227	0.020	1.0	0	0.252	1500	1500	136	0.221	79	79	0.681	13.2	52.4
C3	7.2	19,341	0.063	1.0	0	0.790	1500	1500	135	0.687	79	79	0.676	41.4	52.4
C4	3.9	5,760	0.031	1.0	0	0.437	2000	2000	55	0.206	84	84	0.275	30.5	69.8
C5	3.9	3,732	0.020	1.0	0	0.283	2000	2000	56	0.134	87	87	0.276	19.8	69.8
C6	3.8	12,973	0.070	1.0	0	0.990	2000	2000	53	0.456	72	72	0.269	69.1	69.8
C7	4.1	18,983	0.098	1.0	0	1.386	2000	2000	55	0.665	70	70	0.280	96.8	69.8
C8	4.1	20,225	0.105	1.0	0	1.476	2000	2000	55	0.708	70	70	0.280	103.0	69.8
C9	2.0	17,541	0.159	1.0	0	2.613	1000	1000	55	0.620	76	76	0.277	91.2	34.9

Injection Through (8) 0.75 in.-dia holes (0.0245 ft<sup>2</sup>)

3921C

The pressure measurements were made in the rotating frame of reference using a 48-port Model 48J4-1 Scanivalve assembly using a  $\pm 25$ -psid scanivalve pressure transducer. Calibration of the pressure transducer with a dead weight tester before and after the investigation showed the transducer to be repeatable and accurate to within  $\pm 0.04$  psi.



The procedure for determining the velocity profiles shown in Figure 49 was to curve fit the measured pressure data to a polynomial from which the slope was obtained. The tangential velocity was then calculated by:

$$V = \sqrt{(r/\rho) (dp/dr)} \quad (8)$$

where:

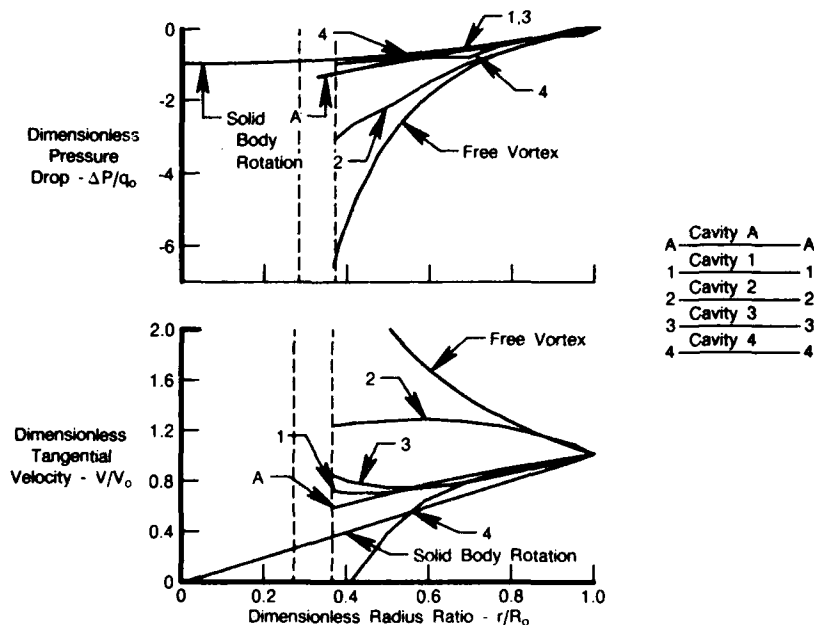
$r$  = local radius

$dp/dr$  = pressure gradient obtained from the curve fit

$\rho$  = density of the fluid at the test conditions.

#### b. Results for Bleed Configuration A

Disk radial pressure measurements were obtained for the A bleed configuration at the flowrates and tangential Reynolds numbers shown in Table 4. The results for the baseline test point A10 are shown in Figure 49. Here, the dimensionless pressure drops and the tangential velocity profiles for drum cavities A through 4 are shown versus the dimensionless radius ratio. Note the relatively large pressure drop in the bleed cavity as compared to those obtained in the adjacent cavities. Also, this large pressure drop corresponds to a relatively large tangential velocity profile within the cavity.



FDA 334595

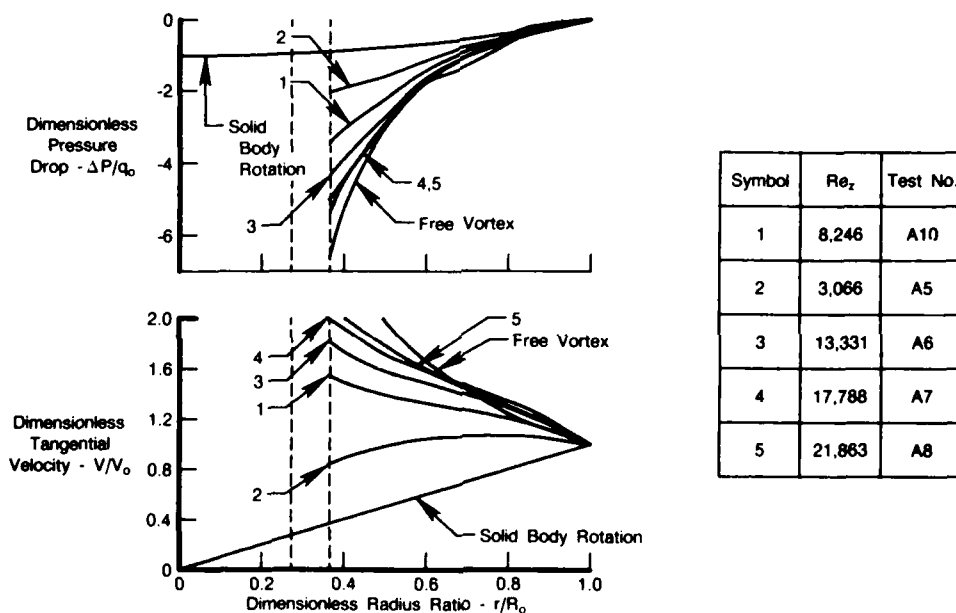
Figure 49. — Pressure and Tangential Velocity Distributions in Selected Cavities of Compressor Drum With Baseline Flow Conditions and Coolant Injection Location A, Test Point A10

For comparison, the pressure drop and the tangential velocity profile for a free vortex and a solid body rotation is shown in Figure 49 in addition to the data. Compared with these curves, the data indicate a swirl level in the bleed cavity that appears to approach the free vortex level over a large portion of the cavity. The pressure drop and velocity profiles for the adjacent cavities indicate a decay of this swirl level to values which approach that of a solid body rotation.

The tangential velocity profiles obtained in this study agree quite favorably with those obtained by Bennett, (Reference 9) who made Laser-Doppler measurements of the flow field in an 11-cavity compressor drum model having the same bleed configuration. In Reference 9, water was used as the working fluid.

The velocity calculated with equation 8 is especially sensitive to small changes to the slope of the fitted curve where the tangential velocities are low. This condition occurs near the bore of the compressor disk when the tangential velocities are near solid body rotation. The tangential velocity determined for the flow in cavity 4 for  $r/R_o < 0.5$  (Reference Figures 49, 51, and 53) may be adversely influenced by the polynomial curve fit through one pressure tap. The velocities determined for the other cavities appear reasonable and self consistent at all radial locations.

Bleed cavity pressure drop and tangential velocity profiles for five flow conditions are shown in Figure 50. As the flowrate is increased, the pressure drop and tangential velocity profiles in the bleed cavity approaches that of a free vortex. The result of this observation is that increasing the flowrate increases the swirl level in the bleed cavity.

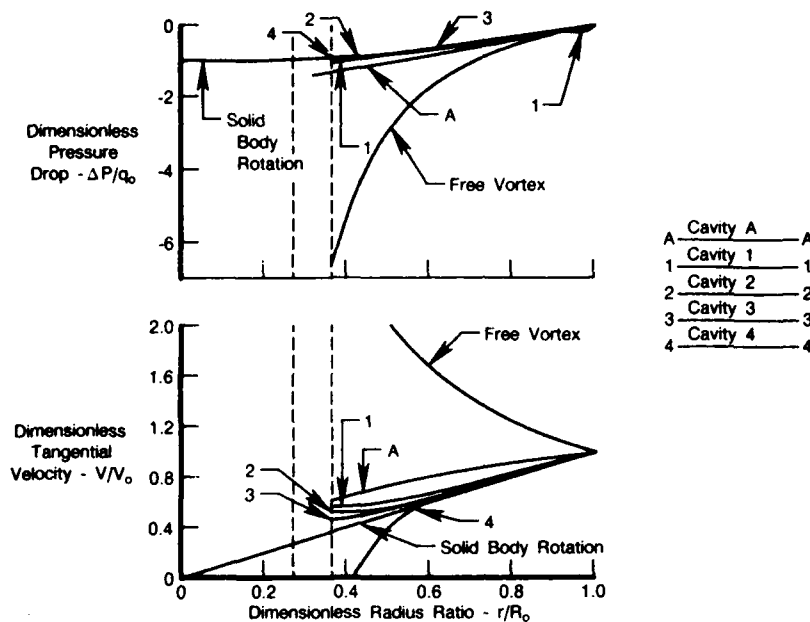


FDA 334596

Figure 50. — Effects of Coolant Flowrate on Pressure and Tangential Velocity Distributions in Bleed Cavity for Coolant Injection Location A

### c. Results for Bleed Configuration B

The radial pressure distribution and dimensionless tangential velocity profiles for the baseline test point B5 (Table 5) is shown in Figure 51. The results shown here indicate that the largest pressure drop (highest swirl level) occurs in the bleed cavity and that the pressure drop progressively decreases in the cavities adjacent to the bleed cavity. Note that the results shown in Figure 51 indicate a modest pressure drop in bleed cavity A, and that the pressure drop in the adjacent cavities is more like that of a solid body rotation.



FDA 334597

Figure 51. — Pressure and Tangential Velocity Distributions in Selected Cavities of Compressor Drum With Baseline Flow Conditions and Coolant Injection Location B, Test Point B5

The bleed cavity pressure drop and dimensionless tangential velocity profiles for three flow conditions are shown in Figure 52. The results shown here indicate an increasing pressure drop with increasing flowrate for radius ratios up to approximately 0.5 and near solid body rotation type pressure drops for larger values of radius ratio. The tangential velocity profiles display a similar trend. This behavior may be due in part to the shape of Cavity A. Note also the vortex-like behavior of the velocity profile at  $0.35 < r/R_o < 0.7$  for the high flowrate condition. This phenomenon will be examined more closely below.

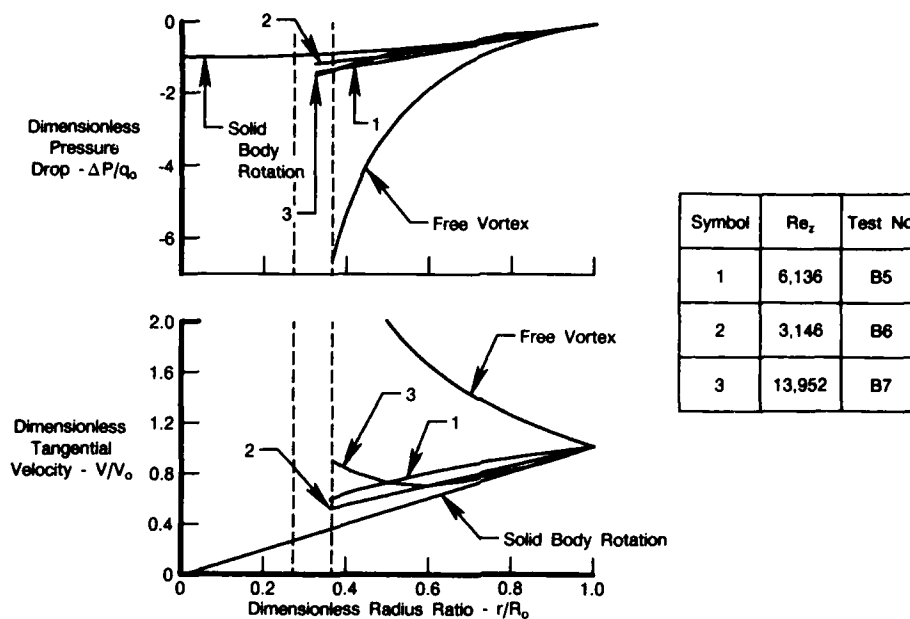
#### d. Results for Bleed Configuration C

Dimensionless pressure drop and tangential velocity profiles for bleed Configuration C are shown in Figure 53. The results shown are for the baseline test point C4 (Table 6). Results shown in Figure 53 indicate a solid body rotation type of behavior in all of the cavities. The pressure drop and tangential velocity profiles obtained at other test points were found to produce results similar to those shown in Figure 53. The conclusion from these experiments is that the cavity aerodynamic characteristics for bleed Configuration C are relatively independent of flowrate.

#### e. Comparison of Results for Bleeds A, B, and C

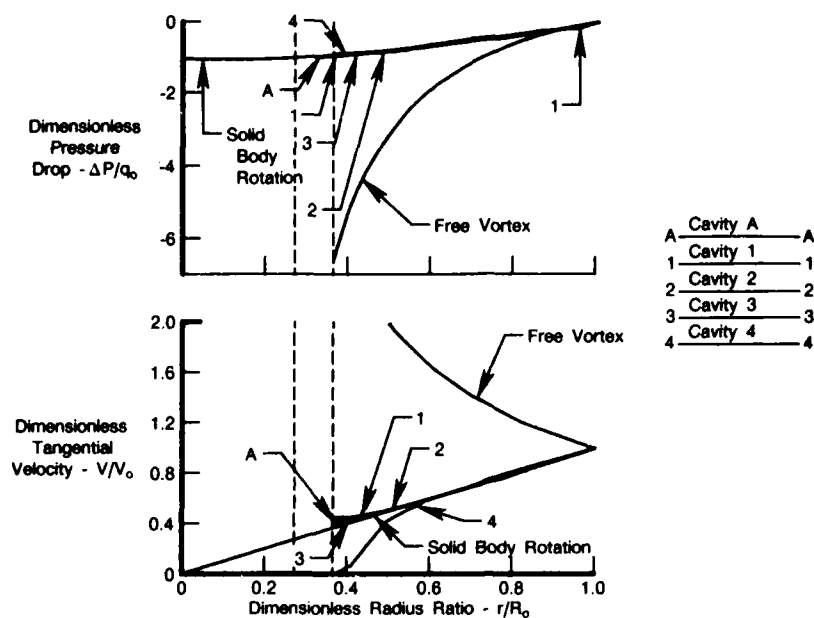
A comparison of the pressure drop and the tangential velocity profiles obtained in the bleed cavities for Configurations A, B, and C are shown in Figures 54 and 55. The results for each bleed configuration were obtained at the same flow conditions. The most significant observation from these figures is the effect that the coolant injection radius has on the compressor drum flow patterns. The results indicate that the pressure drop and cavity swirl levels obtained for

Configuration A are greater than those obtained for bleed Configurations B and C. The conclusion from of this observation is that the midstage compressor bleed configuration has a greater capacity for driving the flow inside the compressor drum cavity, compared with the fan bleed designs represented by bleeds B and C.



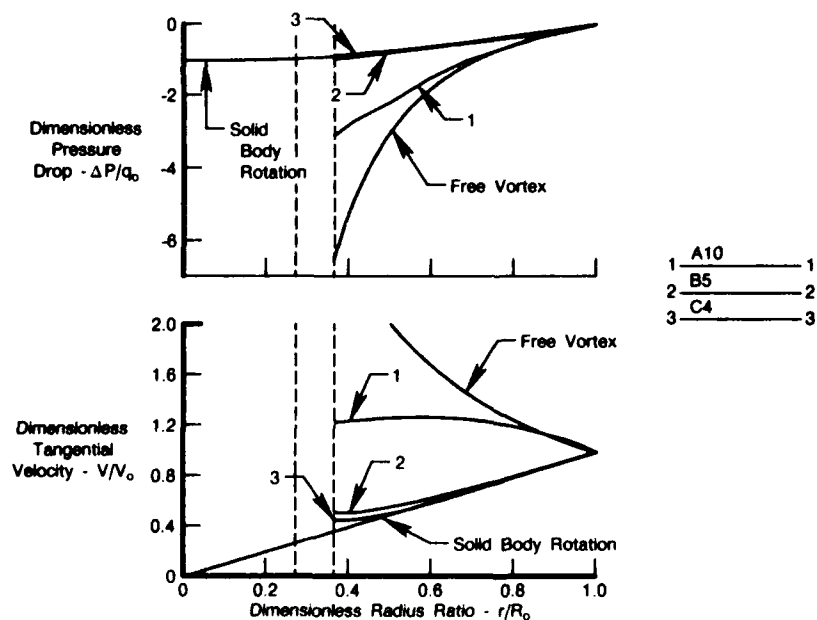
FDA 334598

Figure 52. — Effects of Coolant Flowrate on Pressure and Tangential Velocity Distributions in Bleed Cavity for Coolant Injection Location B



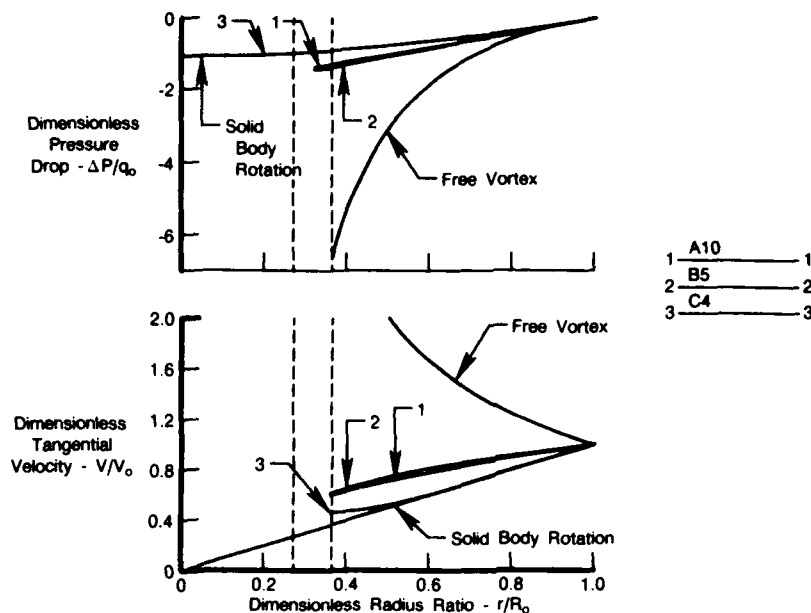
FDA 334599

Figure 53. — Pressure and Tangential Velocity Distributions in Selected Cavities of Compressor Drum With Baseline Flow Conditions and Coolant Injection Location C, Test Point C4



FDA 334600

Figure 54. — Comparison of Pressure and Tangential Velocity Distributions in Compressor Cavity 2 for Baseline Flow Condition and Three Coolant Injection Locations



FDA 334601

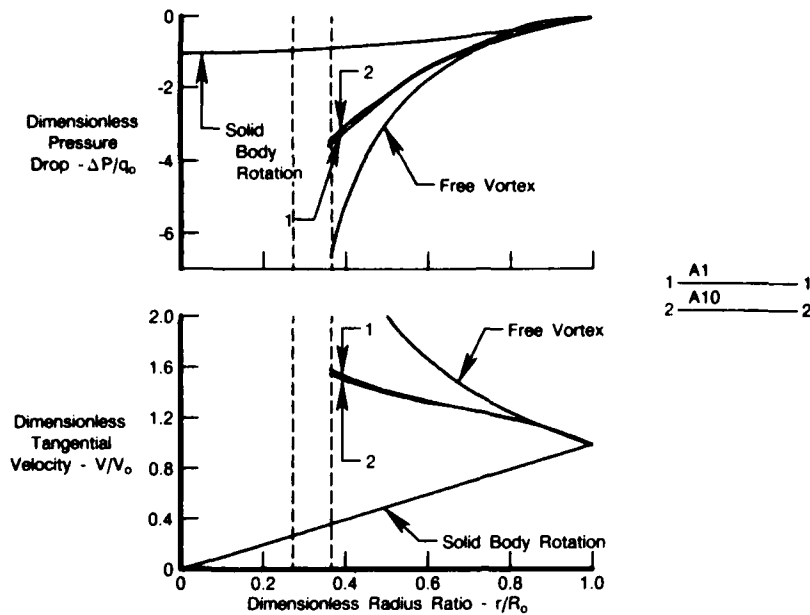
Figure 55. — Comparison of Pressure and Tangential Velocity Distributions in Compressor Cavity A for Baseline Flow Condition and Three Coolant Injection Locations

### 3. ANALYSIS OF THE FLOW IN THE BLEED CAVITY

#### a. Parametric Results

The bleed cavity dimensionless pressure drop and tangential velocity profiles obtained for bleed Configuration A, at two tangential Reynolds numbers are shown in Figure 56. The flow conditions for the data shown were chosen to produce a value of the dimensionless flow parameter,  $\eta_c$ , of  $\eta_c = 0.04$  (baseline condition). The results shown in Figure 56 indicate that the scaling parameter  $\eta_c$  correlates the bleed cavity aerodynamic characteristics with flow conditions. As a result of plots similar to Figure 56, it was found that  $\eta_c$  was able to correlate the pressure drop and the velocity ratios in the non-bleed cavities as well and to do so for all bleed configurations investigated. The conclusion from this finding was that  $\eta_c$  is the appropriate scaling parameter to be used to correlate the compressor drum aerodynamic characteristics.

A cavity-by-cavity comparison of the compressor drum aerodynamic characteristics obtained in this investigation for bleed configurations A, B, and C at two radial locations is shown in Table 7. Here, the cavity core rotation factors obtained for each bleed configuration are presented as a function of the dimensionless flow parameter (scaling parameter)  $\eta_c$ . The data shown were obtained at the dimensionless radius ratios of  $r/R_o = 0.36$  (bore radius) and  $r/R_o = 0.68$ . The core rotation factor ( $k$ ) is defined as the tangential velocity of the fluid at radius  $r$  divided by the local wheel speed  $r\Omega$ . The core rotation factor is a measure of the swirl level of the fluid in the cavity.



FDA 334602

Figure 56. — Comparison of Pressure and Tangential Velocity Distributions in Compressor Cavity 2 for Baseline Secondary Flow Parameter and Two Tangential Reynolds Numbers

There are a number of observations which can be made from Table 7. First, the cavity swirl levels for bleed configuration A are generally greater in all cavities at a given flowrate than those produced by bleed configurations B and C. Note that for the A bleed configuration, the swirl is greatest in the bleed cavity and that the swirl level decreases in the cavities upstream and downstream of the bleed cavity. The decay of the cavity swirl levels appears to be slightly greater for the upstream cavities than for the downstream cavities. This apparently larger decay of angular momentum in the upstream cavities is probably due to the fact that the flow toward the dead end of the drum must be returned along the compressor drum shaft toward the exit end of the drum.

The results shown in Table 7 for the B bleed configuration indicate that the swirl level is greatest in bleed cavity A and that the core rotation factors in the downstream cavities progressively decrease toward a value of 1.0. A core rotation factor of 1.0 indicates a solid body rotation type behavior. Note that the results in Cavity A for the B bleed configuration are approximately the same as the results obtained in Cavity A for the A bleed configuration at the same flowrate.

Finally, the results shown in Table 7 for the C bleed configuration indicate that the core rotation factor for all of the flowrates investigated is approximately 1.0 in all cavities. Increasing the flowrate for this type of bleed design does not increase the swirl velocities in the drum.

TABLE 7.  
COMPARISON OF CORE ROTATION FACTORS, K, FOR SELECTED SECONDARY  
FLOW PARAMETERS AND THREE COOLANT INJECTION LOCATIONS

Flow Condition		Cavity				
$Re_i/Re_0.8$	Test	A	1	2	3	4
<i>Core Rotation Factor at <math>r/R_o = 0.36</math></i>						
0.018	A5	1.2	1.5	2.3	1.7	—
	B6	1.5	1.3	1.3	0.9	0.9
	C5	1.1	1.0	1.1	1.0	1.2
0.032	A4	1.6	2.0	3.4	2.3	1.9
	B5	1.6	1.5	1.4	1.3	1.3
	C4	1.2	1.1	1.2	1.1	1.0
0.068	A6	2.2	2.9	5.0	3.0	2.8
	B7	2.5	1.9	1.5	1.0	—
	C6	1.3	1.3	1.3	1.2	1.1
<i>Core Rotation Factor at <math>r/R_o = 0.68</math></i>						
0.018	A5	1.0	1.0	1.6	1.1	1.0
	B6	1.1	1.0	0.9	1.0	1.0
	C5	1.0	1.0	1.0	1.0	1.0
0.032	A4	1.2	1.1	1.9	1.1	1.1
	B5	1.2	1.1	1.0	1.0	1.0
	C4	1.0	1.0	1.0	1.0	1.0
0.068	A6	1.3	1.4	2.1	1.3	1.3
	B7	1.0	1.2	1.2	1.2	1.1
	C6	1.0	1.0	1.0	1.0	1.0

3921C

#### b. Analytical Formulation

An analysis is available at UTRC which can be used to predict the disk cavity aerodynamic characteristics of the bleed cavity of a midstage bled compressor drum system. Since compressor drums operate at Reynolds numbers of  $10^6$  to  $10^7$ , the flow in the bleed cavity is highly turbulent (Reference 2). Therefore, the model used in the analysis is necessarily constrained to a turbulent transport model of the flow.

Although the flow in the bleed cavity is rather complex, previous investigations (References 14 and 15) have shown that the flow can be divided into two principal regions: (1) a core flow with low radial velocities and tangential velocities which are primarily functions of the radius, and (2) a turbulent boundary layer flow along the disk walls which can have radial velocities which can be on the same order of magnitude as the tangential velocities. These two regions can be highly interactive with flow into and out of the boundary layer depending upon the angular momentum and radial pressure balances in these two regions. The analytical formulation developed couples the flow in the core region with the disk boundary layer flows. The analysis combines a momentum integral analysis for the boundary layer flows, a one-dimensional viscous solution for the core flow, and a turbulent viscosity model.



The analytical formulation is based on the following assumptions: (1) the flow is axisymmetric and time independent, (2) the radial velocities are independent of axial location in the core region, (3) the fluid density can be constant or can vary with the perfect gas law, and (4) the core fluid has a viscosity ( $\bar{\mu}$ ) which is assumed to be constant at all radii.

The core flow tangential momentum equation is:

$$\rho V_r \left( \frac{dV_\theta}{dr} + \frac{V_\theta}{r} \right) = \bar{\mu} \frac{d}{dr} \left[ \frac{1}{r} \frac{d}{dr} (r V_\theta) \right] \quad (10)$$

with solution:

$$V_\theta = C_1 R^{\alpha-1} + C_2 R \quad (11)$$

if a constant radial mass flow is assumed. Here,

$$\alpha = \dot{m}_c / 2\pi S \bar{\mu} \quad (12)$$

where:

$\dot{m}_c$  = core radial flowrate  
 $S$  = distance between the disks  
 $C_1$  and  $C_2$  = constants.

The solution given by Equation 11 can be assumed for small radial domains ( $\Delta r$ ) in which the radial mass flow  $\dot{m}_c$  is assumed to be constant. The solution for  $V_\theta$  at the boundary of adjacent domains can be matched to obtain a piece-wise continuous function for  $V_\theta$  over values of the radius from the bore to the rim. This results in a solution for  $C_1$  and  $C_2$  in each radial domain based on the domain inlet  $V_\theta$  and the domain outlet  $V_\theta$ . The error in assuming a constant radial core flow in each domain is small for small radial domains.

The core flow pressure gradient is obtained from the radial momentum equation. Assuming a constant core flowrate for each radial domain, the pressure gradient is given by:

$$dP/dr = \rho V_\theta^2 / r \quad (13)$$

Here, the fluid density can be assumed to be constant or can be assumed to vary with the perfect gas law.

The disk boundary layer tangential and radial momentum equations are given by:

$$\frac{\partial}{\partial r} (r U_r U_\theta) + \frac{\partial}{\partial z} (r U_r U_\theta) = \nu r^2 \frac{\partial^2 U_\theta}{\partial z^2} \quad (14)$$

$$\frac{\partial}{\partial r} (r U_r^2) + \frac{\partial}{\partial z} (r U_r U_z) - U_\theta^2 = - \frac{r}{\rho} \frac{\partial p}{\partial r} + \nu r \frac{\partial^2 U_r}{\partial z^2} \quad (15)$$

Here,  $U$  is the velocity of the fluid in the boundary layer with  $r$ ,  $\theta$ , and  $z$  denoting the radial, tangential, and axial components, respectively.

The integral form of these boundary layer equations are obtained by integrating from the disk wall ( $z = 0$ ) to edge of the boundary layer ( $z = \delta$ ), which gives:

$$\frac{d}{dr} \int_0^\delta (r U_r U_\theta) dz + V_\theta \frac{d}{dr} \int_0^\delta (r U_r) dz = \nu r^2 \frac{dU_\theta}{dz} \Big|_0^\delta \quad (16)$$

$$\frac{d}{dr} \int_0^\delta (r U_r^2) dz + \int_0^\delta (V_\theta^2 - U_\theta^2) dz = v r \frac{dU_r}{dz} \Big|_0^\delta \quad (17)$$

The boundary layer radial and tangential velocity profiles are assumed to be given by:

$$U_r(z/\delta) = \bar{U}_r \left( \frac{56}{13} \right) \left[ \left( \frac{z}{\delta} \right)^{1/7} - \left( \frac{13}{17} \right) \left( \frac{z}{\delta} \right) + \left( \frac{6}{7} \right) \left( \frac{z}{\delta} \right)^2 \right] \quad (18)$$

and

$$U_\theta(z/\delta) = r\omega + (V_\theta - r\omega) (z/\delta)^{1/7} \quad (19)$$

The tangential velocity profile given by Equation 19 is similar to the 1/7th power law turbulent profile used by von Karman (Reference 2). The radial velocity profile given by Equation 18 also has a 1/7th power profile.

In Equation 18 the quantity  $\bar{U}_r$  is the average radial velocity in the boundary layer at radius  $r$ . The boundary layer flow and the core flow can be coupled in each of the radial domains ( $\Delta r$ ) through the continuity equation given by:

$$\dot{m}_c = \dot{M}_t - 2\dot{m}_s \quad (20)$$

Here,  $\dot{M}_t$  is the total flowrate bled into the cavity. A solution is obtained when the mass balance in each radial domain has converged to a prescribed tolerance.

### c. Comparison of Analysis with Experiment

Results predicted from this analysis for the radial pressure drop, tangential velocity, secondary flowrate, and disk boundary layer thickness in the bleed cavity are shown in Figure 57. Results are shown for a number of flowrates. The results are shown in dimensionless form and are plotted versus the dimensionless radius ratio. Note that the predicted pressure drop and tangential velocity profiles for  $0.363 \leq r/R_0 \leq 1.0$  shown in Figure 57 are similar to the experimental results shown in Figure 50 for the A bleed configuration. The predicted pressure drops and velocity ratios for radii less than the disk radii are also presented in Figure 57.

A comparison of results for the dimensionless pressure drop from the disk outer diameter predicted by the analysis and those obtained for the A bleed configuration are shown in Figure 58. The results for the radial pressure drop are presented as a function of the radius ratio for several flowrates and agree favorably with the experimental results. A comparison of the predicted and the measured rim-to-bore pressure drop are presented in Figure 58 as a function of the dimensionless flowrate. The analytical results agree well with the experimental data. The conclusion of the comparison made in Figure 58 is that the aerodynamic characteristics can be accurately predicted for bleed cavities with radial flow inward from the cavity outside diameter.

### d. B Bleed Tangential Velocity Profiles

The tangential velocity profiles for the B bleed configuration shown in Figure 59 indicate that two types of cavity flow behavior near the bore are possible, depending upon the flowrate. Figure 59 indicates a solid-body or linear type velocity profile between the bore and mid-radius for low flowrates and a vortex-type velocity profile between the bore and mid-radius for high flowrates. This phenomenon was investigated further by conducting experiments at many flow conditions. The results are shown in Figure 59. Here, the data is shown using the coordinates  $Re_z$  and  $Re_r$  upon which lines of constant scaling parameter  $\eta_c$  have been superimposed. The results shown in Figure 59 indicate that the tangential velocity profile in the bleed cavity displayed a

vortex-shaped velocity profile near the disk bore for values of  $\eta_c$  greater than  $\eta_c = 0.05$  and a linear-shaped velocity profile for values of  $\eta_c$  less than  $\eta_c = 0.05$ . The conclusion from this analysis of the results is that the shape of the velocity profile near the bore in the bleed cavity is influenced by the coolant flowrate and can be linear or vortex-shaped, depending upon the value of the scaling parameter,  $\eta_c$ .

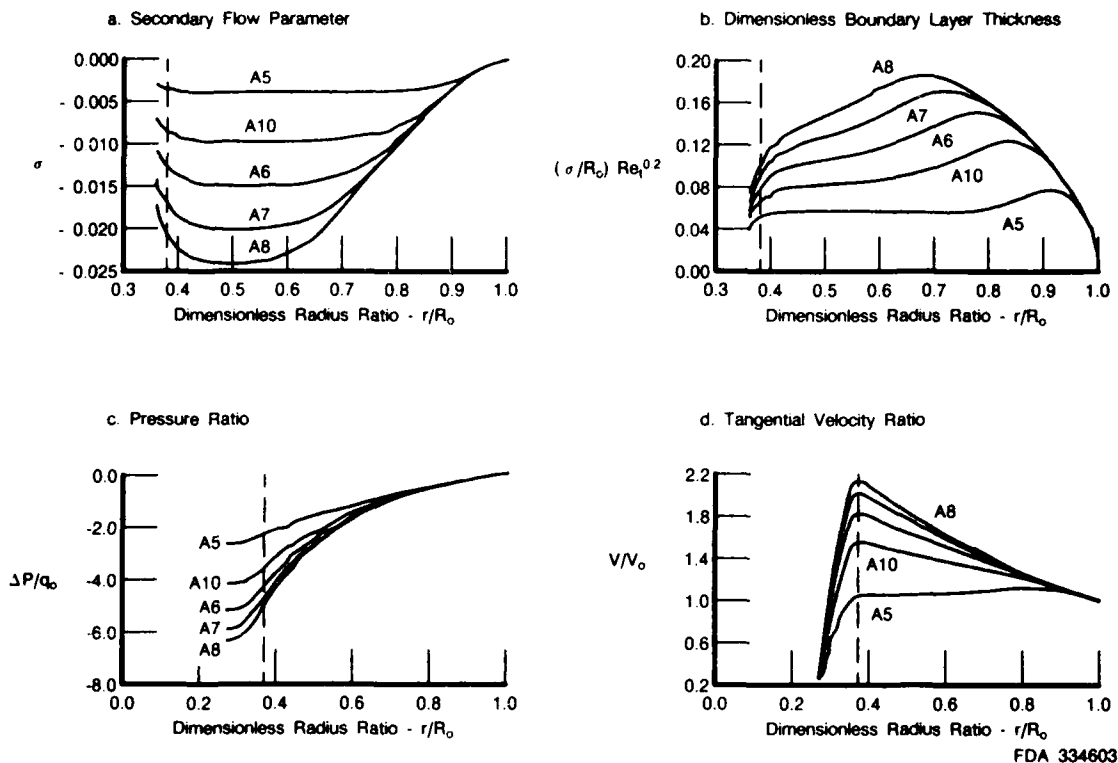


Figure 57. — Prediction of Primary and Secondary Flow Characteristics for Cold Flow Experiments With Injection Location A

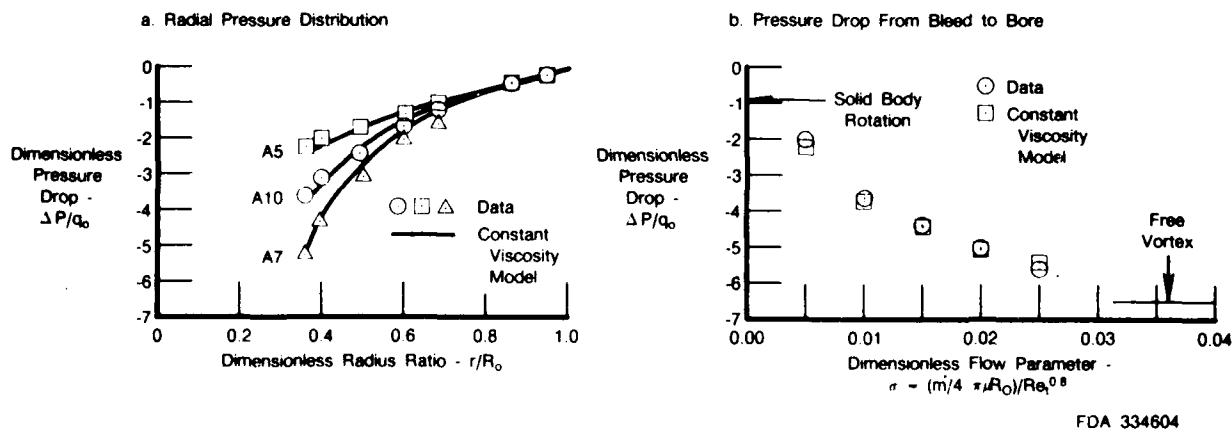


Figure 58. — Comparison of Predicted and Measured Radial Pressure Distributions and Pressure Drop from Bleed to Bore Radii for Cold Flow Compressor Drum Experiments With Coolant Injection Location A

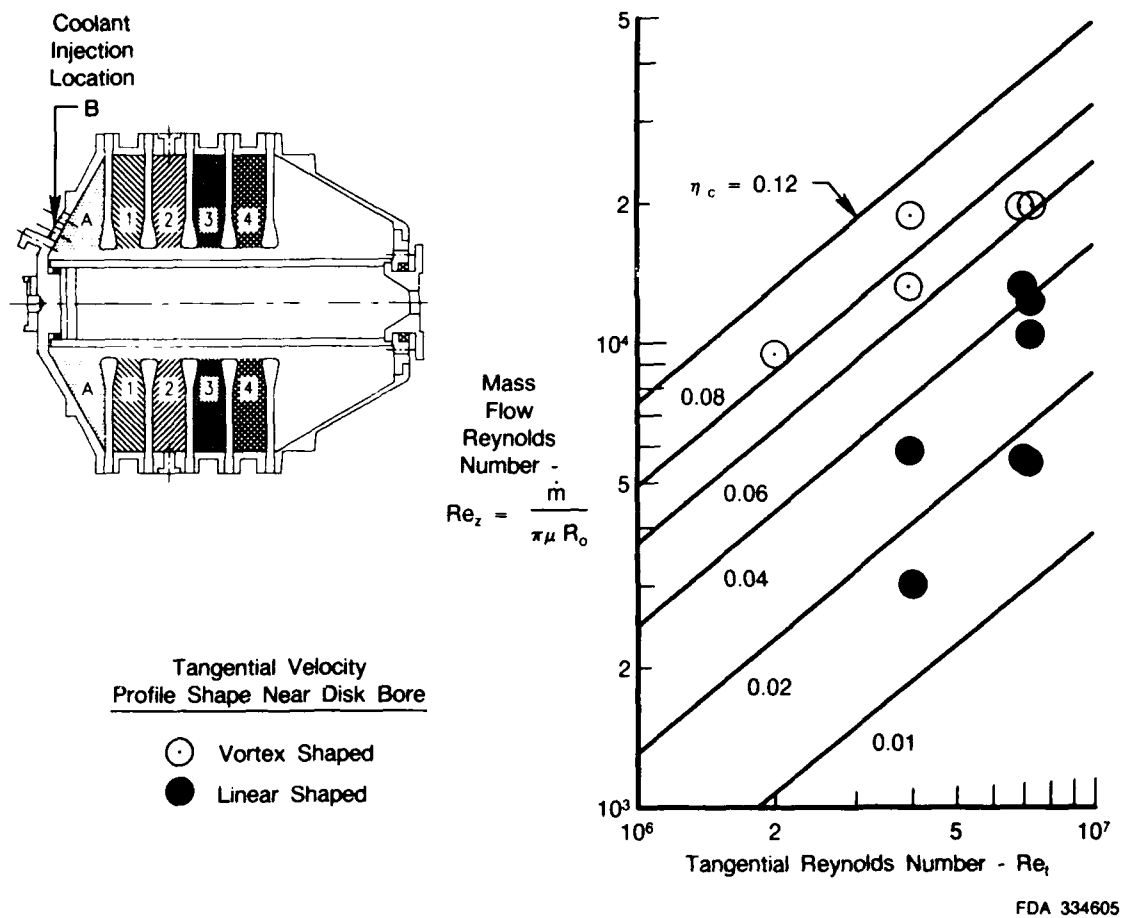


Figure 59. — Effect of Flow Condition on Tangential Velocity Profile Shape Near Disk Bore in Bleed Cavity for Coolant Injection Location B

## SECTION VI

### COMPRESSOR DRUM HEAT TRANSFER EXPERIMENTS

#### 1. INTRODUCTION

##### a. Problem

The coolant bled into the compressor drum is used to control the compressor disk temperatures and to provide cooling air for use in the turbine area. The results of the compressor drum aerodynamic experiments, presented in Section V, have shown that the coolant injection radius and flowrate are the primary parameters which determine the compressor drum flow patterns. Therefore, these parameters are also expected to have a significant effect on the heat transfer mechanisms occurring in the compressor drum. For fan bled compressor drum systems, the angular momentum of the coolant entering the drum is relatively low compared with rim bled systems due to the low injection radius. This results in lower heat-transfer rates and air heat capacity and cavity flows which are primarily buoyancy driven. Therefore, a comprehensive understanding of the heat-transfer characteristics of fan bled compressor drum designs is essential for predicting compressor drum disk thermal response.

##### b. Objective

The objectives of the investigation were to document and correlate compressor drum heat transfer characteristics for both steady-state and transient heating (gas turbine acceleration) and cooling (gas turbine deceleration) cycles for a fan bled compressor drum design system.

##### c. Approach

To achieve these objectives, an experimental investigation was conducted to obtain heat transfer and aerodynamic measurements for a number of compressor drum coolant flowrates and tangential Reynolds numbers. Both transient and steady-state air temperatures, wall temperatures and disk surface heat flux data were obtained as a function of flow conditions in a cavity compressor drum model with a simulated fan bleed injection design. All measurements were obtained at tangential Reynolds numbers typical of current and advanced gas turbine engines. Air was used as the working fluid.

#### 2. DISCUSSION OF EXPERIMENTS AND RESULTS

##### a. Test Apparatus and Procedure

The experiments were conducted using the compressor drum test assembly described in Section II. All data was obtained for bleed configuration B (Figures 10 and 47). The coolant was bled through 8 equally spaced 0.75 in. diameter holes located on the 120 degree conical endwall of the compressor drum assembly at a radius of 6 inches.

To obtain the transient and steady-state heat-transfer data, the model air was diverted through a heat exchanger using high-pressure steam and heated to approximately 240°F. This air was then directed through a static-to-rotating frame air transfer system before entering the model. Due to the large thermal inertia of the massive air transfer system, the temperature of the air entering the model was reduced to approximately 140°F. This resulted in a maximum overall working temperature difference between the hot air and the cold drum of approximately 60 to 70 degrees.

The primary measurements obtained in the investigation were cavity air temperatures, drum surface (metal) temperatures, and drum surface heat flux measurements. All measurements were made in the rotating frame of reference at selected radial and azimuthal locations throughout the test assembly. A total of 43 air thermocouples, 63 wall thermocouples, and 63 heat flux sensors (Figure 13) were used to obtain the data. The transient measurements were obtained by recording the transducer output and sampling time of these instruments in a cyclic fashion during the course of the experiment. The average time between samples obtained from the same instrument was approximately 22 seconds. A total of 43 samples were obtained for each instrument during the run-time of the experiment. The test conditions and pertinent test point identification information for the heat-transfer experiments are presented in Table 8.

TABLE 8.

TEST CONDITIONS AND DIMENSIONLESS PARAMETERS FOR COMPRESSOR  
DRUM HEAT-TRANSFER EXPERIMENTS

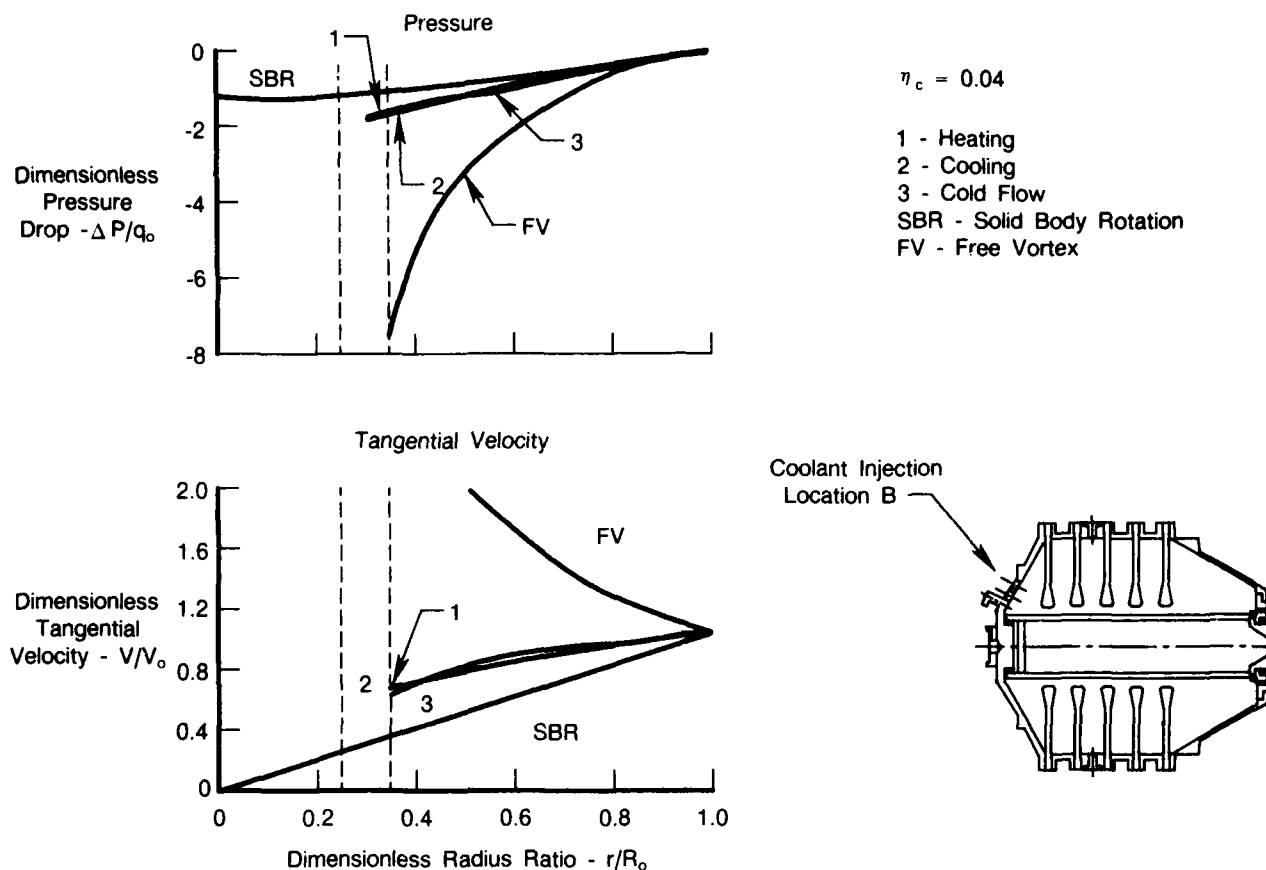
Test	Dimensionless Parameters						Dimensional Parameters								
	$Re_t$ ( $10^{-6}$ )	$Re_z$	$\frac{Re_z}{Re_t^{0.8}}$	$\frac{\Omega_o}{\Omega_i}$	$\frac{T_w - T_c}{T_w}$	$\frac{V_j}{\Omega r_j}$	$\Omega_o$ rpm	$\Omega_i$ rpm	P psia	m lb/sec	$T_w$ °F	$T_c$ °F	$\rho_c$ lb/ft <sup>3</sup>	$V_j$ ft/sec	$\Omega r_j$ ft/sec
B10	5.1	11,690	0.050	1.0	-0.184	0.463	1500	1500	135	0.489	100	203	0.550	36.3	78.5
B11	5.0	10,717	0.047	1.0	-0.193	0.425	1500	1500	134	0.447	94	201	0.547	33.3	78.5
B12	6.9	13,800	0.046	1.0	0.161	0.395	1500	1500	135	0.500	200	94	0.658	31.0	78.5
B13	6.9	12,918	0.047	1.0	0.152	0.404	1500	1500	136	0.509	200	100	0.656	31.7	78.5
B14	5.2	4,898	0.021	1.0	-0.174	0.187	1500	1500	134	0.201	91	187	0.559	14.7	78.5
B15	5.8	5,843	0.020	1.0	0.148	0.167	1500	1500	134	0.211	187	91	0.657	13.1	78.5
B16	4.7	14,720	0.067	1.0	-0.225	0.617	1500	1500	132	0.626	92	216	0.527	48.5	78.5
B17	7.0	20,892	0.070	1.0	0.183	0.595	1500	1500	135	0.755	216	92	0.660	46.7	78.5
B18	2.8	6,311	0.044	1.0	-0.202	0.448	1000	1000	108	0.259	79	188	0.500	23.5	52.4
B19	2.8	6,154	0.043	1.0	-0.175	0.431	1000	1000	107	0.250	84	179	0.452	22.6	52.4
B20	3.7	6,496	0.036	1.0	0.149	0.344	1000	1000	106	0.232	179	84	0.526	18.0	52.4
B21	3.9	7,463	0.040	1.0	0.168	0.382	1000	1000	108	0.265	188	79	0.541	20.0	52.4
B22	3.0	2,848	0.019	1.0	-0.144	0.187	1000	1000	108	0.113	83	161	0.470	9.8	52.4
B23	3.7	3,167	0.018	1.0	0.126	0.169	1000	1000	105	0.113	161	83	0.522	8.8	52.4
B24	2.6	9,911	0.074	1.0	-0.241	0.770	1000	1000	105	0.418	80	210	0.423	40.3	52.4
B25	3.8	12,856	0.071	1.0	0.194	0.685	1000	1000	104	0.457	210	80	0.520	35.9	52.4

Injection Through (8) 0.75 in.-dia holes (0.0245 ft<sup>2</sup>)

3921C

## b. Aerodynamic Results

In addition to heat-transfer measurements, disk cavity pressure data was obtained to determine the effect of heating and cooling on the drum cavity aerodynamic characteristics. The radial pressure drop and tangential velocity profiles obtained for the baseline heating and cooling flow conditions are shown in Figure 60. The baseline flow condition has a coolant flow parameter,  $\eta_c = 0.04$ . The results for the heating and cooling cycles are compared with the results obtained from the compressor drum aerodynamic experiments for the B bleed injection configuration presented in Section V. The results shown in Figure 60 indicate that no measurable changes in the bleed cavity aerodynamic characteristics were observed with heating or cooling, compared with results from the cold flow experiments. The conclusions from this observation are that heating and cooling had no measurable effect on the bleed cavity flow characteristics and that the scaling parameter  $\eta_c$  can be used to describe the flow conditions for the heat-transfer experiments.



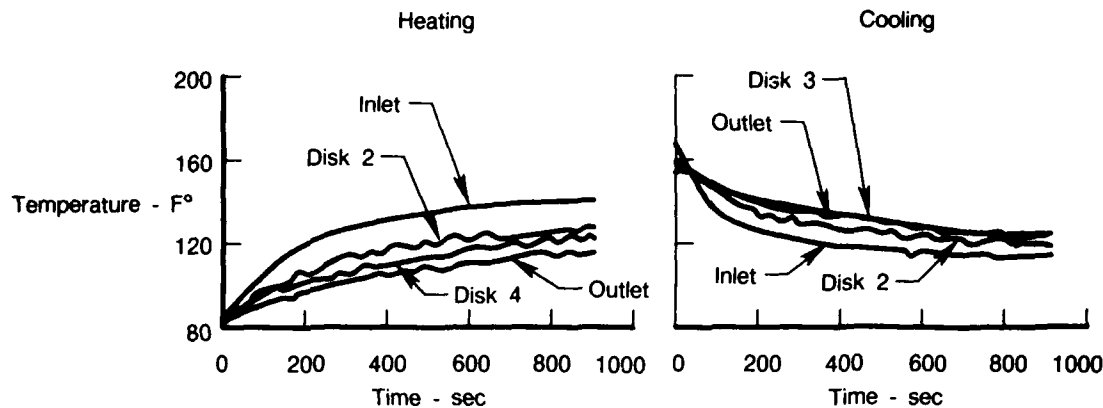
FDA 334606

Figure 60. — Effects of Heating and Cooling on the Bleed Cavity Aerodynamics

### c. Heat-Transfer Results

#### (1) Air Temperatures Along Core

Typical results obtained from the transient heating and cooling experiments for the compressor drum inlet, bore, and outlet air temperature distributions are shown in Figure 61. The drum inlet temperature, bore temperature of disks 2 and 4, and the drum discharge temperature are presented as a function of time from the start of the abrupt temperature change. The results shown in Figure 61 indicate that for the heating, the air temperature continually decreases with increasing distance from the inlet location. The results for the cooling cycle show the opposite; upstream air temperatures are less than the downstream air temperatures at all times.



FDA 334607

Figure 61. — Variation of Air Temperature With Time at Compressor Drum Inlet, Disk 2 Bore, Disk 3 Bore, and Drum Outlet;  $\eta_c = 0.04$ , Coolant Injection Location B

The results shown in Figure 61 also indicate the response times of the test apparatus to the cycles of heating and cooling. The temperature profiles for the heating cycle reach 90 percent of their quasi-steady-state values in approximately 200 to 300 seconds. This is approximately 10 times longer than the thermal response time of a typical gas turbine compressor drum (Reference 16) when accelerated from idle to full power.

## (2) Air Temperatures in Cavity 1

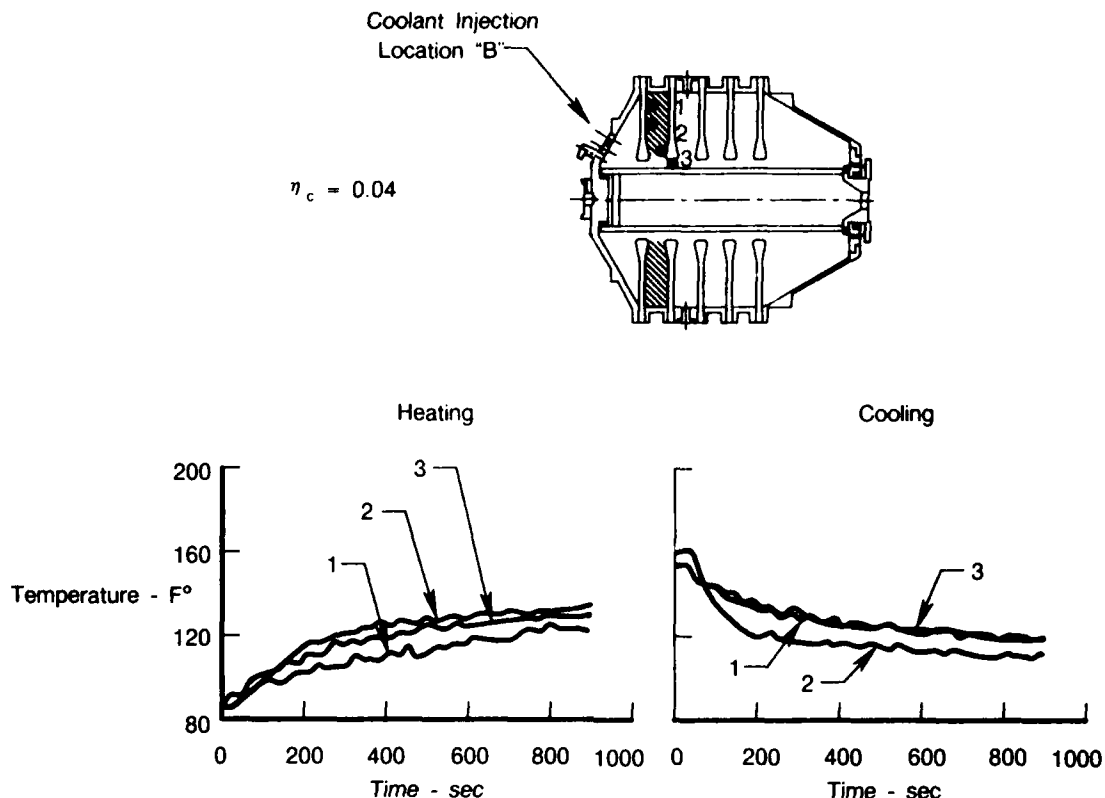
Typical results obtained for the compressor drum disk cavity transient air temperature profiles as a function of time and radial location are shown in Figure 62. The data was obtained for a heating and a cooling cycle. The results shown in Figure 62 were obtained in cavity 1 of the test assembly at the radial locations indicated in the figure insert. The first observation from the results concerns the time history of the mid-cavity air temperature profile and is shown by line 2. The mid-cavity air temperature becomes greater than the air temperature of the cavity disk bore and the cavity outer diameter region after an initial time lapse of approximately 175 seconds. This indicates that a hot-spot has been formed in the center of the cavity. Following the mid-cavity air temperature profile for the cooling cycle, it is observed that after an initial time lapse of approximately 75 seconds, the mid-cavity air temperature becomes less than the air temperature of the cavity disk bore and the cavity outer diameter region. This indicates that on the cooling cycle, a cold-spot has been formed in the center of the cavity. The conclusion from these observations is that the cavity flow field is complex and results in the formation of "thermal pockets" within the cavity that can influence the cavity heat transfer characteristics.

## (3) Wall Temperatures in Cavity 1

Typical results obtained for transient disk surface (metal) temperature profiles as a function of time and radial location are shown in Figure 63. The results shown were obtained in cavity 1 at the radial locations indicated in the model. Observing the mid-cavity disk surface temperature at location 2 for the heating cycle, it appears that the temperature here is well correlated with the results observed for the mid-cavity air temperature profiles shown in Figure 62. Figure 63 indicates that after an initial time lapse, the mid-cavity surface temperature appears to exceed that of locations 1 and 3. The bore surface temperature of disk 1, identified by location 4, appears to be greater than that at locations 1, 2, and 3 at all times. This is probably



due to the fact that the incoming hot air from location B is injected almost directly onto the location 4 wall thermocouple. This can be seen in the insert in Figure 63.



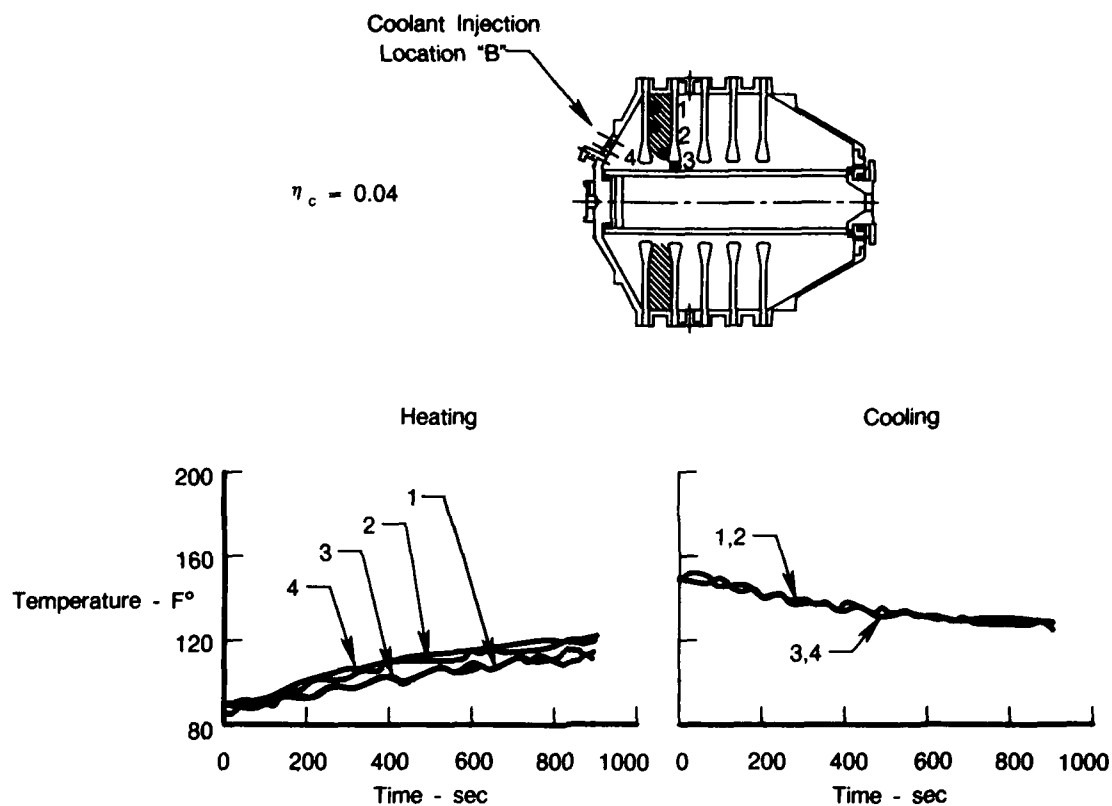
FDA 334808

Figure 62. — Variation of Air Temperature With Time at Three Radial Locations in Cavity 1

The principal observation that can be made from Figure 63 concerns the surface temperature profiles obtained for the cooling cycle. The results shown for cavity radial locations 1 and 3 indicate that the disk surface temperature decay as a function of time at these locations is identical. The surface temperature profiles obtained at locations 2 and 4 were found to be identical with those shown for locations 1 and 3. The result of this observation is that the heat transfer mechanisms for heating are significantly different than those for cooling.

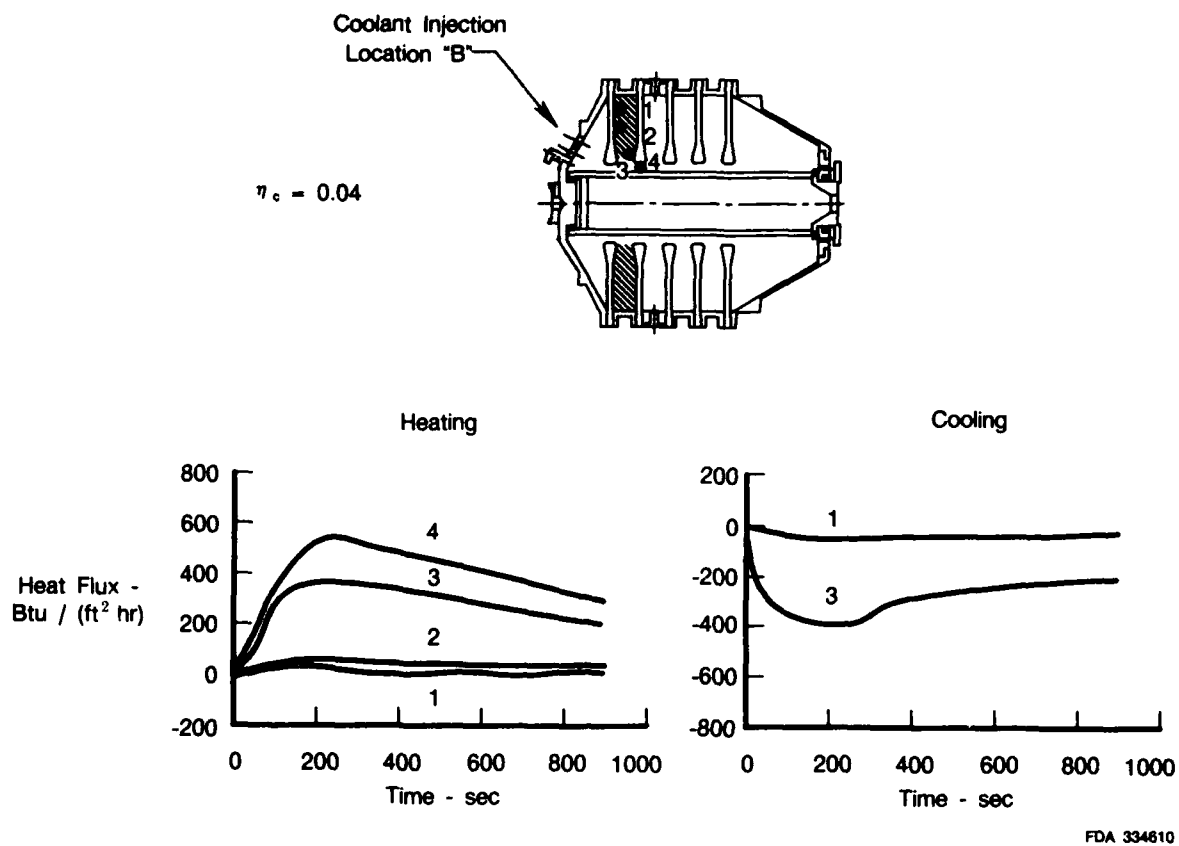
#### (4) Surface Heat Fluxes in Cavity 1

Typical surface heat flux results for heating and cooling are shown in Figure 64. The results were obtained in cavity 1. The cavity radial locations at which the measurements were obtained are shown in the figure insert. The results shown here indicate that largest heat-transfer rates occur at the cavity bore and that the heat-transfer rates decrease as a function of time and with increasing radius. Note that for both heating and cooling flow conditions, the heat-transfer rates in the outer regions of the cavity are very low. This indicates that most of the disk heat transfer occurs at the bore.



FDA 334609

Figure 63. — Variation of Cavity Wall Temperature With Time at Selected Radial Locations in Cavity 1



FDA 334610

Figure 64. — Variation of Surface Heat Flux With Time at Selected Radial Locations in Cavity 1

### 3. COMPARISON OF RESULTS WITH PREVIOUS CORRELATIONS

There is a lack of information in the open literature for comparison with the results obtained in this investigation. In most cases, the available information was obtained at flow scaling parameters that are not representative of those found in a large scale gas turbine and therefore are not suitable for use as a basis for comparison.

Some compressor drum heat-transfer experiments at engine Reynolds numbers, were conducted at UTRC during the mid-1970s. The model used in these investigations was an eleven-cavity compressor drum model which used Freon 113 as the working fluid and had the coolant injected from the "A" location. From these steady-state heat-transfer experiments, a disk cavity heat transfer correlation for disk cooling was obtained for a rim bleed injection configuration, i.e., "A" location. Heat-transfer results predicted by this correlation are shown in Figure 65 and compared with the results obtained in this investigation for cavity 1 and the "B" coolant injection location.

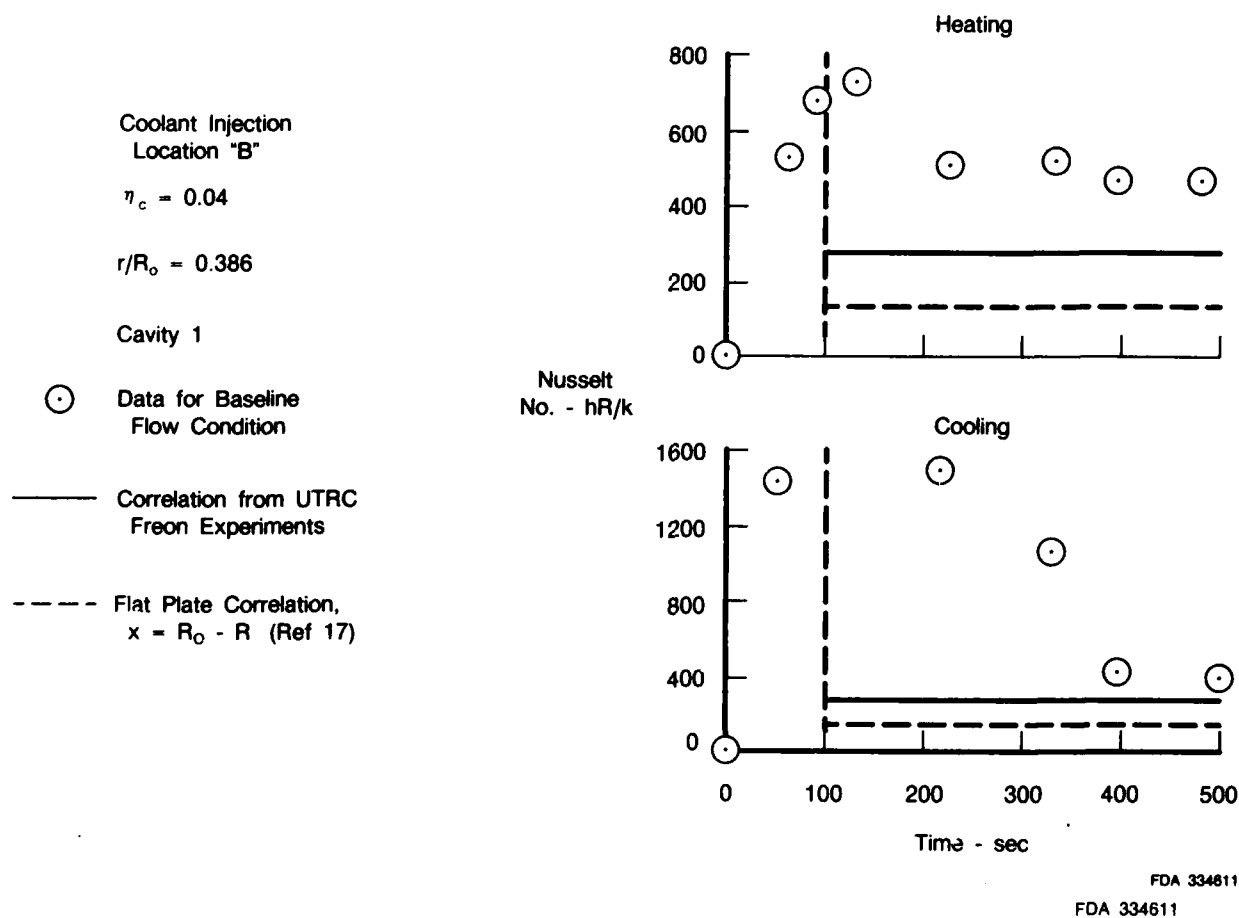


Figure 65. — Comparison of Dimensionless Heat-Transfer Result With Correlations from UTRC Freon Experiments and Flat Plate Theory

Here, the Nusselt number, Nu, is shown versus time. The Nusselt number is defined by

$$\text{Nu} = hr/k \quad (19)$$

where:

$h$  = heat transfer coefficient

$r$  = local radius

$k$  = thermal conductivity of the fluid.

The data shown in Figure 65 was obtained in cavity 1 at the bore of disk 2. In addition to results predicted by the UTRC correlation from the Freon rig experiments, heat-transfer rates predicted from a simple flat plate correlation (Reference 17) are shown for comparison. This correlation is also used for the case of cooling.

The results shown in Figure 65 indicate a relatively large difference between the experimental results and the predicted results during the transient thermal cycles. This indicates that heat transfer rates can be an order of magnitude different during the transient thermal cycle than the value determined by correlations based on steady-state conditions. Note that the results for the cooling transient approaches the UTRC Freon correlation for steady-state cooling as the flow approaches steady-state conditions. Also, the data shown for the heating cycle does not agree well with the UTRC Freon correlation. This is not surprising since the correlation was obtained for cooling and the experimental results presented above have shown that the heat transfer characteristics for heating are quite different from those of cooling.

The most significant observation that can be made from the results shown in Figure 65 concerns the difference in the magnitudes of the heat-transfer rates between the heating and the cooling cycles. Note that the Nusselt numbers for the cooling cycle are approximately twice those of the heating cycle. This may be due to formation of the thermal pockets within the cavity that were shown by the above results. This can produce a potentially unstable flow within the cavity due to density stratifications produced by regions of cold flow over regions of hot flow. This phenomenon should be investigated in greater detail through additional heat-transfer experiments.

## SECTION VII

### CONCLUSIONS

This Disk Pumping Testing Program evaluated secondary flowfields in gas turbine engines to increase the understanding of disk pumping characteristics. The results of turbine disk, turbine rim seal, and compressor drum testing are presented in this section.

#### 1. TURBINE DISK EXPERIMENTS

- The differences in torque coefficients between the flat disks and the smooth turbine disks were attributed to differences in the friction and not to changes in the aerodynamics in the disk cavity.
- The torque coefficients for the counter-rotating disks were insensitive to radial flow direction (inward or outward), whereas the torque coefficients for the co-rotating disks and the one static disk flow conditions increased with increasing flow outward and decreased with increasing flow inward injected with swirl.
- The wall friction on the shroud wall and accompanying torque requirements for typically spaced turbine disks with one disk rotating and one disk static is greater than the torque on the static disk.
- The torque coefficients for counter-rotating disks with a diaphragm installed between disks is approximately the same as for the one static disk condition. The torque coefficients for the counter-rotating smooth turbine disk with no bleed flow and a diaphragm are approximately half those obtained without a diaphragm.
- The torque coefficients for a turbine disk with a typical bolt pattern are approximately twice those for a smooth turbine disk configuration.
- The partial bolt covers evaluated were ineffective in reducing torque coefficients.

#### 2. TURBINE RIM SEAL INGESTION EXPERIMENTS

- The rim seal purge flow required to completely prevent ingestion are compatible with those obtained previously. A trace gas method was employed in this report whereas pressure relationships and flow visualization techniques were used in previous studies.
- A "Turbulent Diffusion Model" for turbine rim cavity seals predicted the shape of the cooling effectiveness versus purge flowrate relationship for the rim seals.
- A decrease in the radial gap between rotating and static seals produced the largest improvement in cooling effectiveness for a given purge flowrate.
- Increasing the axial overlap of a seal improved the cooling performance a modest amount.

### 3. COMPRESSOR DRUM AERODYNAMIC EXPERIMENTS

- The radial pressure distribution in the bleed cavity was strongly dependent on the coolant flowrate and the bleed location. The highest pressure drops were obtained for the bleed location with the largest injection radius and the largest coolant flowrate.
- The dimensionless secondary flow parameter,  $\eta_c = \dot{m} / (\pi \mu R_o) / (\rho V_\theta R_o / \mu)^{0.8}$  was effective in correlating the aerodynamic characteristics of the flow in the compressor cavities.
- The pressure drop distributions in the bleed cavity were well predicted with a momentum integral analysis of the core and boundary layer flows in the cavity.

### 4. COMPRESSOR DRUM HEAT TRANSFER EXPERIMENTS

- Heating and cooling the compressor drum cavity did not noticeably affect the pressure distribution or the tangential velocity distributions in the cavities.
- The maximum dimensionless heat-transfer rates obtained during the transient cooling cycle were approximately twice as great as those for the heating cycle.
- The differences between the dimensionless heat-transfer rates obtained in the heating and cooling cycles were attributed to stabilization of the flow during heating and destabilization of the flow during the cooling transient.
- The dimensionless heat-transfer rates obtained during both the heating and cooling transient cycles were greater than predicted from flat plate free convection correlations or from correlations obtained from previous steady-state, rotating-heat-transfer experiments.

## APPENDIX

### A TURBULENT DIFFUSION MODEL FOR TURBINE RIM CAVITY SEALS BY B.V. JOHNSON (SELECTED PORTIONS OF REFERENCE 10)

#### 1. INTRODUCTION

The perennial goal of the gas turbine designer to obtain increased performance by increasing the turbine inlet temperature is partially thwarted by the need to cool portions of the turbine in order to maintain the structural integrity of the turbine. The turbine rim cavity is one portion required to be cooled as heat from the mainstream is ingested into the rim cavity by conduction or convection. Cooling air is generally supplied to the cavity to maintain acceptable temperatures within the cavity. However, the diversion of compressor air to the cavity and its subsequent injection into the mainstream cause thermodynamic and aerodynamic penalties.

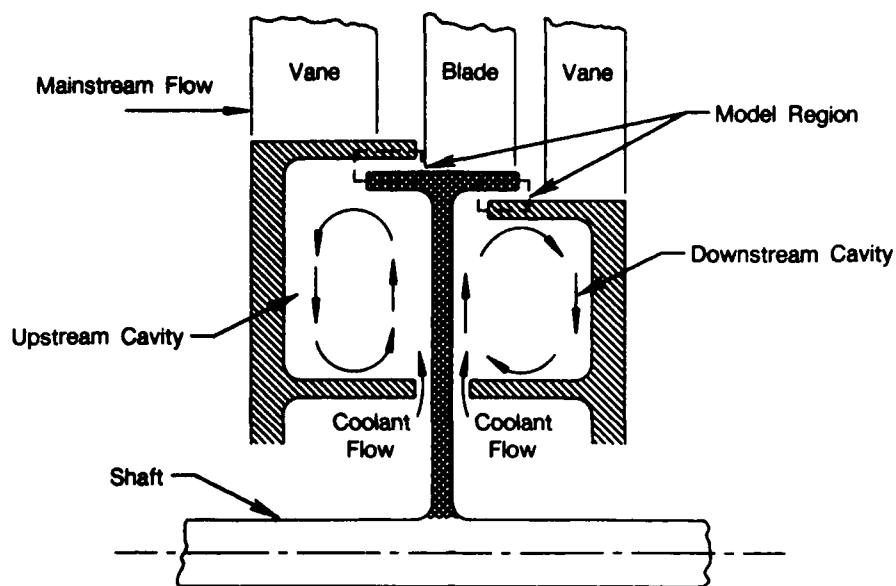
At present, the fluid mechanics of ingestion from the mainstream into the rim cavity are not completely understood for all rim seal configurations. For some configurations (i.e., wide clearances between the rotor and the upstream shroud) a boundary layer model has been formulated and is probably appropriate. However, as the radial clearances are reduced and the rotor rim and the vane shrouds are overlapped, the heat ingestion characteristics are expected to be more influenced by the rim cavity configuration than by the rotor boundary layer flow characteristics. In the present report, a one-dimensional turbulent diffusion model for the latter flow condition is formulated, a solution obtained, and the analytical results compared with experimental results.

#### 2. HEAT INGESTION MODEL

A sketch of the turbine rim seal components are shown in Figure A-1. As shown, the model is developed for a relatively large overlap of the vane and blades. This model allows the heat transport problem to be formulated with a one-dimensional coordinate system, although, as discussed later, the model can be applied to more complicated geometries. It should be noted that the fluid mechanics of flows between stationary and rotating cylinders have been studied by Taylor (Reference 18) and Cole (Reference 19). For some of these flows between rotating cylinders, well-defined cells were formulated. For this model, the turbulent transport of heat is attributed to the turbulent mixing between these cells or by other shear induced turbulent structure.

The details required for the turbulent conduction model are shown in Figure A-2. The flow within the cavity is assumed to be at uniform temperature from the fluid circulation caused by the boundary layer pumping. The heat and flow are assumed to be transported uniformly through an annular passage of length ( $l$ ), average radius ( $R$ ), and height ( $\Delta R$ ). The average mass flux in this annular passage ( $\rho U$ ) is equal to  $W_c/2\pi R\Delta R$  where  $W_c$  is the coolant flowrate. The temperature at the cavity and free stream side of the annular slot are assumed to be maintained at the average cavity temperature ( $\bar{T}$ ) and the free stream temperatures ( $T_e$ ), respectively, by a strong cross stream flow at those axial locations.

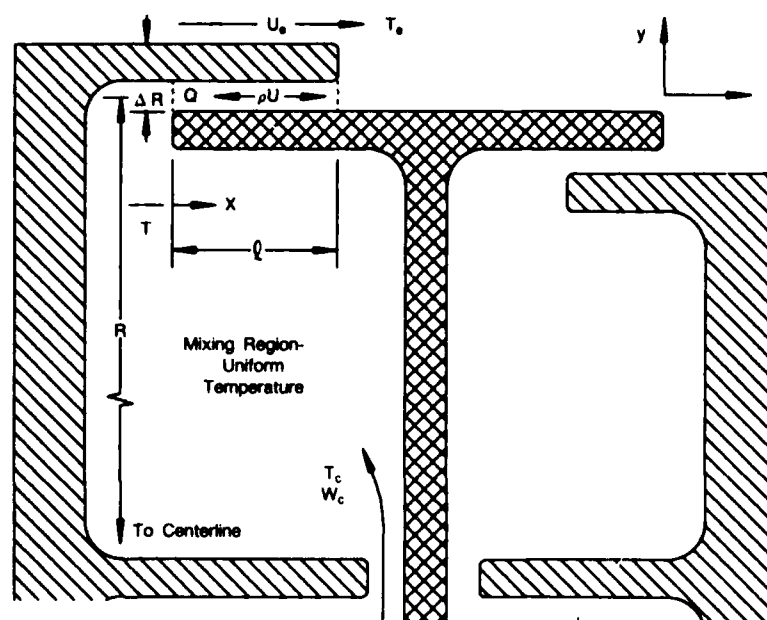




FDA 334508

Figure A-1. — Turbine Rim Seal Components

Heat Flux:  $-Q = -AK \frac{dT}{dX} + \rho U A C_p T$   
 Cross Section Area:  $A = 2 \pi R \Delta R$   
 Mass Flux from Cavity:  $W_c = \rho U A$



FDA 334509

Figure A-2. — Details of Turbulent Diffusion Model for Turbine Rim Cavity Seals

The heat flux at any axial location along the annulus is:

$$-Q = -KA \frac{dT}{dx} + \rho U A C_p T \quad (A-1)$$

where  $Q$  is the positive value of heat being transported into the cavity,  $K$  is a turbulent conductivity coefficient which is assumed to be constant and independent of coolant flowrate ( $W_c = \rho UA$ ) for this model. A heat balance on a control volume of cross section  $A$  and length of  $dx$  with constant fluid properties yields:

$$\frac{d^2T}{dx^2} - \frac{W_c C_p}{KA} \frac{dT}{dx} = 0 \quad (A-2)$$

The general solution to equation A-2 with a positive value of  $W_c C_p / (KA)$  is (Reference 20):

$$T = C_1 e^{W_c C_p x / (KA)} + C_2 \quad (A-3)$$

Applying the boundary conditions of  $T = \bar{T}$  at  $x = 0$  and  $T = T_e$  at  $x = \ell$  yields:

$$T = \bar{T} + (T_e - \bar{T}) \frac{e^{W_c C_p x / (KA)} - 1}{e^{W_c C_p \ell / (KA)} - 1} \quad (A-4)$$

### 3. ANALYTICAL RESULTS

The first result obtainable from the general solution of the temperature distribution (equation A-6) is the, as yet undetermined, heat flux  $Q$ . This is obtained by evaluating Equation A-1 at  $x = 0$ :

$$Q = \frac{(T_e - \bar{T}) W_c C_p}{e^{W_c C_p \ell / (KA)} - 1} - W_c C_p \bar{T} \quad (A-5)$$

It is convenient to reference the local, coolant, and free stream temperatures to the cavity temperature (i.e., let  $\bar{T} = 0$ ). Equations A-4 and A-5 are then rewritten:

$$T = T_e \frac{e^{W_c C_p x / (KA)} - 1}{e^{W_c C_p \ell / (KA)} - 1} \quad (A-6)$$

and

$$Q = \frac{T_e W_c C_p}{e^{W_c C_p \ell / (KA)} - 1} \quad (A-7)$$

The limiting heat flux as  $W_c$  approaches zero is:

$$Q_0 = \frac{T_e W_c C_p}{(1 + \frac{W_c C_p \ell}{KA} + \dots - 1)} = \frac{T_e KA}{\ell} \quad (A-8)$$

the conduction heat transfer through the annulus. It is convenient to calculate an equivalent flowrate ( $W_0$ ) which would be required to convect the same amount of heat into the cavity as is conducted for the zero coolant flowrate:

$$W_0 = Q_0 / C_p T_e = (KA) / (C_p \ell) \quad (A-9)$$

In subsequent discussion,  $W_0$  will be used in place of the quantity  $((KA) / (C_p \ell))$ . Evaluation of  $W_0$  requires experimental data, primarily because of turbulent thermal conductivity is unknown.

AD-A187 199

DISK PUMPING TEST(U) PRATT AND WHITNEY WEST PALM BEACH  
FL GOVERNMENT PRODUCTS DIV D J GRABER ET AL SEP 87  
PW/GPD-FR-19184 AFMAL-TR-87-2050 F33615-83-C-2331

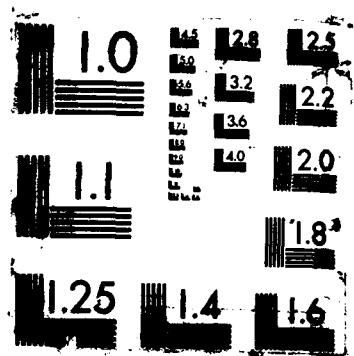
2/2

UNCLASSIFIED

F/G 21/5

NL



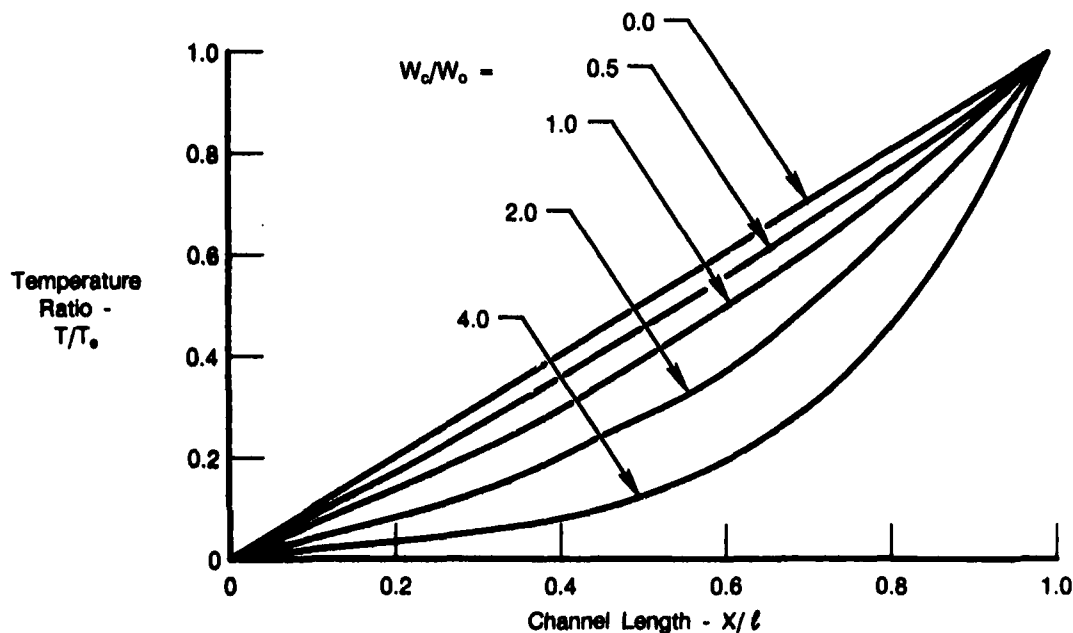


A flowrate convecting an amount of heat equivalent to that conducted through the annulus can be experimentally determined for each test point from the coolant flowrate and the cavity cooling effectiveness data. One method for determining  $W_o$  would be to extrapolate the values of equivalent ingested flowrate  $W_i$  for a coolant flowrate equal to zero. A second method would be to make use of the analytical results from the variation of  $\eta$  with  $W_c/W_o$  (developed in the subsequent paragraph) and determine  $W_o$  from test points where the results are more accurate than those obtainable for the flowrate condition.

The nondimensional temperature distribution along the annular duct can also be obtained from the second boundary condition,  $T = T_o$  at  $x = \ell$ :

$$\frac{T}{T_o} = \frac{e^{W_c x / (W_o \ell)} - 1}{e^{W_c / W_o} - 1} \quad (A-10)$$

The results from this equation are presented graphically in Figure A-3. The principal features are a linear temperature profile for zero coolant flowrate (see equation A-8) and increasing temperature gradients as  $x/\ell$  approaching 1.0 with increasing flow ratio.



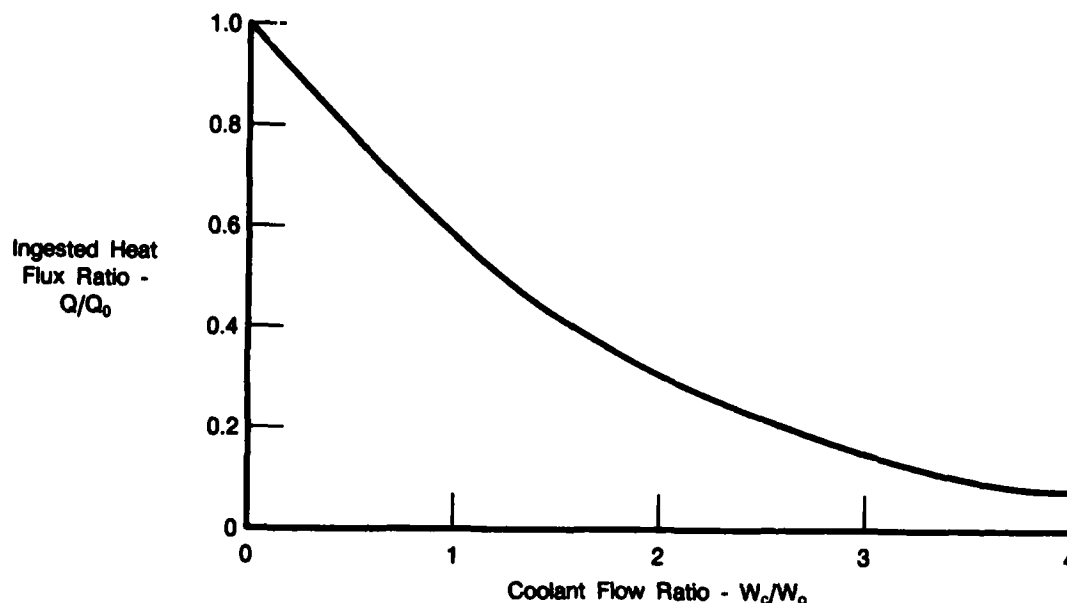
FDA 334510

Figure A-3. — Axial Variation of Temperature in Annular Channel

The ratio of the ingested heat flux with coolant to that conducted when no coolant is flowing, for the same temperature difference across the seal, can be obtained from equations A-7, A-8, and A-9:

$$\frac{Q}{Q_o} = \frac{W_c / W_o}{e^{W_c / W_o} - 1} \quad (A-11)$$

This result is presented graphically in Figure A-4. The principal feature of this solution is the significant decrease in ingested heat flux with increasing flow ratio,  $W_c/W_o$ .



FDA 334511

Figure A-4. — Variation of Ingested Heat Flux Ratio With Coolant Flow Ratio

The cooling effectiveness is defined:

$$\Phi = \frac{T_s - \bar{T}}{T_s - T_c} = \frac{T_s}{T_s - T_c} \quad (\text{A-12})$$

as  $\bar{T}$  is referenced to zero for this analysis. As previously mentioned, heat is being conducted into the cavity through the rim seal and coolant is being added to the cavity at a second location. A heat balance with these quantities yields the steady-state result:

$$Q + W_c C_p T_c = 0 \quad (\text{A-13a})$$

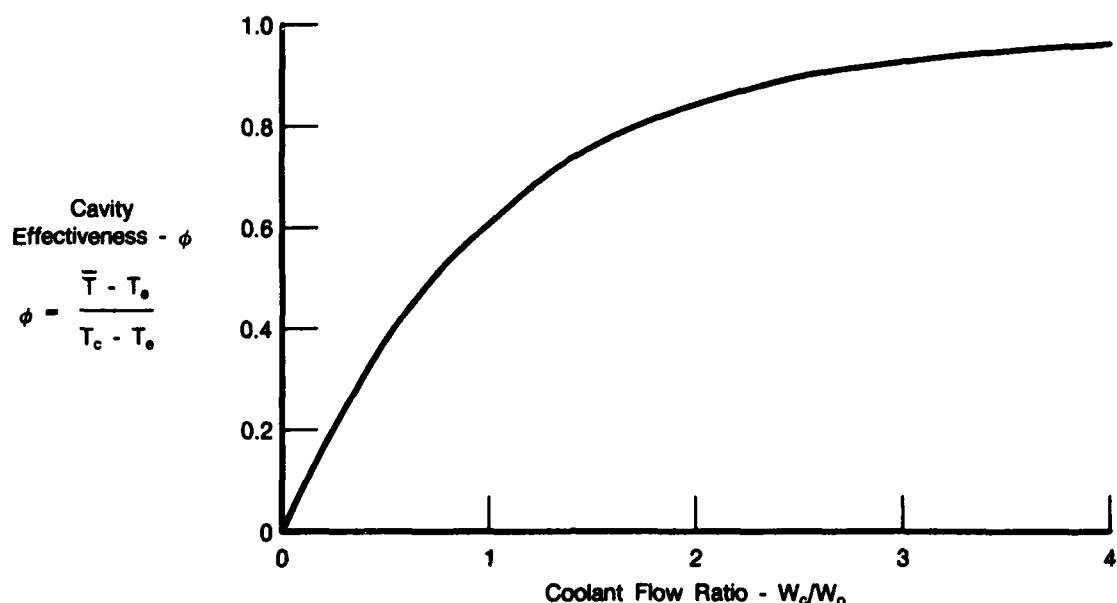
Combining Equation A-13a and the expression for  $Q$  (equation A-7), the following is obtained:

$$\frac{T_s W_c C_p}{e^{W_c/W_0} - 1} + W_c C_p T_c = 0 \quad (\text{A-13b})$$

Equations A-12 and A-13b are combined to obtain the following expression for effectiveness:

$$\Phi = \frac{e^{W_c/W_0} - 1}{e^{W_c/W_0}} \quad (\text{A-14})$$

This result is graphically presented in Figure A-5. The significant increase in effectiveness with coolant flow ratio ( $W_c/W_0$ ) is due to both the decrease in heat flux into the cavity and the increased coolant flow into the cavity.



FDA 334512

Figure A-5. — Variation of Cavity Effectiveness With Coolant Flow Ratio

The flow model presented has been used to obtain the parameters important to the thermal protection of the rim regions. The solution was obtained for constant coefficients ( $\alpha$  and  $\beta$ ) in the transport region. However, a solution which will most likely have the same characteristics can also be obtained (equation A-3) when the conductivity and the gap width are one-dimensional functions of  $x$ . Consequently, the form of the effectiveness solutions is expected to be applicable when the geometries are more complex.

#### 4. TURBULENT TRANSPORT CHARACTERISTICS

At present, the turbulent characteristics of the flow in the vicinity of turbine rim seals is unknown. It is the purpose of this subsection to examine several modes of turbulence generation which could produce the eddy thermal conductivities required to be compatible with the present model and the previous UTRC experiments.

In convection turbulent transport problems convection generally dominates the heat flux in the direction of the mean flow. In the turbine rim region, the mean flow direction is primarily tangential with an axial cross flow convecting fluid from the cavity to the mainstream. When the axial cross flow velocity is much less than the turbulent velocities which create an eddy thermal conductivity within the rim seal region, the axial heat flux can be expected to be dominated by turbulent conductivity. When the cross flow velocity is much greater than the turbulent velocities, the axial heat flux will be primarily convective. The region of interest for the turbine rim seal is apparently between these two limiting conditions and, hence, the heat transfer is a combination of turbulent conduction and convection.

There are several flow models which could provide turbulence generation in the turbine rim seal region. These include (1) turbulent shear between concentric rotating cylinders, (2) large-scale instabilities which occur because of the tangential velocity distribution, (3) turbulence

convected from the disk boundary layer, and (4) turbulence generated by the free shear layer at the disk outer diameter.

**(a) Turbulent Shear Between Concentric Rotating Cylinders**

A turbulent viscosity mixing length model is presented in Reference 4 with  $\epsilon = U \cdot K(r_2 - r_1) / (r_2 - r_1)$  where  $U$  is the shear velocity,  $U_* = \sqrt{\tau / \rho}$ ,  $r_1$  and  $r_2$  are the inner and outer radii of the annulus and  $K$  is a constant. This model has successfully been used to predict the velocity distribution between a long rotating inner cylinder and a stationary outer cylinder with  $K = 0.4$  and  $U_*$  determined from torque measurements. Using torque data for long concentric cylinders, the characteristic turbulent velocity and the maximum eddy viscosity could be expected to be  $U_* = 0.03 V_o$  and  $\epsilon = 0.003 V_o \Delta R$ . Using torque data for a free cylinder increases the shear turbulent velocity to  $0.06 V_o$ .

**(b) Transport Due to Large-Scale Cells**

Taylor and Coles (References 18 and 19) have extensively studied the cell structure formed between concentric rotating cylinders. The turbulent interaction of this large cell structure is a potential cause of large axial heat conductivities. These large cells are expected where the inner cylinder rotates and the outer cylinder is stationary as the case for the upstream turbine rim seal with large overlaps. Limited data, available for heat transfer between an outer stationary cylinder and an inner rotating or stationary cylinder (Reference 21), shows that the heat transfer coefficients vary by factors of 5 at the same Reynolds number, depending on rotating and axial flow.

**(c) Turbulence Convected From the Disk Boundary Layer**

Most of the flow convected from the rim cavity can be expected to come from the boundary layer region near the rotating disk. From some configurations, the fluid from the disk boundary layer could be expected to flow continuously to the rim seal region and maintain the disk wall boundary layer turbulent characteristics. The eddy viscosities for this flow are expected to be approximately the same as for turbulent shear between concentric rotating cylinders.

**(d) Turbulence Generated by Free Shear Layer at Disk Outer Diameter**

For most rim seal configurations, the flow from the disk is expected to detach and form a free shear layer. The turbulence generated by the free shear layer will have larger scales and greater velocity fluctuations than the flow in the disk boundary layer. Consequently, turbulent transport coefficients greater than for the rotating disk for the concentric cylinder boundary layer generated turbulence can be expected for this configuration.

A thermal conductivity turbulent transport model can be formulated by assuming a turbulent Prandtl number equal to one and using the shear generated eddy viscosities:

$$K = \epsilon_t \rho C_p \quad (A-15)$$

For each of the turbulence generation mechanisms described, the average eddy viscosity in the rim seal region can be expected to be proportional to the rim speed and the clearance between the rim and the shroud and a coefficient which is a weak function of Reynolds number:

$$\epsilon_t = a_1 V_t \Delta R \quad (A-16a)$$



The ratio of eddy viscosity to laminar viscosity is obtained from equation A-16a:

$$\epsilon_t/\nu = a_1 V_t \Delta R/\nu \quad (\text{A-16b})$$

The right-hand side of equation A-16b is recognizable as a Couette flow Reynolds number. Fully-turbulent flow could be expected for Reynolds numbers greater than 3000.

The coefficient  $a_1$  can be evaluated with respect to the turbulent diffusion model for each test geometry and set of flow conditions. Equations A-9, A-15 and A-16a are combined to obtain  $a_1$  as a function of Reynolds number and annular geometry ratios:

$$a_1 = \left( \frac{W_o}{2\pi\mu R} \right) * \left( \frac{\mu}{\rho V_t R} \right) * \left( \frac{l}{\Delta R} \right) * \left( \frac{R}{\Delta R} \right) \quad (\text{A-17a})$$

or

$$a_1 = (R_{w,o}/R_{w,t}) * (l/\Delta R) * (R/\Delta R) \quad (\text{A-17b})$$

## 5. CONCLUDING REMARKS

A turbulent diffusion model was formulated in this report for the convection and eddy conduction of heat through certain turbine rim seal geometries. Results from the model predicted the experimental shape of the variation of cooling effectiveness with coolant flowrate. However, the model requires a turbulent transport coefficient to determine the absolute level of cooling within the rim cavity. Transport coefficients were determined by evaluating the experimental data and found to vary with configuration but be approximately independent of Reynolds number. A present, universal turbulent transport coefficients for the turbulent diffusion model are not available and experiments will be required to determine the nature of the flow in the turbine rim seal region.

## REFERENCES

1. O. L. Anderson, *Theoretical Solutions for the Secondary Flow on the End Wall of a Vortex Tube*, United Aircraft Research Laboratories, Connecticut 06108, R-2494-1, November 1961.
2. H. Schlichting, *Boundary-Layer Theory*, Seventh Edition, McGraw-Hill Book Company, New York, 1979.
3. H. Zimmermann, A. Firsching, G. H. Dibelius, and M. Ziemann, "Friction Losses and Flow Distribution for Rotating Disks with Shielded and Protruding Bolts," *Journal of Engineering for Gas Turbines and Power*, pp 1-6, October 1986.
4. J. M. Owen, *Heat and Mass Transfer in Rotating Machinery*, Hemisphere Publishing Corporation, New York, 1984.
5. A. Z. Szeri, S. J. Schneider, F. Labbe, and H. N. Kaufman, "Flow Between Rotating Disks. Part 1. Basic Flow," *Journal of Fluid Mechanics*, Vol. 134, pp 103-131, 1983.
6. D. Dijkstra and G. J. F. van Heijst, "The Flow Between Two Finite Rotating Disks Enclosed by a Cylinder," *Journal of Fluid Mechanics*, Vol. 128, pp 123-154.
7. F. J. Bayley and J. M. Owen, "The Fluid Dynamics of a Shrouded Disk System with a Radial Outflow of Coolant," *Journal of Engineering for Power*, Vol. 92, pp 335-342, 1970.
8. U. P. Phadke and J. M. Owen, "An Investigation of Ingress for an 'Air-Cooled' Shrouded Rotating Disk System with Radial-Clearance Seals," *Journal of Engineering for Power*, Vol. 105, pp 178-183, 1983.
9. J. C. Bennett, LDV Measurements in a Model Compressor Disk Cavity, *Proceedings of Second International Workshop on Laser Velocimetry*, Purdue University, March 1974.
10. B. V. Johnson, "A Turbulent Diffusion Model for Turbine Rim Seal Cavity Seals," United Technologies Research Center Report UTRC 75-17, February 10, 1976.
11. Eckert, E. R. G. and R. J. Goldstein: *Measurement Methods in Heat Transfer*, 2nd Edition, Hemisphere Publishing Corp., Washington, D.C., 1976.
12. Pederson, D. R., E. R. G. Eckert and R. J. Goldstein: Film Cooling with Large Density Differences Between the Mainstream and the Secondary Fluid Measured by the Heat-Mass Transfer Analogy. *Trans. of the ASME Journal of Heat Transfer*, Vol. 99, November 1977.
13. Denton, J. D. and S. Usui: Use of a Tracer Gas Technique to Study Mixing in a Low Speed Turbine. ASME Paper No. 81-GT-86, March 1981.
14. O. L. Anderson, *Theoretical Effect of Mach Number and Temperature Gradient on Primary and Secondary Flows in a Jet-Driven Vortex*, United Aircraft Research Laboratories, Report for U.S. Air Force Systems Command, Report No. RTD-TDR-63-1098, November 1963.
15. B. V. Johnson, *Analysis of Secondary Flow on a Rotating Disk Adjacent to a Free-Vortex Flow*, United Aircraft Research Laboratories, Connecticut 06108, F212020-1, 1967.

16. D. K. Hennecke, *Heat and Mass Transport in Rotating Machinery*, Hemisphere Publishing Corporation, New York, 1984.
17. E. R. G. Eckert and R. M. Drake, *Heat and Mass Transport*, McGraw-Hill Book Company, New York, 1959.
18. Taylor, G.I.: Stability of a Viscous Liquid Contained Between Two Rotating Cylinders. Phil. Trans. Royal Society A Vol. 223 (1923), pgs. 289-243.
19. Cole, D.: Transition in Circular Couette Flow, *J. Fluid Mechanics*, (1964).
20. Huntington, E.V.: Mathematics section of Mechanical Engineering Handbook edited by L.S. Marks. McGraw Hill, 1951.
21. Dorfman, L.A.: Hydrodynamic Resistance and the Heat Loss of Rotating Solid. Oliver and Boyd, Edinburgh and London, 1963, Chapter 7.

END

DATE

FILMED

FEB.

1988